PHD

Design and Commissioning of an Experimental Rig to Study Buoyancy-Induced Heat Transfer in Axial Compressor Cavities

Luberti, Dario

Award date:
2022

Awarding institution:
University of Bath

Design and Commissioning of an Experimental Rig to Study Buoyancy-Induced Heat Transfer in Axial Compressor Cavities

Dario Luberti

A thesis submitted for the Degree of Doctor of Philosophy

University of Bath

Department of Mechanical Engineering

December 2021

COPYRIGHT

Dario Luberti

……………………………………………

To Livia

Abstract

This thesis describes the design and commissioning of an experimental test rig to characterise and measure buoyancy-induced heat transfer in rotating cavities, simulating an axial compressor in an aero-engine. The purpose of the rig is to provide experimental data to validate computational / theoretical models and thermo-mechanical codes used by engine designers. The work is principally experimental in nature with a strong emphasis on developing appropriate instrumentation for reliable heat transfer measurements performed in a rotating environment at high levels of mechanical stress. Much work is also generated in terms of data analysis, theoretical modelling and finite element analysis.

It is now urgent to reduce harmful emissions at altitude to avoid catastrophic climate change. The next generation of aero-engines (e.g. ultra-high-bypass ratio and geared turbofans) have technology drivers demanding smaller core dimensions; these require shorter compressor blades with increased sensitivity to clearance losses and reliability across a flight cycle. To enable new technologies and architectures, engine designers must predict the temperature and radial growth of compressor disks (to which the blades are attached), which affect the blade tip clearance and compressor stability. These design issues are particularly acute during engine transients.

Efficient operation with reduced fuel consumption is dependent on highly efficient engine components, particularly compressors, leading to the requirement of secondary air systems (SAS) for cooling purposes. Aero-engine compressors typically feature co-rotating disks which form cavities bounded by a shroud, and with an axial through-flow of air. Heat is transferred to the shrouds and disks from the hot, compressed air in the main gas path. If the shroud is hotter than the axial through-flow, buoyancy-induced flow can occur in the open rotating cavities. The radial distribution of temperature and thermal stress in the disks governs the expansion of the rotor and the running clearance between the compressor blades and the outer casing in the mainstream cavity. The issue is also pertinent to industrial gas turbines. Buoyancy-induced flow is a strongly conjugate problem: the temperature distribution on the disks affects the flow in the cavity, and vice-versa.

As a preliminary study, the thesis describes a numerical disk-growth model for a single, isolated rotating disk, assessing the impact of imposed generic radial distributions of temperature. The impact for future engine operational conditions with shorter compressor blades and higher engine pressure ratios is determined.

The first main portion of the thesis describes a thermo-mechanical design of the rig including a titanium disk pack (including thermocouple instrumentation) to ensure operation at 8,000 rpm and 150 °C, with a design life of 10,000 cycles. The design aspects include novel thermocouple grooves to keep stress levels in the elastic range. Key features of the rig include modularity of components and access to the test section. The thermo-mechanical design was produced as an internal report, reviewed and approved by engineers at Rolls-Royce.

The second main portion of the thesis describes the collection and analysis of experimental data over a wide range of non-dimensional operating conditions. The experiments have helped characterise key features of buoyancy-induced rotating flow relevant to engine designers and for the validation of numerical and theoretical models.

The work in this thesis has led to four peer-reviewed journal publications, three of which were presented at annual Turbo Expo for the American Society of Mechanical Engineers.

Acknowledgements

When I think about the long and non-linear journey the PhD studies represented for me, many memories and – more importantly – faces come to my mind. I will make my best to capture all the due acknowledgements I have in these few lines. Despite the common thinking of a PhD as a lonely period, the people I am grateful to is quite long. I believe everybody inspired me in different ways, and I could not achieve this result without.

Without indulging further in rhetoric, I wish to acknowledge Professor Gary Lock for his unceasing support. His ability to spot the good and the positive in every outcome has been a precious teaching to me. I sincerely thank Dr James Scobie for having given me the opportunity to study at the University of Bath and for his understanding supervision. I thank alongside Dr Oliver Pountney and Dr Carl Sangan for their always-friendly advice.

I reserve a special acknowledgement for Professor J. M. Owen. I consider an outstanding privilege having worked with him, and I felt honoured by his time and his trust. I wish to thank also Dr Hui Tang for the kind help I received and Dr Mauro Carnevale for the inspiring chats we had.

I had the opportunity to work side by side with two extraordinary researchers as Dr Marios Patinios and Dr Richard Jackson, who I am proud to call friends. I am glad for the time we spent together and the teachings they gifted me.

In the varied and changing environment of the PhD office there is a group of people I am keen to thank. First, I must acknowledge my dearest friend and flatmate Burak. He has listened and encouraged me in the harder times offering his wisdom. I sincerely thank also Artur, Fabian, Dimitris, Giove and Onur for the fun we had together. Furthermore, I am grateful to Ernesto, Liam, Josh and Neys for their friendship.

I owe my parents and my brothers a major thank you for backing me in every occasion regardless the distance.

Finally, I am in endless debt of gratitude towards my sweet Livia, to whom this work is dedicated.

Contents

List of Figures

List of Tables

Nomenclature

Symbols

a	inner disk/cavity radius
a^*	radius of the cob outer edge
A	empirical constant of cob convection correlation
A_{disk}	Surface area of the disk
a_f	failure crack size
a_0	initial crack length
b	outer cavity radius
b^*	disk external radius
b'	radius at the outermost thermocouple on disk diaphragm
b''	fatigue coefficient accounting for metal surface state
B	empirical constant of cob convection correlation
Bi	Biot number
Bo	buoyancy number
c	specific heat capacity of the disk material
C	empirical parameter of shroud convection correlation
C_{crack}	crack propagation material property constant
c_p	specific heat at constant pressure
c_s	speed of sound
Co	Coriolis parameter
D	characteristic diameter
d_h	hydraulic diameter
D_s	specific diameter
E	Young’s modulus
Ek	Ekman number
$\boldsymbol{F}$	body force vector
G	gap ratio of the cavity (s/b)
G_{CB}	cold-build tip clearance
G_{tip}	blade tip clearance
Gr	Grashof number (based on centripetal acceleration)

Gr_D	Grashof number based on the characteristic diameter
h	heat transfer coefficient
$\bar{h}$	averaged heat transfer coefficient
h_0	specific total enthalpy
h_{static}	specific static enthalpy
I	Buoyancy Model integral
k	thermal conductivity
K	power law constant
$k_{e,bending}$	stress concentration factor due to bending
$k_{e,radial}$	stress concentration factor due to radial force
$k_{e,tangential}$	stress concentration factor due to tangential force
K_{IC}	fracture toughness
K_1, K_2	integration constants of radial stress, tangential stress and total growth equations
l	axial length of the disk cob
L	length scale
$\dot{m}$	mass flow rate
$\dot{m}_{fuel}$	mass flow rate of engine fuel
$\dot{m}_{gas}$	mass flow rate of gases at engine exhaust
$\dot{m}_i$	mass flow rate of the internal air system
$\dot{m}_{tot}$	total compressor mass flow rate
Ma	Mach number
N	thrust force
n_{crack}	crack propagation material property constant
n_{ex}	power law exponent
N_f	number of fatigue cycles to failure in case of crack
n_s	specific rotational speed
Nu	Nusselt number
Nu_L	Nusselt number based on the length scale L
Nu_D	Nusselt number based on the characteristic diameter D
$\overline{\mathrm{Nu}}$	averaged Nusselt number
p	pressure
$\tilde{p}$	reduced pressure

Pr	Prandtl number
q	heat flux
Q	volume flow rate
$\dot{Q}$	thermal power
$\dot{Q}_{l,tot}$	total heat loss
r	radial direction
$\boldsymbol{r}$	position vector
R	stage reaction
R_{air}	specific gas constant of air
r_s	shaft radius
Re_L	rotational Reynolds number for cob
Re_T	rotational Reynolds number for cob
Re_z	axial Reynolds number
Re_ϕ	rotational Reynolds number
$\mathrm{Re}_{\phi,x}$	local rotational Reynolds number
Ro	Rossby number
s	cavity axial gap at the inner radius
s'	cavity axial length
t	time
T	temperature
t_d	disk diaphragm thickness
T^*	non-dimensional temperature of the flat plate $(= (T - T_o)/(T_\infty - T_o))$
T_∞	freestream temperature for the flat plate
$\boldsymbol{u}$	absolute velocity vector (components are u_r, u_ϕ, u_z)
$\lvert\boldsymbol{u}\rvert$	magnitude of absolute velocity vector
u	relative radial velocity
U	velocity for the rotational Reynolds number for cob
U_{air}	velocity of air incoming to the engine
U_{jet}	velocity of gases at the engine nozzle exit
u_r	absolute radial velocity
u_z	absolute axial velocity
U_0	reference velocity
U_∞	freestream velocity for the flat plate

u_{ϕ}	absolute tangential velocity
v	relative tangential velocity
V	volume
w	relative axial velocity
$\boldsymbol{w}$	relative velocity vector (components are u, v, w)
$\widetilde{w}$	specific work
W	axial velocity of through-flow
$\widetilde{w}_C$	compressor specific work
$\widetilde{w}_{cycle}$	specific work of gas turbine cycle
$\widetilde{w}_{stage}$	specific work of compressor stage
x	non-dimensional radius (r/b)
$\tilde{x}$	coordinate of the flat plate
X_f	fatigue safety factor
Y	crack shape factor
z	axial direction
z^*	non-dimensional z direction ($= z/L$ in the flat plate)
α	thermal expansion coefficient
α'	absolute flow angle
β	volumetric expansion coefficient
$\beta\Delta T$	temperature difference between metal at cavity outer radius and through-flow temperature, divided by the through-flow temperature
γ	heat capacity ratio
δ	radial growth
δ_t	thermal boundary layer thickness
δT	temperature difference between fluid in the Ekman layer and in the core
$\Delta\sigma$	cycle stress range
η_C	compressor efficiency
η_{cycle}	efficiency of gas turbine cycle
η_p	polytropic efficiency
η_{prop}	propulsive efficiency
η_T	turbine efficiency
η_{tt}	total-to-total efficiency

ϑ	Ekman spiral angle
θ	non-dimensional disk temperature ($= (T_o - T_c)/(T_{o,b} - T_{c,b})$)
Θ	non-dimensional disk temperature considering the outermost thermocouple on the diaphragm ($= (T_o - T_f)/(T_{o,b'} - T_f)$)
μ	dynamic viscosity
ν	Poisson's ratio
π	pressure ratio of gas turbine cycle
ρ	density
σ_a	alternated stress
σ_{eq}	equivalent (von Mises) stress
σ_m	mean stress
σ_N	fatigue strength at N number of cycles
σ_r	radial stress
σ_t	tangential stress (or circumferential or hoop stress)
σ_y	yield strength
τ	temperature ratio of gas turbine cycle (highest-to-minimum)
τ_c	time constant
τ_r	radial shear stress
τ_ϕ	tangential shear stress
ϕ	tangential direction
ϕ'	relative tangential direction
Φ	flow coefficient
ψ	stage loading
Ω	rotational speed
$\mathbf{\Omega}$	rotational speed vector

Subscripts

a	value at $r = a$
a^*	value at $r = a^*$
b	value at $r = b$
b'	value at $r = b'$
b^*	value at $r = b^*$
BT	blade tip

c	core, based on the core; denotes “theoretical” values in case of quantities like Gr, Nu, h
cob	cob
CS	casing
d	disk diaphragm
E	thermal expansion
f	through-flow, based on through-flow temperature (when applied to quantities like Gr, Nu, h)
o	at metal surface
r	radial
R	rotational
rec	recovery
s	isentropic
sh	shroud
SS	steady state
T	thermal
TOT	total
unf	unfeatured
x	lateral direction
y	vertical direction
z	axial
ϕ	tangential

Superscripts

$diaphragm$	value at the disk diaphragm
hub	value at the disk inner radius
$shroud$	value at the shroud

Abbreviations

CFD	Computational Fluid Dynamics
DNS	Direct Navier-Stokes
FEA	Finite Element Analysis
HP	High Pressure

HPC	High Pressure Compressor
IPC	Intermediate Pressure Compressor
LDV	Laser-Doppler Velocimetry
LES	Large Eddy Simulations
OPR	Overall Pressure Ratio
RANS	Reynolds Averaged Navier-Stokes
SAS	Secondary Air Systems
TIT	Turbine Inlet Temperature
TSFC	Thrust-Specific Fuel Consumption

Chapter 1

Introduction

Starting from a historical overview, this chapter summarises the background knowledge on gas turbines and propulsion theory, aiming to access the current designs of modern engines. Internal air systems and in particular high pressure compressor cavities are presented, since they constitute the main topic of the work in this thesis.

1.1 BRIEF HISTORY OF GAS TURBINES FOR AVIATION

The term “turbine” in its own modern meaning was used for the first time in 1820 by C. Burdin. However, evidence of elementary turbomachines dates back many centuries. In the II century BC, Hero of Alexandria invented the first steam turbine (“aeolipile”), using a heated rotating chamber from which steam would emerge through a pair of bent pipes.

The first prototype of a partial gas turbine was proposed by John Barber (1791), who also gave a physical understanding of the working principle. According to his patent, a reciprocating compressor passes air and combustible gases to burn in a chamber and ultimately into a turbine to generate power. The poor technology of the time prevented Barber and many later inventors to take advantage of their patents. J. F. Stolze was the first to conceive the schematic of a modern gas turbine cycle (1872), but the low efficiencies of the turbomachines – especially the compressor – prevented the invention from being a success. The first gas turbine able to produce net power (15 kW) was designed and built by A. Elling in 1903. From that moment, the development of the technology and the performance accelerated. In 1939, the first simple-cycle gas turbine power plant was built in Neuchâtel, Switzerland, by Brown Boveri: it delivered 4 MW of electric power. In 1988, ASME declared this power plant a Historic Mechanical Engineering Landmark, a “status reserved for milestones of outstanding technical development”.

An impressive development of gas turbines started in the 1940s, when enormous potential was seen in the aviation sector, at first military, then civil. The idea of using a gas turbine for jet propulsion was patented in France by M. Guillaume (1921). However, a significant turning point was in 1930, when F. Whittle got a patent and started to build a turbojet engine featuring a centrifugal compressor, a turbine and a single combustion chamber. From 1936, A. A. Griffith and H. Constant began the development and testing of axial compressors. The first flight propelled by a turbojet was made in 1939 in Germany, with an engine designed by H. von Ohain. Meantime, Whittle received funding for the W1 engine, which flew for the first time in 1941.

During the Second World War, the United Kingdom and Germany made notable efforts to produce turbojet engines at large scale. The efforts resulted in a rapid and almost entire replacement of reciprocating engines in aviation. A number of companies led the development, some of which are still major competitors today (Rolls-Royce, General Electric and Pratt & Whitney). Components, materials and fuels were rapidly and scientifically improved as the technology developed rapidly after the Second World War.

The quest for thermal efficiency through higher turbine inlet temperature and cycle pressure ratio started in the 1950s, and it is still crucial today. New engine configurations have been launched to meet unequalled performance. For example, General Electric tested the first turbofan engine in 1957, while Rolls-Royce developed the first three-shaft engine in 1967. From the 1970s, noise reduction, lower emissions and fuel cost became additional drivers of engine developments. High bypass turbofans were progressively introduced to meet environmental targets and face high fuel cost.

Gas turbines allow aircraft to fly much faster with reduced weight and size. Today, a number of different engine types are available for aircraft (twin spools, three-spools, high bypass, propfan, turboprop and so on), but they all represent inevitable developments of Whittle’s original engine. Turbine cooling, blade technology, increased thrust-to-weight ratio, aerodynamic modelling and many other technologies underpin the outstanding level of performance that aero-engines have reached. This technology is sophisticated, reliable, efficient and clean.

In recent years, the confidence in electric aircraft is slowly increasing. However, gas turbines for aviation will be still dominant in the next decades.

1.2 GAS TURBINES THEORY AND ENGINE CONFIGURATIONS

Starting from the thermodynamic cycle, this section briefly presents the basic theory behind gas turbines for aviation and the configurations they assume in modern engines, focusing mainly on the compressor. The engine figures of merit relevant for this work are discussed.

1.2.1 Brayton-Joule cycle

The reference thermodynamic cycle of a gas turbine and the equipment required were studied by J. P. Joule and later by G. B. Brayton (Figure 1.1). Air, i.e. the working fluid, undergoes four transformations:

1) Adiabatic compression: work is provided such that air is compressed. The ideal transformation 1-2 differs from the real transformation 1-2’ because of irreversibilities in the compressor, ending in point 2’ rather than 2 (same pressure but higher entropy).
2) Isobaric heating: the compressor discharges the air to the combustion chamber, where fuel is added and combustion provides heat to reach point 3. In the real case, losses reduce slightly the pressure (point 3’). The maximum temperature is limited by the material of the turbine.
3) Adiabatic expansion: air and combustion gases expand in a turbine, extracting their enthalpy and providing work, which partly drives the compressor and partly feeds a user. Once again, irreversible processes in the turbomachine (3’-4’) reduce the amount of useful work compared to the ideal case, shifting the end of the expansion to higher entropy.
4) Isobaric cooling: a fictitious transformation for open loop gas turbines (as all those used in engines), where the flow is discharged to the atmosphere and air with the same initial properties enters to the cycle.

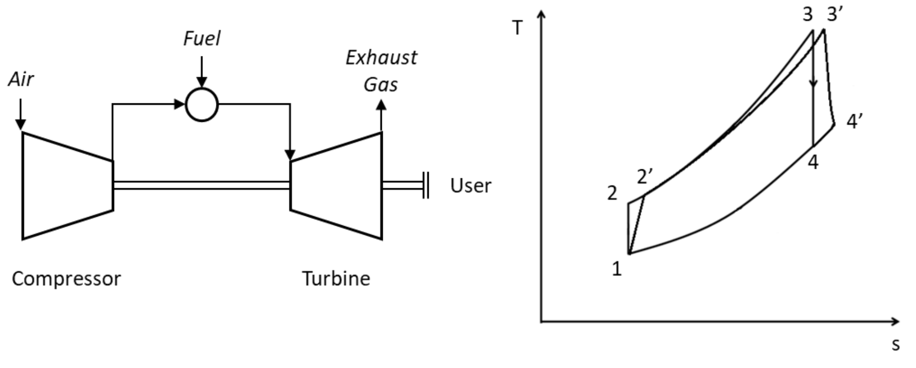

Figure 1.1 – Simple scheme of an open cycle gas turbine (left) and Brayton-Joule cycle in ideal and real case (right).

The efficiency η_{cycle} and the net specific work w_{cycle} of the real cycle are:

$$\eta_{cycle} = \frac{\tau\eta_{T,s}\left(1-\frac{1}{\pi^{\frac{\gamma-1}{\gamma}}}\right)-\frac{1}{\eta_{C,s}}\left(\pi^{\frac{\gamma-1}{\gamma}}-1\right)}{\tau-\frac{1}{\eta_{C,s}}\left(\pi^{\frac{\gamma-1}{\gamma}}-1\right)-1} \qquad (1.1)$$

$$\frac{w_{cycle}}{c_p T_1} = \tau \eta_{T,s} \left(1 - \frac{1}{\pi^{\frac{\gamma-1}{\gamma}}} \right) - \frac{1}{\eta_{C,s}} \left(\pi^{\frac{\gamma-1}{\gamma}} - 1 \right) \tag{1.2}$$

where π is the pressure ratio p_2/p_1, τ is the temperature ratio T_3/T_1, γ is the heat capacity ratio, c_p is the specific heat at constant pressure, $\eta_{C,s}$ and $\eta_{T,s}$ are the compressor and turbine isentropic efficiencies, respectively. The isentropic specific work of the compressor is expressed as:

$$\frac{w_{C,s}}{c_p T_1} = \frac{\pi^{\frac{\gamma-1}{\gamma}}}{\eta_{C,s}} \tag{1.3}$$

The work available for the user is equal to the work produced by the turbine reduced by the work absorbed by the compressor. The figures of merit of the cycle are:

- The pressure ratio π
- The turbine inlet temperature T_3 (TIT)
- The isentropic efficiency of the compressor $\eta_{C,s}$
- The isentropic efficiency of the turbine $\eta_{T,s}$

Figure 1.2 shows the dependency of the specific work and the cycle efficiency on the pressure ratio and the TIT (specifically τ). For each τ, the specific work features a peak value at a certain pressure ratio. Also the cycle efficiency has a maximum for each τ, but at a higher pressure ratio and with a rather flat behaviour around the peak. Any increase of τ results in an increase of the specific work output, which in turn means a reduction in size for a given power, which is always beneficial. Consequently, the cycle needs a higher pressure ratio to take advantage of the higher permissible temperature.

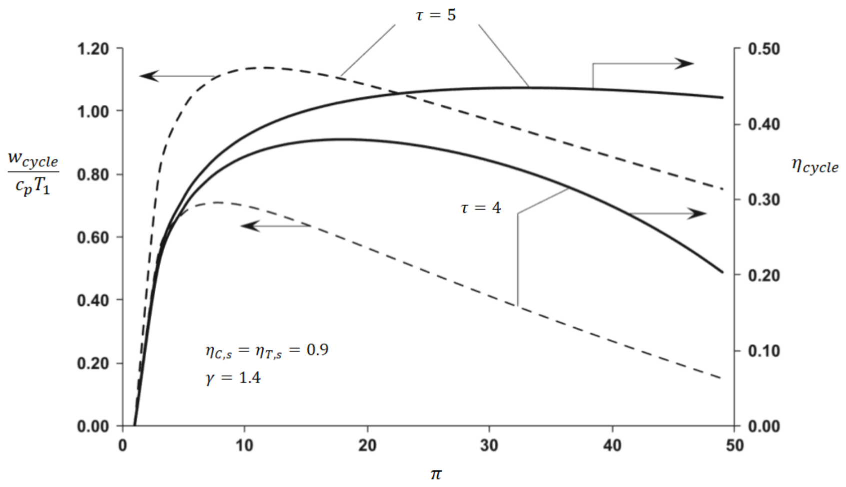

Figure 1.2 – Variation of specific work and efficiency of the cycle with pressure ratio and turbine inlet temperature, adapted from Sultanian 2018.

In an aero-engine, the turbine extracts from the flow just enough work to drive the compressor and fan, to win the mechanical losses and to provide the power off-takes needed by the engine and the aircraft. As a result, a considerable amount of enthalpy is left in the exhaust gases. A nozzle is placed at the turbine outlet to let the flow expand adiabatically: this constitutes the basis of jet propulsion. The nozzle represents the actual user of the enthalpy of the gases. In any case, the figures of merit are the same, with the pressure ratio across the engine typically called overall pressure ratio (OPR). Research and development of gas turbines aim to achieve high efficiency through the performance of components ($\eta_{C,s}$ and $\eta_{T,s}$) and also by increasing both OPR and TIT. Figure 1.3 reports the evolution of the OPR and TIT over the last decades. As it is discussed in Sections 1.3 and 1.4, the quest for higher OPRs has impact on the compressor cavities, which are the object of this thesis.

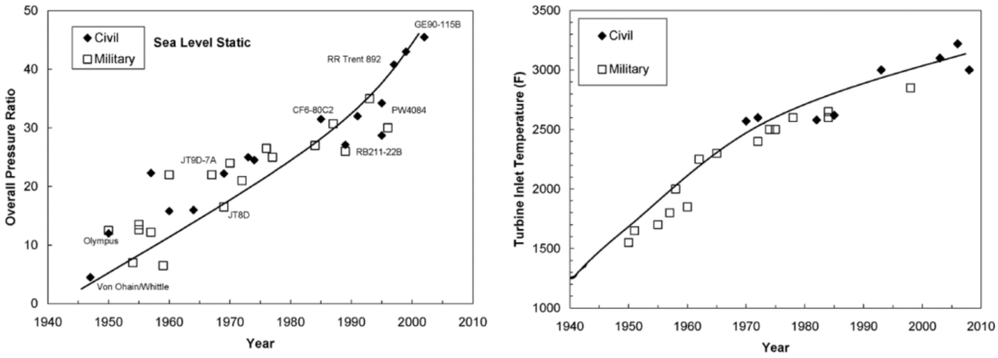

Figure 1.3 – OPR and TIT of civil and military engines between 1939 and 2003, adapted from Ballal et al. 2004.

1.2.2 Axial compressor theory

Modern gas turbines for aero-engines feature axial compressors, i.e. axial turbomachines able to increase the pressure of a continuous flow. In their simplest scheme, rotor and stator rows are the two functional components. In the rotor, the kinetic energy of the flow increases owing to the work exchange between blades and fluid, and then it is partially converted to pressure. In the stator, the flow diffuses, reducing the kinetic energy again in favour of pressure. The Euler equation computes the specific work of a single compressor stage:

$$\widetilde{w}_{stage} = \Omega r(|\boldsymbol{u}_2| \cos \alpha'_2 - |\boldsymbol{u}_1| \cos \alpha'_1) = \Omega r(u_{\phi,2} - u_{\phi,1}) \qquad (1.4)$$

Definitions of the symbols used are reported in nomenclature, while the indices 1 and 2 represent velocities at the inlet and at the outlet of the rotor, respectively. The diagrams in Figure 1.4 are named velocity triangles, and contain all the basic quantities to retrieve the non-dimensional parameters describing the stage:

- Flow Coefficient:

$$\Phi = \frac{|\boldsymbol{u}_1| \sin \alpha_1'}{\Omega r} = \frac{u_z}{\Omega r} \tag{1.5}$$

- Stage Loading:

$$\psi = \frac{\left(h_{0,1} - h_{0,2}\right)}{(\Omega r)^2} \tag{1.6}$$

- Stage Reaction:

$$R = \frac{h_{static,1} - h_{static,2}}{h_{static,1} - h_{static.3}} \tag{1.7}$$

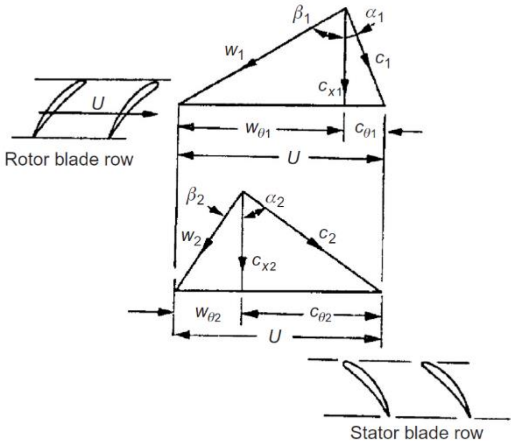

Figure 1.4 – Velocity triangles of an axial compressor stage, adapted from Dixon 2014. Symbols are defined in Dixon 2014.

The compression process operated by the single stage is not isentropic, due to thermodynamic and kinetic losses. Thermodynamic losses emerge from entropy creation within the stage and are related to 2D and 3D flow effects, such as blade tip leakages. Kinetic losses are the kinetic energy left to the flow at the stage outlet.

The isentropic efficiency introduced in Section 1.2.1 can be expressed, for a stage, as total-to-total efficiency, i.e. the ratio between total enthalpy change across the stage in the ideal and in the real case:

$$\eta_{tt} = \frac{h_{0,3s} - h_{0,1}}{h_{0,3} - h_{0,1}} \tag{1.8}$$

where h_0 is the total enthalpy and index 3 refers to stage outlet. Total-to-total efficiency does not consider the kinetic losses, since the kinetic energy left in the flow is useful for the following stage. Axial machines accommodate high mass flow rates at the cost of a reduced pressure ratio of the single stage. More stages can be placed one after the other to build up the desired pressure ratio. The isentropic efficiency of a multi-stage compression process is dependent on the pressure ratio itself and is always lower than the single stage efficiency, due to the reheat effect. Thus, to compare two compressors, the polytropic efficiency η_p is commonly used. It can be considered the efficiency of a small infinitesimal compression and, by integration, can be linked to the isentropic efficiency:

$$\eta_{C,s} = \frac{\pi^{\frac{\gamma-1}{\gamma}} - 1}{\pi^{\frac{\gamma-1}{\gamma\eta_p}} - 1} \tag{1.9}$$

1.2.3 Propulsion and engine configurations

The majority of aircraft are powered by jet engines, i.e. engines generating fast gas jets for propulsion. The turbojet engine is depicted in Figure 1.5. The main components are a compressor, a combustion chamber, a turbine and an expansion nozzle.

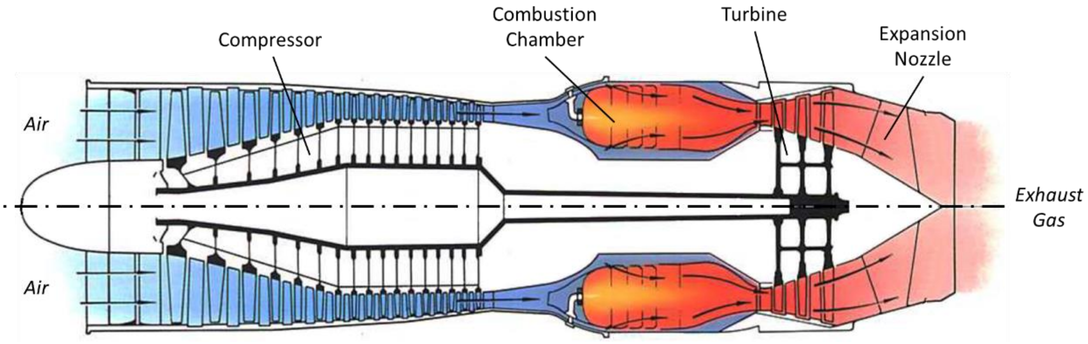

Figure 1.5 – Scheme of a turbojet engine, adapted from Rolls-Royce 1996.

The turbine powers only the compressor, leaving in the exhaust gases a significant amount of enthalpy, which is converted to kinetic energy by the nozzle, resulting in a thrust force N in the opposite direction:

$$N = \dot{m}_{gas}(U_{jet} - U_{air}) \tag{1.10}$$

where $\dot{m}_{gas}$ is the exhaust gas mass flow rate, U_{jet} is the velocity of the gas expelled by the nozzle, U_{air} is the incoming air velocity. The specific thrust is obtained dividing the thrust by the mass flow rate of the gas ejected by the engine ($N/\dot{m}_{gas}$). The propulsive efficiency η_{prop} is:

$$\eta_{prop} = \frac{2U_{air}}{U_{air} + U_{jet}} \tag{1.11}$$

To produce more thrust (i.e. higher payloads or higher performance of the aircraft), a turbojet engine has to increase either $\dot{m}_{gas}$ or U_{jet}. Increasing the gas flow rate has a limit: higher-size engine nacelles capture more air, but result in additional aerodynamic drag (which in turn has to be overcome by additional thrust). Increasing the jet exit velocity, instead, results in low propulsive efficiency. To overcome this impasse, turbofan engines have been proposed (Figure 1.6), and these are the most common solution for civil aircraft propulsion.

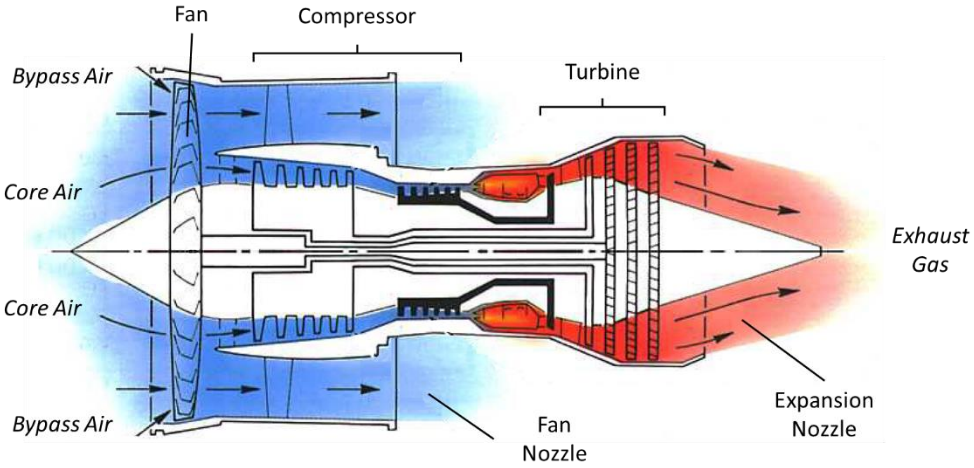

Figure 1.6 – Scheme of a Turbofan engine (high bypass), adapted from Rolls Royce 1996.

The turbofan represents a modification of the turbojet engine invented by F. Whittle. All the incoming air is ingested by the fan, but only part of it proceeds through the core. The two streams expand in separate nozzles but both contribute to the thrust. For given aircraft velocity (U_{air}) and jet velocities, a fan with a high-diameter captures more air, resulting in more thrust for the same propulsive efficiency. The ratio between the two air streams (non-core air to core air) is called bypass ratio. For a required thrust, higher bypass means higher propulsive efficiency. However, high fan diameters are only possible with low rotation speeds and advanced blade materials. A widely used figure of merit of an aircraft engine is the thrust-specific fuel consumption (TSFC):

$$TSFC = \frac{\dot{m}_{fuel}}{N} \tag{1.12}$$

Turbofan engines have much lower values of TSFC compared to turbojet engines (at least at subsonic speeds).

The TSFC and the specific thrust of turbojet and turbofans are strongly dependent on the TIT and the OPR, as shown in Figure 1.7. As the OPR increases, the fuel consumption always reduces. For an increased TIT, instead, both the specific thrust and the TSFC increase. Therefore, any increase in specific thrust – driven by engine and aircraft compactness – must be compensated by an increase of OPR to balance the penalty in the fuel consumption. Turbofan engine designs have two additional parameters affecting the TSFC, i.e. the fan pressure ratio and the bypass ratio. However, for a given OPR, there exist a minimum TSFC for a certain value of fan pressure ratio and bypass ratio (Cohen et al. 1996). Although the optimisation procedure may be long, it is evident that higher specific thrust, higher OPR and higher bypass ratio are key to reduce specific fuel consumption of the engine improve the economics of the aircraft operation.

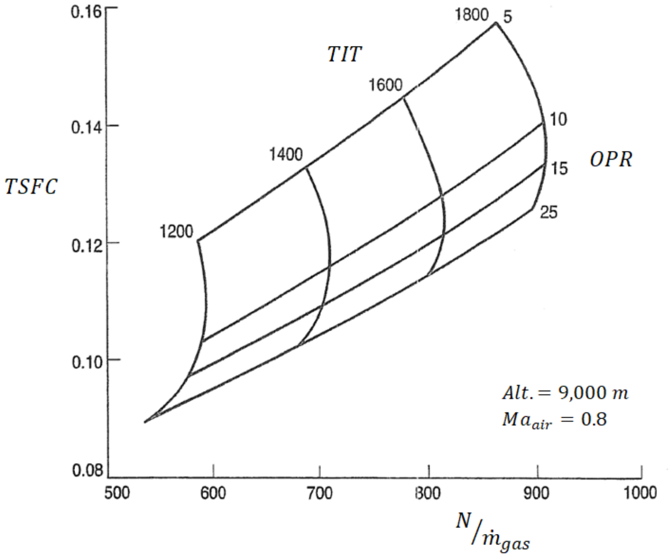

Figure 1.7 – Effect of turbine inlet temperature and overall pressure ratio on thrust-specific fuel consumption and specific thrust for a turbojet at subsonic speed, adapted from Cohen et al. 1996.

1.2.4 Compressor configurations

The quest for low TSFC requires higher TIT and OPR. However, the performance of the compressor and the turbine are also crucial. For turbomachines, the highest efficiency is attained for particular combinations (laying on the Cordier line, Dixon 2014) of the specific speed n_s and the specific diameter D_s, i.e. two non-dimensional parameters defined as:

$$n_s = \Omega \frac{\sqrt{Q}}{\widetilde{w}_s^{3/4}} \tag{1.13}$$

$$D_s = D \frac{\widetilde{w}_s^{1/4}}{\sqrt{Q}} \tag{1.14}$$

where Ω is the rotational speed, Q the volume flow rate, $\widetilde{w}_s$ the isentropic work per unit mass, D the characteristic diameter. A cycle with high pressure ratio leads to high volume flow rates at the inlet of the compressor and very low volume flow rate at the outlet; the opposite for the turbine. As the specific volume of air varies throughout the compression process, the combination of specific speed and specific diameter for the optimum efficiency changes. Hence, it is beneficial to split both compressor and turbine, fitting them in two spools rotating at different speeds. In high bypass ratios, the fan diameter can be such that a third rotational speed is needed. This is required to limit centrifugal stresses. The two solutions deployed by the engine manufacturers are the three-spool engines and the geared turbofan engines. Figure 1.8 shows a cross-section of the Trent1000, a high bypass three-spool turbofan.

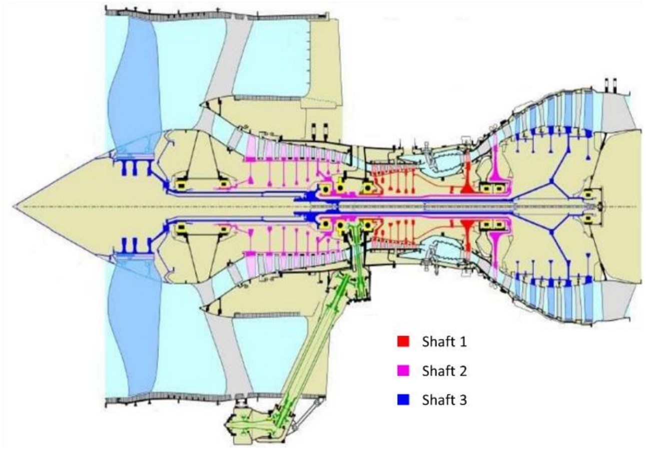

Figure 1.8 – Cross-section RR Trent1000, a three-spool turbofan engine, adapted from Ohja and Ragava.

The compression process of modern engines is broken into more consecutive stages. Each compressor is driven by its own turbine at an optimum rotation speed. The main subassemblies of a compression system are:

- Nose cone, responsible of smoothing the flow and resist to external objects potentially ingested (such as ice).
- Fan, which increases the pressure of the bypass airflow for nozzle expansion and supercharges the core airflow for the core compressor(s). A few stages can be fitted on the same shaft of the fan, named booster stages.
- Core compressor(s), acting on the core airflow. These compressors increase the pressure for the cycle and for the thrust, provides air bleeds for multiple functions.

The core compressor is made up by one or two axial compressors with a variable number of stages, depending on the application. Large civil engines usually feature two core compressors with two or three shafts. The first compressor is named intermediate pressure compressor (IPC), the second is named high pressure compressor (HPC). Small civil engines and military engines fit one core compressor with two shafts (booster stages typically fitted on the fan shaft). Figure 1.9 shows a cross-section of the Trent500, a high bypass three-spool turbofan.

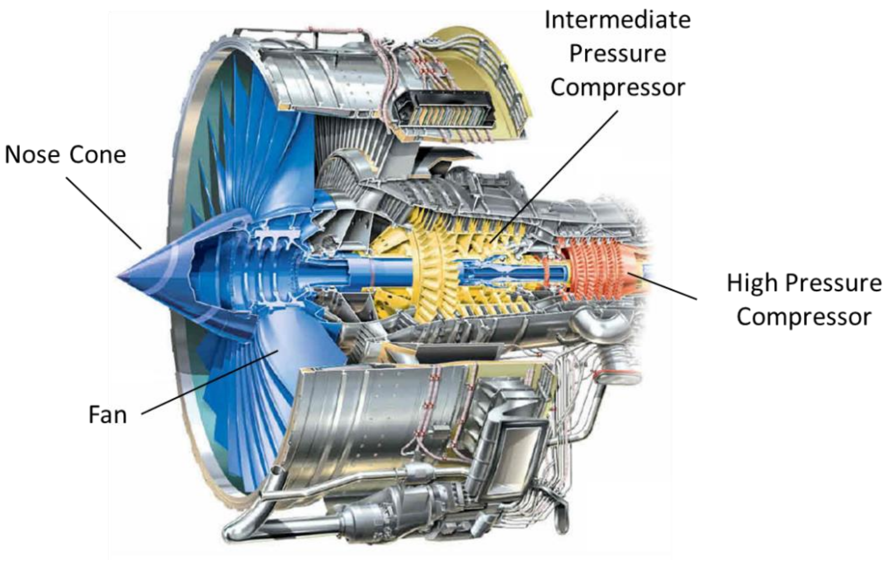

Figure 1.9 – Compression system of a RR Trent500, a high bypass turbofan, adapted from Rolls-Royce 2015.

In a compressor, rotor blades are attached to disks with different fixing arrangements, and disks are welded or bolted to each other. Due to the reduced size in the last stages of the HPC, the blades can be machined as part of the disk, constituting a "blisk". The resulting rotor geometry is a disk stack, which builds up successive cavities. The stator vanes are mounted on the casing.

A compressor disk is made up by a thick ring at the inner radius (called "cob"), a thin diaphragm and an external shroud. Mechanical, thermal and inertial stresses can be significant. Additionally, the thermal response of a disk is crucial in the engine response due to aircraft manoeuvres. Integrity is a key task for a sound compressor design: there is a balance between component integrity, safety and minimisation of the disk weight.

The next generation of aero-engine compressors aims at higher bypass, higher pressure ratios and higher efficiency. At the same time, lower cost, weight and noise must be achieved. All these targets require fundamental understanding of the governing aerodynamics, mechanics, materials and manufacturing.

1.3 INTERNAL AIR SYSTEMS IN MODERN GAS TURBINES

Air, oil and fuel systems are crucial for the operation of the engine. The present work is framed within air systems. Up to 20% of the incoming air is extracted from the compressor for the purposes of internal or external systems (Rolls-Royce 1996). External systems include services such as cabin pressurisation and conditioning. The internal air, instead, performs a number of vital tasks and, together with the hardware features arranged to guide it, constitutes the internal air system (also referred to as the secondary air system).

1.3.1 Role of internal air systems

Internal air systems divert air from the compressor to achieve three main goals (Figure 1.10):

- Cooling of engine components. Many metal components, such as turbine blades, vanes and casing, are exposed to hot air (up to 1,500 °C). In the last stages of the HPC metal temperatures reach 700 °C. Cooling is required either to prevent melting or to extend life. The location within the compressor where the air is extracted depends on the service temperature and pressure. For example, HP turbine blades are cooled with air from the HPC outlet, whereas the volume comprised within the HPC rotor and the shaft is filled with air drawn from the outlet of the IPC. Disks and shafts are structural components demanding integrity at all conditions. Limiting the disk maximum operating temperature increases reliability and allows weight reduction.
- Sealing flow paths and bearing chambers. Any leakage among the engine parts lowers the overall performance. Seals are deployed between stationary and rotating, co-rotating or contra-rotating parts. Bearing chambers are typically air-sealed.
- Bearing load control. Flow interaction with blades and vanes in turbines and compressors generates axial forces in opposite directions, which have to be taken by the thrust bearings. The internal air system contributes to balance the loads by pressurising disks and shafts.

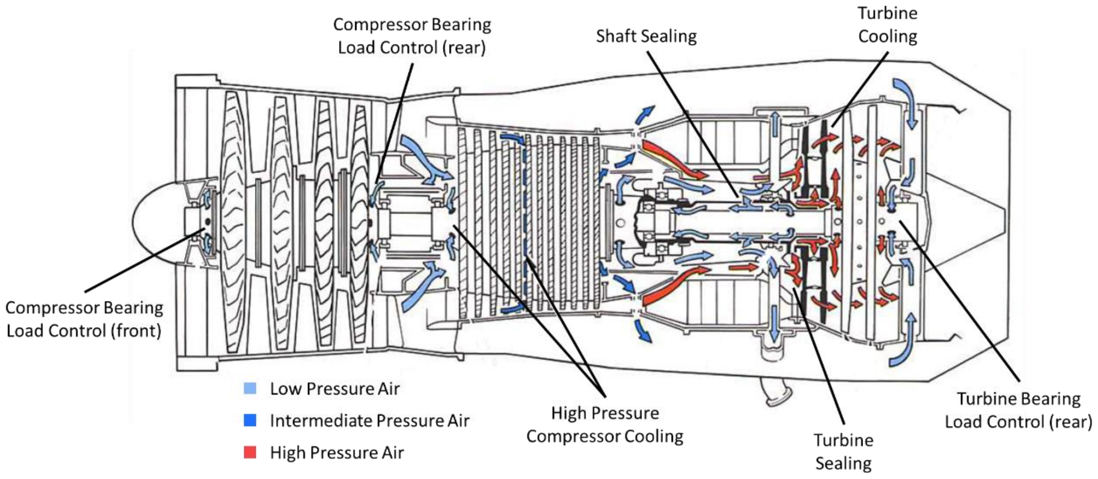

Figure 1.10 – Internal air system of a low bypass turbofan, adapted from Rolls-Royce 1996.

1.3.2 Relevant elements of internal air systems

Internal air systems are built up by a collection of components belonging to three categories: flow passages (ducts, slots, orifices), seals and cavities. Passages are communication means for air to move from one side to the other. Seals prevent or minimise air displacement between two separate volumes of the engine. Disks and static structures create axisymmetric features known as cavities. They make up a significant amount of the engine cross-section and are of utmost importance for integrity and performance.

Co-rotating compressor cavities are the subject of this work. A variation of temperature and pressure occurs when air enters, exits and passes a cavity. The flow rate, rotating speed, initial flow direction (e.g. radially inward or outward) affect the flow field.

In internal air systems, vortices are a common flow feature. Pure free vortex structures are seldom found due to friction at the walls. Solid body rotation occurs as the flow interacts with rotating walls and is forced to their rotation speed. In compressor cavities, however, the flow structure can be far from these two extremes, and further complicated by radial inflow or superposition of an axial through-flow.

1.3.3 Impact on engine performance

Flow through features such as cavities is relevant for the overall energy balance of the system. The amount of air extracted corresponds to a loss of 5% of fuel energy. It must be reduced as much as possible by optimising geometries, flow paths and heat transfer. To assess the impact of the internal air systems on gas turbine performance, let us consider:

- A Brayton-Joule cycle whose compressor and turbine have constant isentropic efficiency;
- Part of the internal air flow rate takes part to the turbine expansion (air used for blade cooling), the rest does not ($\dot{m}_i$);
- Negligible fuel mass flow rate and combustor pressure drop.

The work output and the efficiency are (Sultanian 2014):

$$\eta_{cycle} = \frac{\tau \eta_{T,s}\left(1 - \frac{1}{\pi^{\frac{\gamma-1}{\gamma}}}\right) - \frac{1}{\left(1 - \frac{\dot{m}_i}{\dot{m}_{tot}}\right)\eta_{C,s}}\left(\pi^{\frac{\gamma-1}{\gamma}} - 1\right)}{\tau - \frac{1}{\eta_{C,s}}\left(\pi^{\frac{\gamma-1}{\gamma}} - 1\right) - 1} \qquad (1.15)$$

$$\frac{w_{cycle}}{c_p T_1} = \left(1 - \frac{\dot{m}_i}{\dot{m}_{tot}}\right) \tau \eta_{T,s} \left(1 - \frac{1}{\pi^{\frac{\gamma-1}{\gamma}}}\right) - \frac{1}{\eta_{C,s}} \left(\pi^{\frac{\gamma-1}{\gamma}} - 1\right) \tag{1.16}$$

Compared to (1.1) and (1.2), the previous equations show that the internal air must be used wisely to maintain the engine performance.

The design of internal air systems needs to be robust across the widest operating envelope, using a minimum amount of air and retaining acceptable performance. Aging of the engine, presence of solid particles in air and aircraft manoeuvres are all potential threats for system integrity. One-dimensional modelling considers the hardware elements of internal air systems interconnected in networks. This is a common tool for design optimisation and monitoring.

1.4 COMPRESSOR CAVITIES

The cavities of a high pressure compressor are located underneath the core flow path. Each cavity is formed between two disks connected at the outer radius by a shroud, as in Figure 1.11. Blades are at the rim of the disks, with stator vane seals preventing leakage at the outer shroud. Aero-engine cavities locate an axisymmetric volume together with the shaft.

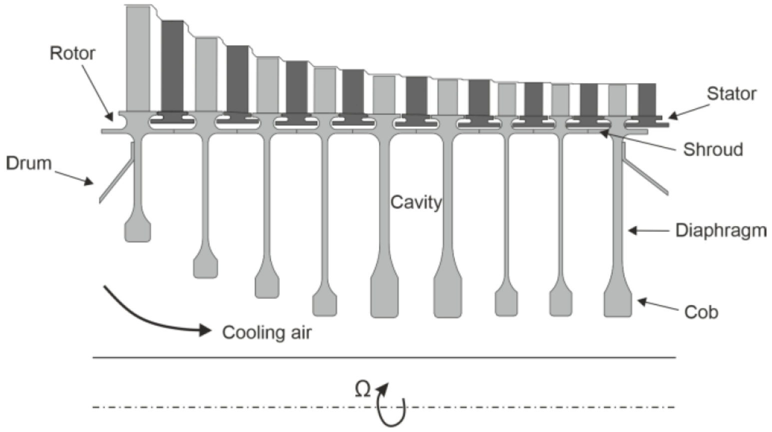

Figure 1.11 – Cross-section of a high pressure compressor featuring the cavity stack and a through-flow of cooling air, adapted from Jackson et al. 2021.

The interest for compressor cavities lays in the fact that they contribute significantly to the running blade-tip clearance. The necessary gaps between rotating blades and casing give rise to leakage flows at the tips, which are a secondary flow loss. Tip leakage flows reduce the total-to-total efficiency and are responsible for about one third of the total stage loss (Denton 1993). As the air progresses through the compressor stages, the adiabatic increase in density is associated with the temperature rise. The flow heats blades, vanes and all wetted surfaces. Blades are attached to the disks, which are also heated. The tip gap – i.e. the distance between the blade tip and the inner casing surface – results from the growth of the casing, the blades, the disks and the shroud. The tip leakage loss is more intense as the blades become shorter relative to the finite gap size, which happens in the latter stages of the compressor. From the overall energy balance perspective, losses in those stages are even more significant. From current values of 50:1, the OPR of the next generation of aero-engines is anticipated to increase to 70:1, resulting in even shorter high pressure compressor blades in the aft stages.

The internal air system includes air extraction from the outlet of the previous compressor, with the purpose of cooling and controlling the radial growth of the HPC rotor, and ultimately the tip clearance. The cooling air flows axially through the bores of the disk stack, interacting with the flow in the cavities and the disk diaphragm surfaces. The heat transfer and the thermal conductivity of the disk generate a radial temperature distribution, information that is important if the tip clearance and the increase of the stage efficiency are to be calculated.

During manoeuvres, the engine undergoes accelerations and decelerations, resulting in transients, during which the tip clearance is not equal to the steady-state value, owing to differences in thermal inertia of disks, blades, shroud and casing. During the engine life, compressor rotors are cyclically subject to many temperature distributions and non-uniform thermal expansion, giving rise to thermal stresses and intense low-cycle fatigue.

The fundamental understanding of the interplay between the flow field and the heat transfer on the cavity walls informs accurate prediction and modelling of the radial temperature distribution, providing the designer important information. This work is a contribution to that understanding.

1.5 AIM AND OBJECTIVES

The aim of the thesis is to design and commission an experimental test rig to characterise and measure buoyancy-induced heat transfer in rotating cavities simulating an axial compressor. This will progress the understanding of the fluid dynamics and heat transfer within the cavity and provide experimental data to validate theoretical and computational models. Ultimately, the results will support engine designers who use such models as predictive tools. The test rig must meaningfully reproduce and investigate all possible scenarios encountered in real engine compressors and provide experimental data via a complete set of instrumentation.

The objectives of the thesis are:

- Use a simple numerical disk-growth model for a single isolated rotating disk to answer the following questions:
    - What is the impact of an assumed radial temperature distribution on the growth of a compressor disk? What are the differences in radial growth for different, generic profiles of temperature, including those predicted by the physically-based Owen-Tang Buoyancy Model?
    - Will the impact change in future engines with shorter HPC blades and higher pressure ratios?
    - What speculation can be made (in absence of a transient Buoyancy Model) regarding transients?
- Assess if the design of the rotating disk pack of the Bath Compressor-Cavity Rig (including thermocouple instrumentation) is adequate to fulfil the operational requirements of the experimental rig (8,000 rpm, 150 °C temperature at the external surface, design life of 10,000 cycles). Propose relevant design modifications if needed, without affecting the interface with the non-rotating part of the rig.
- Develop a design to accommodate all relevant instrumentation for heat transfer and fluid dynamics. The rig design must be flexible with respect to the geometries that can be tested. Furthermore, the operating modes of the rig must reproduce operating parameters that are meaningful and relevant compared to real engines.
- Characterise the buoyancy-induced heat transfer in the experimental rig cavity with an extensive data set of steady-state measurements across the rig operating ranges. Understand the underlying physical phenomena and the drivers of the heat transfer in terms of Nusselt number.

1.6 THESIS OUTLINE

Chapter 1 introduces the history of gas turbines for aviation, highlighting the technology and developments for powering aircraft. The basic theory of the Brayton-Joule cycle and axial compressors is briefly reported, followed by the fundamentals of aircraft propulsion. Attention is given to the compressor and its modern configurations. The discussion moves then to the internal air systems of aero-engines, introducing the high pressure compressor cavities and the implications the cooling has in terms of tip clearance control and engine integrity. The aims and objectives of the thesis are stated.

Chapter 2 provides a comprehensive background of previous research on compressor cavities. Basic structures such as free disk pumping and forced vortex are introduced and the theoretical equations for rotating flows reported. Previous experimental work is then critically presented, together with a recent Buoyancy Model for high pressure compressor cavities (Owen and Tang 2015). Existing literature on compressor disk modelling for tip clearance calculation closes the review.

Chapter 3 shows the impact that temperature modelling of the compressor cavity has in terms of tip clearance. By using 1D modelling and 2D finite element analysis, the radial growth of a representative compressor disk is calculated using the Buoyancy Model as a datum for the temperature distribution. Results are then compared to other temperature distributions.

Chapter 4 reports the stress calculations of the rotating parts of the Bath Compressor-Cavity Rig. It is a finite element thermo-mechanical analysis performed with both static and cyclic loads conditions aiming to validate the design through the whole rig life. Critical design changes are suggested to keep the maximum stress values within the elastic limit at the locations of the instrumentation.

Chapter 5 presents the design and commissioning of the Bath Compressor-Cavity Rig. It comprises four disks with engine representative geometry, overhung on a rotating shaft. Instrumentation is deployed in the inner cavity and is detailed throughout the chapter. Modularity and flexibility are the key features, allowing several different conditions and operating ranges to be tested. Successful commissioning is supported by field data, alongside with the capability of the rig to generate sensible data compliant with the basic understanding of the flow features.

Chapter 6 provides the results of a test campaign of steady-state temperature measurements on the experimental rig. Full parameter ranges are investigated for a given geometry of the cavity and results compared with prediction of the Buoyancy Model, showing good agreement. The heat transfer between flow and cavity walls is interpreted in terms of flow structure, highlighting the correlation with the governing parameters and physics.

Chapter 7 concludes the work summarising the key findings. Recommendations for future research is given based on the rig capabilities.

Chapter 2

Literature review

Starting from the free disk, which is the foundation of all rotating flows, this Chapter presents existing literature on rotating cavities, with focus on open cavities having axial through-flow. The theoretical equations are presented to collect the necessary tools for the understanding of the flow behaviour. After a brief overview of the possible configurations of cavities for gas turbines and of the relevant non-dimensional parameters useful to describe them, attention is drawn to experimental research facilities and to a recent theoretical model for buoyancy-induced flow. One of the purposes of the test rig described in this thesis is indeed to complete the validation of that model, though the wider application is for providing data, engine design tools and CFD. Pertinent CFD studies are also briefly outlined, and a review of compressor disk modelling for tip clearance calculation is reported.

2.1 THE FREE DISK

Rotating disks are constitutive elements of internal air systems. The flow field associated to a rotating disk determines the power necessary to overcome the frictional drag (due to the shear), the characteristics of the heat transfer, the temperature distribution and thus the thermal stresses and the thermal expansion. A single fluid dynamics analysis cannot be developed to study such problems as geometry plays an important role. The most basic problem of rotating flows is the free disk. It considers a disk spinning at a constant angular velocity immersed in a viscous fluid.

2.1.1 Free disk-pumping effect

A spinning disk in a non-rotating fluid is illustrated in Figure 2.1. It is assumed horizontal, with the flow stationary at large distances from the solid face. The angular velocity is Ω and the disk radius b, with a cylindrical reference system (r, ϕ, z) to describe the flow. The fluid in contact with the disk surface is forced to rotate at the same angular velocity by the no-slip condition. This results in a linear radial distribution of tangential velocity, which tends to zero as the z coordinate increases and the undisturbed flow is met. In the rotating reference system, centrifugal forces act on the rotating flow, generating an outward radial component of velocity, which is zero at both the disk surface (no-slip) and in the undisturbed flow. Since fluid is ejected at the outer radius, there must be an axial entrainment of flow for the conservation of mass. This phenomenon is called free the disk-pumping effect, and the related outward flow is the pumped flow: the free disk behaves as a bladeless compressor.

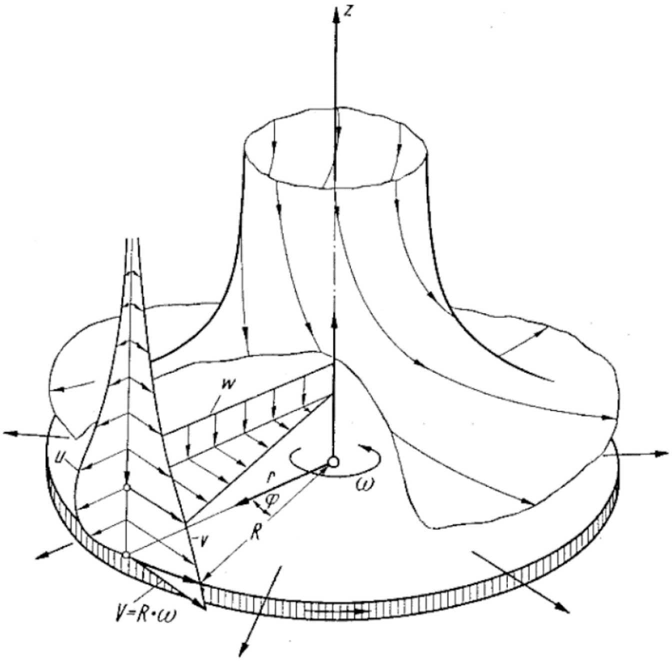

Figure 2.1 – Flow field of the free disk with representation of the boundary layer (Schlichting 2000). Symbols defined in Schlichting 2000.

Compared to the flow over a flat plate, the boundary layer related to the free disk has multi-component velocity and, within the premises of this specific problem, is sometimes referred to as von Kármán layer (Appelquist 2017). The flow in the boundary layer can be laminar or turbulent according to the value of the local rotational Reynolds number defined as:

$$\mathrm{Re}_{\phi,x} = x^2 \frac{\rho \Omega b^2}{\mu} \tag{2.1}$$

where $x = r/b$. In the vicinity of the axis the flow is always laminar; it might undergo transition to turbulent flow as the radius increases.

2.1.2 Generalisation of the free disk

The free disk problem can be generalised when an angular velocity is assigned to the freestream. If the flow rotation speed is less than the disk, the pumping effect will be less intense, with the disk still behaving as a bladeless compressor but with lower outflow rate

(Sultanian 2018). When the flow is rotating and the disk is fixed, the pumping effect is reversed: air is captured radially and discharged axially, hence the disk acts like a bladeless turbine. The related boundary layer is called the Bödewadt layer (Crespo del Arco et al. 2017). In the case where the disk and the flow have similar angular velocity (no matter which one is higher), the resulting boundary layer is called Ekman layer.

Rotating cavities in axial compressors are made up by two co-rotating disks connected at the external radius via the shroud. At steady state, shear stresses at the disk faces induce flow rotation at a speed comparable to that of the cavity and Ekman layers form on the solid walls. These Ekman layers are crucial to the understanding of the heat transfer and they will be presented in more detail in the next section, where the appropriate, governing equations are derived.

2.2 THEORETICAL EQUATIONS FOR ROTATING CAVITIES

In rotating machinery, it can be beneficial to describe the flow structure in a rotating reference frame. This choice makes additional terms arise in the laws of motion, such as the centrifugal and Coriolis accelerations. In this section, the continuity and momentum equations in a frame rotating at Ω are reported, and the linear Ekman layer equations are derived. The derivation is based on Childs 2011. The absolute reference system is (r, ϕ, z), while the relative reference system is (r, ϕ' , z), with $\phi' = \phi - \Omega t$, as shown in Figure 2.2.

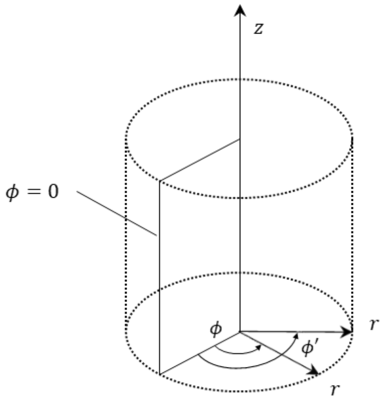

Figure 2.2 – Absolute and relative reference system. The relative reference system rotates at Ω about the z axis with respect to the absolute reference system.

2.2.1 Continuity and momentum equations in a rotating reference system

The continuity equation for a fixed reference system is:

$$\frac{D\rho}{Dt} + \rho\nabla \cdot \boldsymbol{u} = 0 \tag{2.2}$$

The absolute velocity vector $\boldsymbol{u}$ has the three components (u_r, u_ϕ, u_z). The relative velocity vector $\boldsymbol{w}$ has three components (u, v, w) such that:

$$u = u_r \tag{2.3}$$

$$v = u_\phi - \Omega r \tag{2.4}$$

$$w = u_z \tag{2.5}$$

The continuity equation in the rotating reference frame can be written as:

$$\frac{\partial \rho}{\partial t} + \frac{1}{r}\frac{\partial}{\partial r}(\rho r u) + \frac{1}{r}\frac{\partial}{\partial \phi'}(\rho v) + \frac{\partial}{\partial z}(\rho w) = 0 \tag{2.6}$$

The momentum equation for a flow with constant viscosity in the fixed reference system is:

$$\rho\frac{D\boldsymbol{u}}{Dt} = -\nabla p + \mu\nabla^2\boldsymbol{u} + \frac{1}{3}\mu\nabla(\nabla\cdot\boldsymbol{u}) + \boldsymbol{F} \tag{2.7}$$

where $\boldsymbol{F}$ represents the body forces. With the assumption of:

- Incompressible flow (ρ = constant);

the continuity equation (2.6) leads to:

$$\frac{1}{r}\frac{\partial}{\partial r}(ru) + \frac{1}{r}\frac{\partial v}{\partial \phi'} + \frac{\partial w}{\partial z} = 0 \tag{2.8}$$

The momentum equation (2.7) becomes:

$$\rho\frac{D\boldsymbol{u}}{Dt} = -\nabla p + \mu\nabla^2\boldsymbol{u} + \boldsymbol{F} \tag{2.9}$$

Writing the previous equation in the rotating reference frame leads to:

$$\begin{aligned}\rho\frac{D\boldsymbol{w}}{Dt} &= \rho\left[\frac{\partial\boldsymbol{w}}{\partial t} + (\boldsymbol{w}\cdot\nabla)\boldsymbol{w} + 2\boldsymbol{\Omega}\times\boldsymbol{w} + \boldsymbol{\Omega}\times(\boldsymbol{\Omega}\times\boldsymbol{r})\right]\\ &= -\nabla p + \mu\nabla^2\boldsymbol{w} + \boldsymbol{F}\end{aligned} \tag{2.10}$$

where

$$\boldsymbol{u} = \boldsymbol{w} + (\boldsymbol{\Omega}\times\boldsymbol{r}) \tag{2.11}$$

In components form, equation (2.10) can be expanded as:

$$\begin{aligned}&\rho\left[\frac{\partial u}{\partial t} + u\frac{\partial u}{\partial r} + v\frac{\partial u}{\partial \phi'} + w\frac{\partial u}{\partial z} - \frac{v^2}{r} - 2\Omega v - \Omega^2 r\right]\\ &= -\frac{\partial p}{\partial r} + \mu\left(\frac{\partial^2 u}{\partial r^2} + \frac{1}{r}\frac{\partial u}{\partial r} - \frac{u}{r^2} + \frac{1}{r^2}\frac{\partial^2 u}{\partial \phi'^2} + \frac{\partial^2 u}{\partial z^2} - \frac{2}{r^2}\frac{\partial v}{\partial \phi}\right) + F_r\end{aligned} \tag{2.12}$$

$$\begin{aligned}&\rho\left[\frac{\partial v}{\partial t} + u\frac{\partial v}{\partial r} + \frac{uv}{r} + \frac{v}{r}\frac{\partial v}{\partial \phi'} + w\frac{\partial v}{\partial z} + 2\Omega u\right]\\ &= -\frac{1}{r}\frac{\partial p}{\partial \phi'} + \mu\left(\frac{\partial^2 v}{\partial r^2} + \frac{1}{r}\frac{\partial v}{\partial r} - \frac{v}{r^2} + \frac{1}{r^2}\frac{\partial^2 v}{\partial \phi'^2} + \frac{\partial^2 v}{\partial z^2} + \frac{2}{r^2}\frac{\partial u}{\partial \phi'}\right) + F_\phi\end{aligned} \tag{2.13}$$

$$\rho\left[\frac{\partial w}{\partial t}+u\frac{\partial w}{\partial r}+\frac{v}{r}\frac{\partial w}{\partial \phi'}+w\frac{\partial w}{\partial z}\right] = -\frac{\partial p}{\partial z}+\mu\left[\frac{\partial^2 w}{\partial r^2}+\frac{1}{r}\frac{\partial w}{\partial r}+\frac{1}{r^2}\frac{\partial^2 w}{\partial \phi'^2}+\frac{\partial^2 w}{\partial z^2}\right]+F_z \tag{2.14}$$

The terms $2\Omega v$ and $2\Omega u$ of equations (2.12) and (2.13) represent the Coriolis acceleration components, while $\Omega^2 r$ is the centrifugal acceleration. These additional terms represent the main source of difference in the behaviour of rotating flows when compared to non-rotating flows.

In rotating environments, it is convenient to combine the static pressure gradient with the centrifugal acceleration to take into account of the distribution of pressure due to the centrifugal forces. The resulting distribution is the equivalent of the hydrostatic pressure in the gravitational field. The centrifugal term $\Omega^2 r$ of equation (2.12) can be included in the pressure gradient:

$$\tilde{p} = p - \frac{1}{2}\rho\Omega^2 r^2 \tag{2.15}$$

where $\tilde{p}$ is the reduced pressure and which can substitute the static pressure in equations (2.12)-(2.14).

From dimensional analysis of equation (2.10), two non-dimensional groups emerge: the Rossby number Ro and the Ekman number Ek, respectively defined as:

$$\mathrm{Ro} = \frac{U_0}{\Omega L} \tag{2.16}$$

$$\mathrm{Ek} = \frac{\nu}{\Omega L^2} \tag{2.17}$$

The Rossby number is a measure of the inertial forces with respect to the Coriolis terms, while the Ekman number is a measure of the viscous forces with respect to the Coriolis forces. The length scale L and the reference velocity U_0 have to be chosen according to the specific problem. Flows where the Coriolis terms are dominant relative to others, i.e. Ro $\ll 1$ and Ek $\ll 1$, are called geostrophic. In a geostrophic flow, the Coriolis forces are balanced by the pressure gradients.

2.2.2 Taylor-Proudman theorem

The Taylor-Proudman theorem states that in a steady and incompressible geostrophic flow the three components of the relative velocity do not change in the axial direction. In a system with solid walls such as a compressor cavity, the flow in the core is thus two-dimensional in planes perpendicular to the axial direction:

$$\frac{\partial \boldsymbol{w}}{\partial z} = 0 \tag{2.18}$$

2.2.3 Linear Ekman layer equations

Consider the following assumptions:

- steady flow $\left(\frac{\partial}{\partial t} = 0\right)$;
- axisymmetric flow $\left(\frac{\partial}{\partial \phi'} = 0\right)$;
- laminar flow;
- no body forces $\left(F_r = F_{\phi'} = F_z = 0\right)$;
- Ro $\ll 1$, meaning that the convective terms can be neglected.

Under these conditions, equations (2.12)-(2.14) reduce to:

$$-2\rho\Omega v = -\frac{\partial \tilde{p}}{\partial r} + \mu \frac{\partial}{\partial r}\left[\frac{1}{r}\frac{\partial}{\partial r}(ru)\right] + \mu \frac{\partial^2 u}{\partial z^2} \tag{2.19}$$

$$2\rho\Omega u = \mu \frac{\partial}{\partial r}\left[\frac{1}{r}\frac{\partial}{\partial r}(rv)\right] + \mu \frac{\partial^2 v}{\partial z^2} \tag{2.20}$$

$$0 = -\frac{\partial \tilde{p}}{\partial z} + \mu \frac{\partial}{\partial r}\left[\frac{1}{r}\frac{\partial}{\partial r}(rw)\right] + \mu \frac{\partial^2 w}{\partial z^2} \tag{2.21}$$

while equation (2.8) reduces to:

$$\frac{1}{r}\frac{\partial}{\partial r}(ru) + \frac{\partial w}{\partial z} = 0 \tag{2.22}$$

Considering a rotating cavity whose axis is aligned with z such that the surface of one of the disks is at $z = 0$, the flow in the core of the cavity will be in geostrophic equilibrium (the core is assumed inviscid):

$$2\rho\Omega v_c = \frac{\partial \tilde{p}}{\partial r} \tag{2.23}$$

$$2\rho\Omega u_c = 0 \tag{2.24}$$

$$0 = \frac{\partial \tilde{p}}{\partial z} \tag{2.25}$$

Note that the subscript c refers to values in the cavity core. As discussed above, the boundary layers on the disks are commonly referred to as Ekman layers. If in the boundary layer the rate of change of the velocities along the direction normal to the solid walls is much higher than the rate of change along the radial direction, equations (2.19)-(2.21) can be linearized:

$$-2\rho\Omega v = -\frac{\partial \tilde{p}}{\partial r} + \mu \frac{\partial^2 u}{\partial z^2} \tag{2.26}$$

$$2\rho\Omega u = \mu\frac{\partial^2 v}{\partial z^2} \tag{2.27}$$

$$0 = -\frac{\partial \tilde{p}}{\partial z} + \mu\frac{\partial^2 w}{\partial z^2} \tag{2.28}$$

and the continuity equation yields:

$$\frac{\partial w}{\partial z} = 0 \tag{2.29}$$

If the value of w in a single location is known, the velocity component in the boundary layer is known. At the solid wall, it must be $w = 0$ for the no-slip condition. From the Taylor-Proudman theorem, $w = 0$ in the cavity core as well. Equation (2.28) simplifies to:

$$\frac{\partial \tilde{p}}{\partial z} = 0 \tag{2.30}$$

Combining equation (2.23) and (2.26) and re-writing equation (2.27), the linear Ekman layer equations are found:

$$-2\rho\Omega(v - v_c) = \mu\frac{\partial^2 u}{\partial z^2} \tag{2.31}$$

$$2\rho\Omega u = \mu\frac{\partial^2 v}{\partial z^2} \tag{2.32}$$

The Ekman layer is non-entraining, thus the thickness is constant. The solution of equations (2.31)-(2.32) with proper boundary conditions (no-slip at the wall and velocity equal to freestream at the outer edge of the layer) leads to the tangential and radial velocity profiles illustrated in Figure 2.3. If the flow in the cavity rotates faster than the disks, the radial component is inward, the opposite if its rotation speed is lower. The angle ϑ that the resulting velocity vector makes with respect to the tangential direction varies with the distance from the wall. Projecting the velocity distribution on a plane results in the so-called Ekman spiral.

2.3 TYPES OF ROTATING CAVITIES

A variety of different configurations of rotating cavities in turbomachinery are summarised in Figure 2.4. They can be closed or open with possible access or not to the rotation axis. There can be flow, either radial (inward/outward) or axial. There can be a central shaft, which rotates at its own speed in the same or opposite sense with respect to the cavity. There can be multiple cavities, with one disk shared between two. The metal surfaces might have the same temperature of the flow (isothermal cavity) or different.

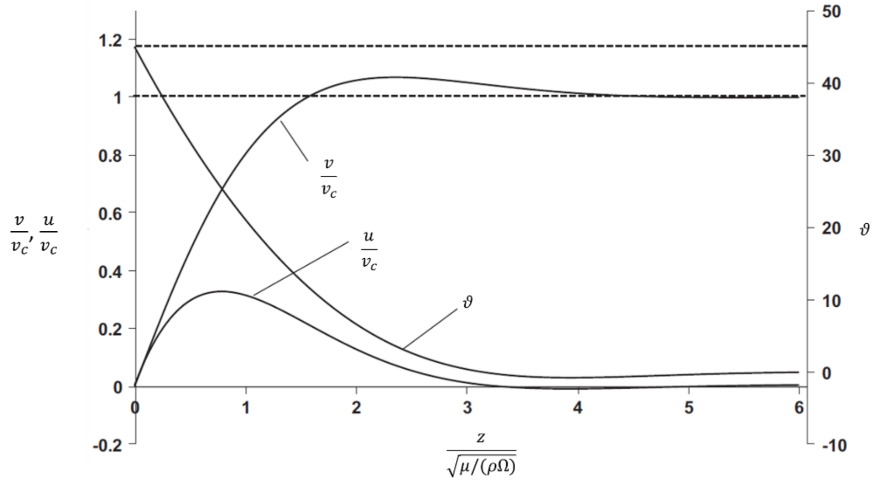

Figure 2.3 – Analytical solution of the linear Ekman layer equations (adapted from Sultanian 2018).

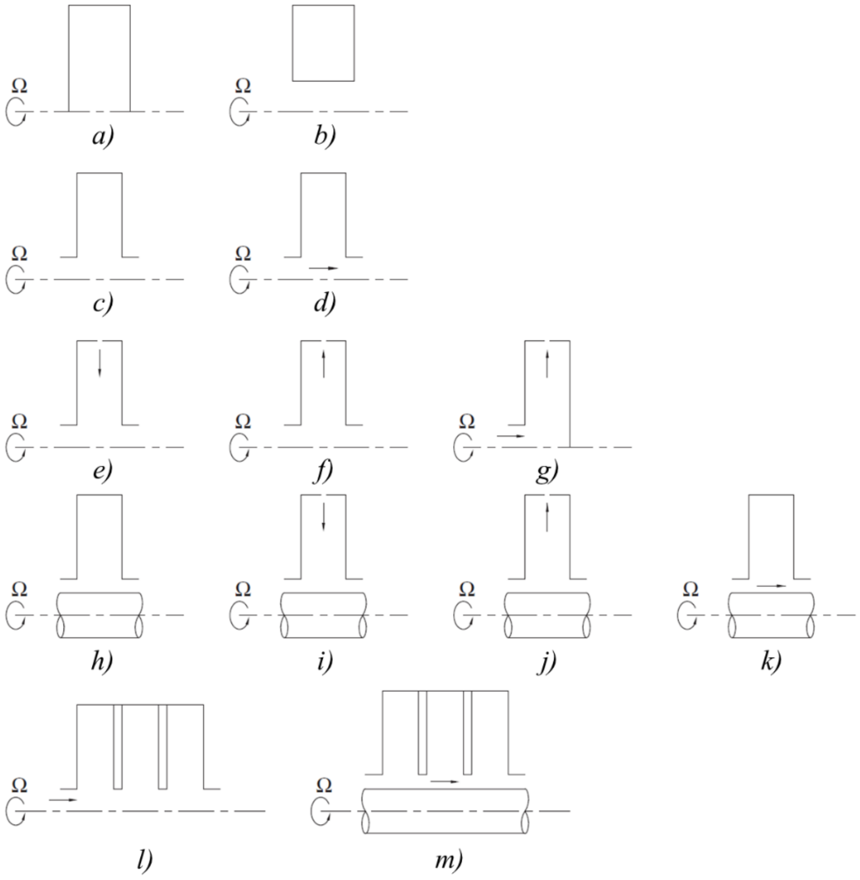

Figure 2.4 – Types of rotating cavities; a) closed cylindrical cavity; b) closed annular cavity; c) open cavity; d) open cavity with axial through-flow; e) open cavity with radial inflow; f) open cavity with radial outflow; g) open cavity with axial inlet and radial outflow; h) open cavity with shaft; i) open cavity with shaft and radial inflow; j) open cavity with shaft and radial outflow; k) open cavity with shaft and axial through-flow; l) multi-cavity with axial through-flow; m) multi-cavity with shaft and axial through-flow; (adapted from Childs 2011).

With reference to a single cavity, the following quantities and symbols will be used in the present work (Figure 2.5):

- a is the inner radius

- a' is the inner radius of the disk diaphragm
- b is the shroud radius
- b' is the outer radius of the disk diaphragm
- r_s is the shaft radius
- s is the axial gap of the cavity (taken at a)
- s' is the cavity axial length (for disks with cobs thicker than diaphragms)
- t_d is the disk thickness
- $G = s/b$ is the gap ratio
- l is the axial length of the disk cob (generally higher than the disk thickness)

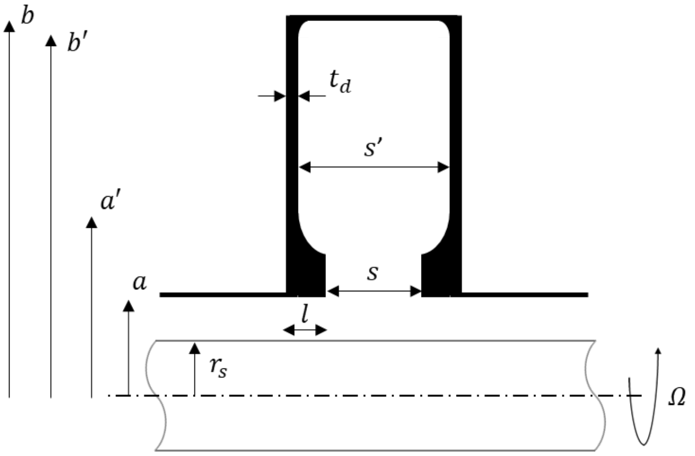

Figure 2.5 – Scheme of a single cavity and related nomenclature.

The three most common cavity configurations for HPCs are presented below to provide an overview on the flow field in the relevant cases. The relevant non-dimensional parameters for heated rotating cavities are then reported.

2.3.1 Closed rotating cavity

A closed rotating cavity is rather common in axial compressors of industrial gas turbines and sometimes present in axial compressors of aero engines. They can be cylindrical or annular, as shown in Figure 2.4a and Figure 2.4b. If the cavity is isothermal, the flow in the core will be in solid-body rotation at steady state.

If one disk is hotter than the other, natural convection can occur. In the rotating reference frame, vortices are generated by movement of air from the hot disk to the cold disk at the lower radii and vice versa at the higher radii (Figure 2.6a). In the case where the shroud is heated, the flow field is affected by buoyancy. The air close to the shroud heats up and give rise to cyclonic and anticyclonic vortex pairs whose axes are aligned to the cavity (Figure 2.6b). The mechanism is allowed by the centrifugal force, which acts onto the shroud in the same manner as gravity would act on a horizontal heated plate. The associated convection is generally referred to as Rayleigh-Bénard convection, and is typical in all the rotating cavities heated at the shroud.

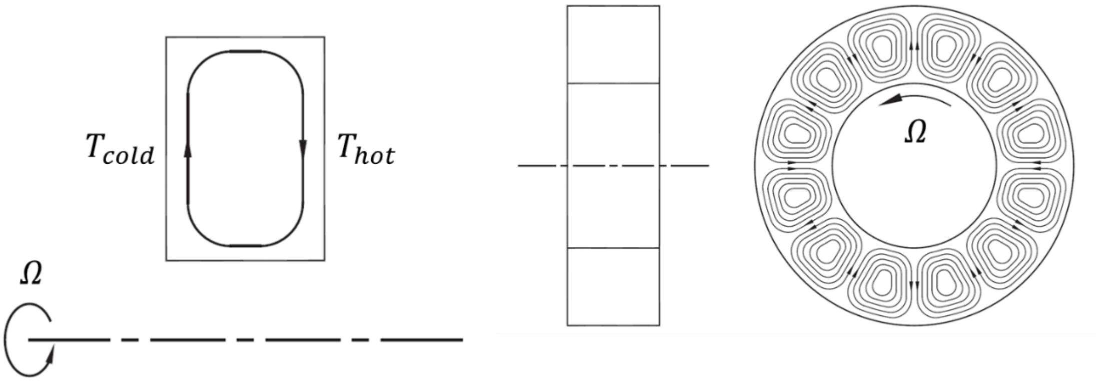

a) b)

Figure 2.6 – Flow features of heated closed cavities; a) one disk hotter than the other; b) heated shroud; (adapted from Childs 2011).

2.3.2 Rotating cavity with radial inflow

A rotating cavity with radial inflow such as those in Figure 2.4e and Figure 2.4i can be included in the design of a high-pressure compressor in the middle of the disk stack to bleed high-pressure air for cooling or other purposes. Holes or slots are machined on the shroud, creating a flow source for the cavity. Close to the discharge in the cavity there are recirculation zones. The cavity core flow is geostrophic, with no entrainment of air from the core to the Ekman layers. The radial inflow feeds the layers from the outer radius, while at the inner radius the conservation of mass requires the presence of a sink region. This behaviour is counterintuitive as it is opposite to what is expected from a free disk pumping effect.

2.3.3 Rotating cavity with axial though-flow

Rotating cavities with axial though-flow are the primary objective of the present work. They characterise the large majority of high-pressure compressors for aero engines, where they are stacked one after the other (Figure 2.4m). In steady-state operation, the shroud is heated by the compressed air in the main stream. For each cavity, the following disk – with respect to the annulus flow direction – is hotter due to the ongoing adiabatic compression process. The axial though-flow is obtained by an upstream bleed in the compressor.

For the isothermal case, the axial through-flow is expected to generate a toroidal vortex at the low radii of the cavity. The cavity core is in geostrophic conditions. As detailed in the next section, vortex breakdown is possible, cancelling the axisymmetry of the flow. When the shroud is heated, vortex pairs such as those in Figure 2.6b occur. However, the through-flow interacts with the core flow, and a portion can breach into the core, giving rise to the so-called “radial arms”. To conserve of mass, a radial inflow in the Ekman layers is generated. A visual representation of the flow features is given in Figure 2.7.

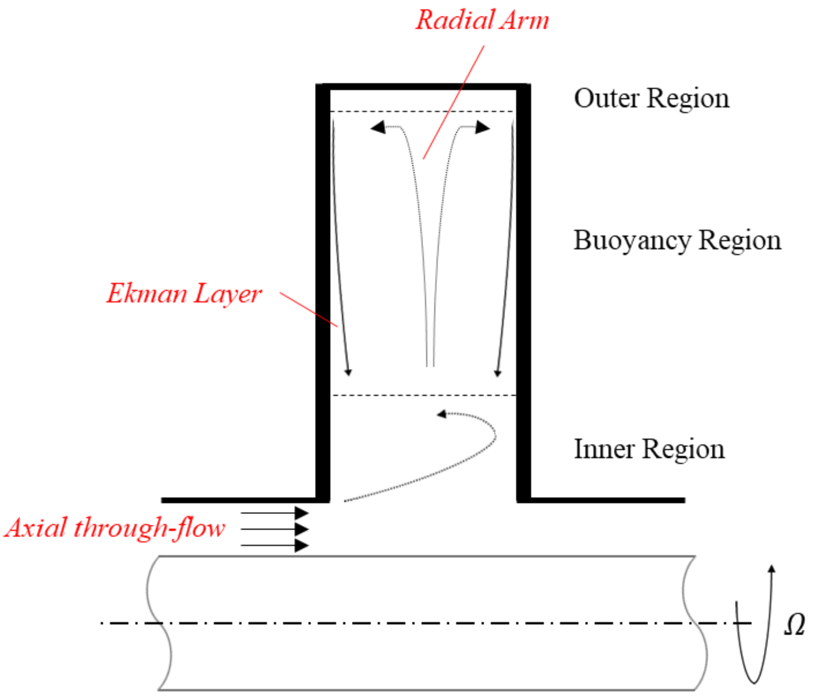

Figure 2.7 – Flow features of a heated rotating cavity with axial through-flow of coolant. Interaction between the through-flow and the cavity flow is constrained in the inner region; the buoyancy region hosts vortex pairs and radial arms; the outer region is a convective region between cavity flow and shroud.

2.3.4 Non-dimensional parameters for rotating cavities

With reference to the physics of rotating cavities with axial though-flow, the following non-dimensional parameters are relevant.

The rotational Reynolds number Re_ϕ represents the magnitude of the inertial versus the viscous terms in a rotating flow problem, where the outer radius of the cavity is taken as length scale:

$$\mathrm{Re}_\phi = \frac{\rho \Omega b^2}{\mu} \tag{2.33}$$

An axial Reynolds number Re_z can be defined for the axial though-flow case:

$$\mathrm{Re}_z = \frac{\rho W d_h}{\mu} \tag{2.34}$$

where W represents the axial component of through-flow velocity in the fixed reference frame and d_h is the hydraulic diameter of the annular passage, $d_h = 2(a - r_s)$.

As mentioned previously, the Rossby number represents the ratio between the inertial and Coriolis terms. The axial velocity W of the through-flow can be used as reference:

$$\mathrm{Ro} = \frac{W}{\Omega a} \tag{2.35}$$

Hence,

$$\mathrm{Ro} \propto \frac{\mathrm{Re}_z}{\mathrm{Re}_\phi} \tag{2.36}$$

Heated cavities such as those in axial compressors are subject to buoyancy phenomena triggered by heating of the flow and a consequent density non-uniformity. The resulting heat transfer mode is natural convection, which is commonly described by the Grashof number. The traditional formulation is rearranged by substituting the gravitational acceleration with the centripetal:

$$\mathrm{Gr} = \frac{\rho^2 \beta \Delta T \Omega^2 b^4}{\mu} \tag{2.37}$$

where β is the volumetric expansion coefficient and

$$\beta \Delta T = \frac{T_{0,b} - T_f}{T_f} \tag{2.38}$$

is a non-dimensional term called buoyancy parameter. $T_{0,b}$ corresponds to the metal temperature at the shroud radius, while T_f is the through-flow temperature. It is easy to show that:

$$\mathrm{Gr} = \mathrm{Re}_\phi^2 \beta \Delta T \tag{2.39}$$

It is possible to define a non-dimensional group from the ratio between Gr and Re_z^2, i.e. the natural versus the forced convection:

$$\mathrm{Bo} = \frac{\mathrm{Gr}}{\mathrm{Re}_z^2} \propto \frac{\beta \Delta T}{\mathrm{Ro}^2} \tag{2.40}$$

where Bo is called buoyancy number.

2.4 REVIEW OF EXPERIMNTAL RESEARCH ON COMPRESSOR CAVITIES WITH AXIAL THROUGH-FLOW

A detailed review of the experimental research on the topic is reported to assess the characteristics and capabilities of experimental rigs for compressor cavities and to support the flow features discussed so far. A comprehensive review of buoyancy-induced flows in open rotating cavities is reported in Owen and Long 2015. The early rigs were far from the operating conditions of modern engines, but nonetheless contributed to the fundamental understanding. The level of sophistication reached by the most recent rigs is believed to be enough representative. For the sake of comparison, all the experimental conditions reported in the analysed literature have been converted in non-dimensional terms according to the definitions given in the section before.

2.4.1 Early work

The first experimental investigations on rotating cavities aimed at the general understanding of the flow behaviour, trying eventually to relate it to the heat transfer rate. Flow visualization in a single non-heated cavity rig was made by Owen and Bilimoria 1977, showing that, without rotation, the axial through-flow generates a toroidal vortex filling the whole cavity. With rotation, the penetration decreased with Re_{ϕ} and increased with Re_{z}. Two breakdown modes were isolated: “spiral” in the range $21 < \mathrm{Ro} < 100$, axisymmetric (with oscillating boundaries) in the range $0.8 < \mathrm{Ro} < 21$. Their presence was also related with the gap ratio G. When the cavity was heated, the breakdown was responsible for a dramatic change in the Nusselt number. Moreover, on a different geometry, changing the inlet swirl angle does not affect the breakdown (Owen and Pincombe 1979). Both these rigs featured no shaft. In real engine conditions, a $\mathrm{Ro} > 0.5$ was always found to trigger instabilities in the through-flow (Johnson et al. 2006).

The non-heated behaviour of the cavity flow in an internal air system facility featuring a compressor drum with four cavities and pressure taps on the disk surfaces was investigated in Johnson et al. 1991. It was concluded that, at engine representative Ro and with coolant injected at the shaft radius, the flow inside the cavities is essentially in solid body rotation. If the shroud was heated, the corresponding heat transfer type would thus be free convection.

2.4.2 Early University of Sussex rigs

A number of geometries with different gap ratios and Rossby numbers were investigated by Farthing et al. 1992a. This was achieved via four single-cavity rigs. In isothermal conditions, a small gap ratio ($G < 0.267$) limits the influence of vortex breakdown on the cavity flow. With $\mathrm{Ro} < 20$, most of the fluid in the cavity experiences solid body rotation. In the case of symmetrically heated disks, flow visualization showed a radial arm of through-flow precessing about the axis and splitting in two vortices (cyclonic and anti-cyclonic). Additionally, it was possible to notice a radial inflow near the disk surfaces (inside the Ekman layers). The great flexibility of their rig in terms of different geometries and optical access limited the Grashof number to Gr = 9×10^9. Temperature measurements were obtained by embedding thermocouples onto the rotating disks with signals taken out through slip rings. In one of these rigs (Farthing et al. 1992b), for a disk temperature increasing radially, the local disk Nusselt number had the same increasing trend, no consistent correlation with the Rossby number was found. The ranges of experimental conditions were: $2\times10^5 < \mathrm{Re}_\phi < 5\times10^6$, $2\times10^4 < \mathrm{Re}_z < 1.6\times10^5$, $0.25 < \beta\Delta T < 0.3$. With only one disk heated (similar to engines, where the shroud temperature increases along the axis), the magnitude of radiation from the hotter to the colder disk can be as high as the convection. Moreover, no influence of the shaft on the heat transfer coefficients was detected.

2.4.3 MTU Aero Engines rig

The influence of the shaft was studied further by Burkhardt et al. 1993 for a three cavities compressor rotor rig for Gr up to 4.4×10^{12}. Hot air heated the outer shroud of the drum while the shaft speed and direction could be controlled separately. The cooling air could be pressurized up to 2.76 bar. It was shown that as the shaft approaches the drum speed, the disk temperature decreased. This rig was the first to replicate engine transient conditions, but only four temperature signals for each disk were recorded for the cavity of interest. The measured temperatures were interpolated with a polynomial to get a surface temperature distribution, then a 2D solver used to compute the temperature field of the disks. The heat flux was calculated via the temperature gradient normal to the cavity walls, and used to determine the Nusselt number. The computed Nusselt numbers showed a “peaky” behaviour and was, in general, higher for the upstream disk.

2.4.4 RWTH Aachen rig and Bath early rig

Starting from the flow structure in Farthing et al. 1992a, the repeatability of the results at different cases by means of flow visualization was confirmed by Bohn et al. 2000 (G = 0.2, a/b = 0.3, Gr < 1.7×10^{11}, Re_ϕ < 8×10^5). A single cavity rig with a co-rotating shaft was equipped with heaters on the disks and the shroud. A section of one disk was fitted with a transparent window. The Nusselt numbers showed a positive correlation with Re_z. Further investigations (Owen and Powell 2004) confirmed that the disk Nusselt number increases with increasing Re_ϕ: buoyancy effects become stronger

(Re_ϕ = 0.38-3.2×10^6, Re_z = 0.15-4.7×10^4, shroud temperature up to 100 °C). In their single cavity rig, one disk was heated uniformly, and the other was fitted with a transparent window to allow LDV measurements. The spectral analysis of the velocity results revealed that the cavity structures could be composed by one, two or three vortex pairs. This was consistent with the thermodynamic analysis performed by Owen 2010.

2.4.5 Multi-Cavity rig at the University of Sussex

In more recent years, the Multi-Cavity Rig at the University of Sussex contributed to the understanding of both the flow structure and the heat transfer in the cavity, as well as the effects of the disk geometry. The original build comprised two cavities and a cone (Alexiou 2000), and was fully instrumented with thermocouples peened onto the metal surfaces. The cables were held in channels through epoxy resin and titanium straps were spot-welded to secure the bundles. Impinging hot air was used to heat up the shroud, while the through-flow of cooling air could be pressurized (to increase the rig performance in terms or Re_z, Re_ϕ and Gr acting on the density), and the shaft could be rotated. It was shown that the heat transfer on the metal surfaces depends not only on Re_ϕ and Re_z, but also on the gap ratio, inlet radius, shaft radius and shaft rotation.

In the second build of the same rig, the number of cavities was increased to five and included optical access for LDV (Long et al. 2007). It was demonstrated that the tangential velocity in the cavity core did not feature axial changes and the axial velocity is nearly zero. In the cob region, the flow swirled faster than the walls for a wide gap and slower than the walls for a narrow gap. In both cases, eventually, the tangential velocity tended to the solid body as the radius increases. A smaller gap, therefore, attenuated the interactions between the cavity and the through-flow. The presence of radial velocity in the cavity was found: even though tiny in magnitude compared to the tangential component, it proved the existence of radial inflow.

The third build of the rig featured four cavities with both sides of the middle disk being instrumented similarly to Alexiou 2000. Through LDV, Miché 2008 found evidence of periodic fluctuations in the tangential velocity of the flow in the cavity, linked via spectral analysis to the presence of contra-rotating vortex pairs. The effects of the relevant non-dimensional parameters on the disk temperature distribution were investigated by Atkins and Kanjirakkad 2014. In this work, the rig was rebuilt and instrumentation completely changed. It was the first rig with low uncertainty, telemetry-based thermocouple measurements with high enough spatial density to enable the stable

Bayesian heat flux reconstruction (Section 2.5.4). The investigated non-dimensional ranges were: $0.3 < \mathrm{Ro} < 4.7$, $0.06 < \beta\Delta T < 0.32$, $5.4\times10^{8} < \mathrm{Gr} < 2.9\times10^{12}$. When the buoyancy forces are high (high Re_{ϕ} and $\beta\Delta T$), the instabilities promote radial mixing and prevent the rise of the non-dimensional temperature at higher radii. The cob region was found to be influenced by Re_{z} mainly, and only slightly by the Grashof number. The rotationally dominated flow in the upper part of the cavity suppresses interactions with the through-flow. With lower Re_{ϕ} the higher mixing pushed up the non dimensional temperature in the cobs. Following the work of Farthing et al. 1991 – where de-swirl nozzles at the cavity shroud had been suggested to inject flow oppositely to the solid body rotation (to break the free convection and enhance the mixing) – the Multi-Cavity Rig was used to show how a radial inflow bleed from the annulus air can stop the buoyant flow and potentially reduce the engine transients during acceleration and deceleration (Atkins 2013). It was the first rig in literature to use transients to estimate the true local heat transfer coefficients at engine scaled heating and cooling conditions. This approach to the heat transfer problem allows the calculation of the local heat transfer coefficient without the need of measuring temperatures and the need to solve an inverse problem.

2.4.6 TU Dresden rig

The presence of two convection zones – one influenced by the buoyant structures, the other by the axial through-flow – was found also by Günther et al. 2012 and Günther et al. 2014 ($\mathrm{Re}_{\phi} < 9.3\times10^{6}$, $\mathrm{Re}_{z} < 1.2\times10^{5}$, $\mathrm{Gr} < 2.25\times10^{13}$). They used a two-cavity rig with a uniformly heated external shroud. The surfaces of both cavities were instrumented with thermocouples and the temperature at the cavity inlets was also captured. The reported heat flux measurements were derived from the axial temperature gradient in the internal disk. Both cavities have a radial location where the heat flux becomes zero (at higher radius in the first cavity due to stronger impingement of the through-flow). This was explained with the extension of a toroidal vortex compared to the buoyancy-dominated region: when the two zones meet, the heat flux cancels. The flow in the first cavity always cools the disk, whereas the flow in the second cavity cools it only in the impingement-dominated region. No correlation was established between the location where the heat flux changes sign and the Rossby number. The toroidal vortex of coolant grew with Re_{z} only at low Re_{ϕ}.

2.4.7 Beihang University rig

A two cavity rig was used to characterize the heat transfer in the ranges: $0.2 < Ro < 1.6$, $0.16 < \beta \Delta T < 0.3$, $4.7 \times 10^{10} < Gr < 9.8 \times 10^{11}$ (Quan et al. 2018). The heat transfer coefficient distributions were obtained through specific sensors developed in-house. The measurements indicated the presence of a region affected by forced convection and a region affected by free convection. Once again, the axial through-flow affects mainly the cob region, and especially the windward surface. The rotation and the buoyancy parameter affect the heat transfer mainly at higher radii. Peaks of heat transfer coefficients were found at low radii.

2.4.8 New TU Dresden rig

A recent single cavity rig reported in Diemel et al. 2019 aims to measure the cavity surface temperature, surface pressure, core temperature and inlet swirl angle at a very wide range of non-dimensional parameters: high rotational speed ($Re_{\phi} = 1.4 \times 10^7$, while a specifically designed shroud heating module pushes $\beta \Delta T$ up to 0.5, resulting in a $Gr > 10^{14}$. Since both disks are instrumented with thermocouples placed also on the back faces, they plan to perform a finite element analysis using interpolated temperatures to extract the heat fluxes and therefore the heat transfer coefficients. To the author’s knowledge, this is the test rig with the highest potential for performance but no results have been published yet.

2.4.9 Summary

The Grashof number and the buoyancy parameter are the two fundamental indicators characterising buoyancy-induced flow in heated rotating cavities with axial through-flow of coolant. The experimental test rigs can be ranked accordingly, as shown in Figure 2.8. It is believed that real engines cavities do not differ much from these values. The test rig described in this thesis, named the Bath Compressor-Cavity Rig, is also reported in Luberti et al. 2021.

2.5 OWEN AND TANG BUOYANCY MODEL AND VALIDATION

Besides the unravelling of the complex physics behind compressor cavities, the engine designer needs a reliable predictive model to calculate the correct temperature distribution on the metal walls for given specific boundary conditions. Experimentally validated equations for the Nusselt number distributions on each surface of the cavity are the key deliverable of theoretical studies. An overview of models of the heat transfer associated with cavities with axial through flows is reported in Owen et al. 2018. A crucial milestone was represented by the Buoyancy Model proposed by Owen and Tang 2015. This section starts recalling the basics of heat transfer in forced and free convection and then aims to provide an overview of the fundamental insight of the model starting from the equations previously derived. The current validation status follows.

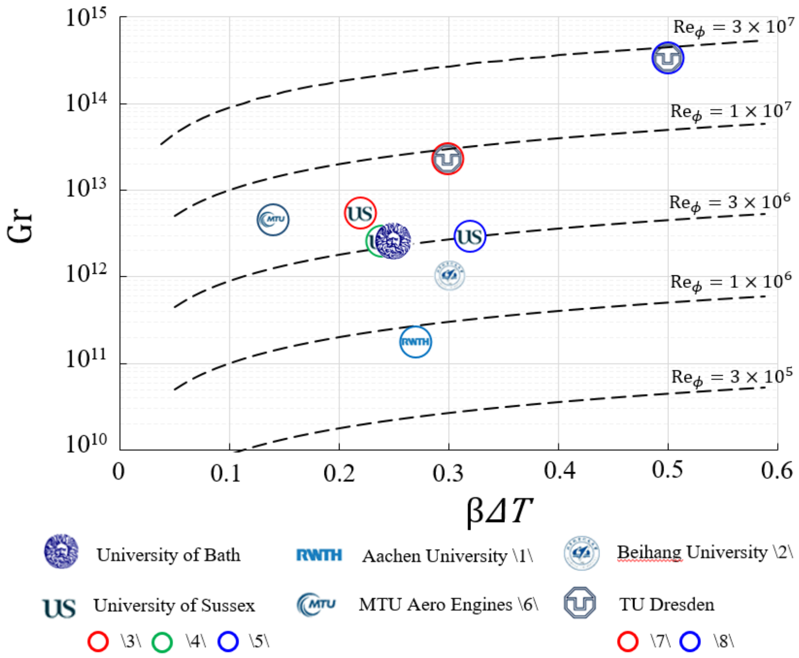

Figure 2.8 – Experimental research rigs for heated rotating cavities with axial through-flow (adapted from Luberti et al. 2021). References in the Figure: \1\ Bohn et al. 2000; \2\ Quan et al. 2018; \3\ Alexiou 2000; \4\ Long et al. 2007, Long and Childs 2007; \5\ Miché 2008, Atkins and Kanjirakkad 2014; \6\ Burkhardt et al. 1993; \7\ Günther et al 2012, Günther et al. 2014; \8\ Diemel et al. 2019.

2.5.1 Basic review of heat transfer in forced and free convection

In the case of a fluid stream over an isothermal surface with L as length scale, a thermal boundary layer develops if the temperature of the fluid is different form the surface (Figure 2.9). At the surface, the local heat flux can be expressed as:

$$q_o = -k \left.\frac{\partial T}{\partial z}\right|_{z=0} \tag{2.41}$$

Newton's law of cooling states:

$$q_o = h(T_o - T_\infty) \tag{2.42}$$

Hence:

$$h = \frac{-k \partial T / \partial z|_{z=0}}{T_o - T_\infty} \tag{2.43}$$

The conditions of the thermal boundary layer affect the surface temperature gradient and therefore the rate of heat transfer across the boundary. Additionally, the temperature gradient in the boundary layer decrease as $\tilde{x}$ increases, thus the heat transfer coefficient and the heat flux decrease as $\tilde{x}$ increases.

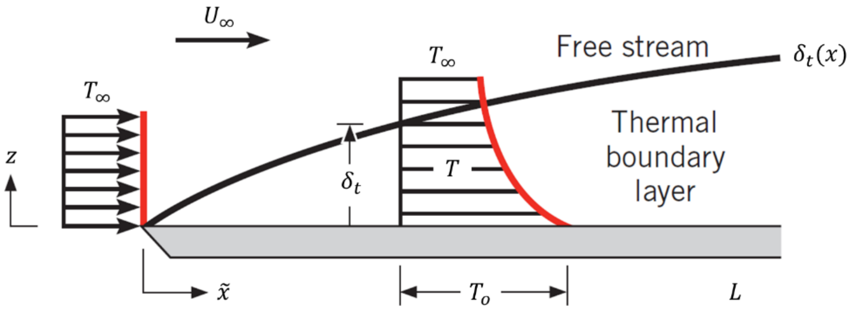

Figure 2.9 – Thermal boundary layer development on an isothermal flat plate (adapted from Incropera et al. 2011).

Using dimensionless variables, equation 2.43 becomes:

$$h = \frac{k}{L}\frac{\partial T^*}{\partial z^*}\bigg|_{z^*=0} \tag{2.44}$$

where:

$$T^* = \frac{T - T_o}{T_\infty - T_o} \tag{2.45}$$

$$z^* = \frac{z}{L} \tag{2.46}$$

Equation (2.44) introduces the Nusselt number as a non-dimensional parameter equal to the dimensionless temperature gradient at the surface:

$$\mathrm{Nu}_L = \frac{hL}{k} = \frac{\partial T^*}{\partial z^*}\bigg|_{z^*=0} \tag{2.47}$$

The Nusselt number represents a measure of the convection heat transfer on a surface with a fluid stream.

The heat transfer mechanism reported in Figure 2.9 represents the forced convection, i.e. a condition in which the relative motion of the flow with respect to the surface is maintained by external means. In forced convection the local Nusselt number is a universal function of the abscissa $\tilde{x}$ of the geometry, of the Reynolds number Re_L and of the Prandtl number Pr:

$$\mathrm{Nu}_L = f(\tilde{x}, \mathrm{Re}_L, \mathrm{Pr}) \tag{2.48}$$

$$\mathrm{Re}_L = \frac{\mu U_\infty L}{\rho} \tag{2.49}$$

$$Pr = \frac{c_p \mu}{k} \tag{2.50}$$

To express the average heat transfer coefficient over a surface, the Nusselt number can be averaged, resulting in a dimensionless parameter depending only upon the Reynolds number and the Prandtl number:

$$\mathrm{Nu}_L = f(\mathrm{Re}_L, \mathrm{Pr}) \tag{2.51}$$

For a given fluid with averaged physical properties, the dependency of the Nusselt number on the Prandtl number can be relaxed (as it would be treated as a constant). In such conditions, for forced convection the Nusselt number – and thus the heat transfer coefficient on a surface – would depend only on the Reynolds number.

In the case of absence of a forced velocity, convection mechanisms can still occur. These cases are generally referred to as natural or free convection. A body force, such as gravity or centrifugal forces (as in compressor cavities), together with a density gradient, creates a buoyancy force responsible for convection. A temperature difference between a surface and a fluid can be considered the driver for free convection heat transfer, if the temperature difference generates for density gradients in the fluid. In Figure 2.10, an isothermal cylinder with D as length scale is immersed in quiescent air a temperature of T_∞.The heating of the fluid in the vicinity of the cylinder and the gravity generate a buoyant plume of flow upwards. As the previous case, a thermal boundary layer develops around the cylinder. At low ϕ, the boundary layer thickness is low, resulting in high heat transfer rate as per equation (2.43). Once again, the heat transfer rate decreases as ϕ increases.

As for the forced convection, it is possible to derive the average Nusselt number over a surface as a universal function of the Grashof number Gr_D, and of the Prandtl number Pr:

$$\mathrm{Nu}_D = f(\mathrm{Gr}_D, \mathrm{Pr}) \tag{2.52}$$

$$\mathrm{Gr}_D = \frac{\mu\beta(T_o - T_\infty)D^3}{\rho} \tag{2.53}$$

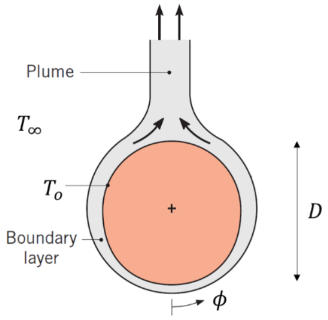

Figure 2.10 – Thermal boundary layer on a heated horizontal cylinder (from Incropera et al. 2011).

Free convection velocities are generally much smaller than forced convection velocities (since in free convection the convective velocities are generated by temperature differences). This implies that the associated heat transfer rates are lower. In the large majority of applications, forced and free convection theoretically coexist. If the effect of the Reynolds number is much higher than the effect of the Grashof number, free convection can be discarded. Conversely, forced convection can be discarded. However, there is a number of cases where the two effects impact the heat transfer rate in the same magnitude and have to be considered together.

A more generalised definition of the heat transfer coefficient considers heat dissipation mechanisms occurring in a flow over a solid body (e.g. a flat plate as in Figure 2.9). For the no-slip condition, kinetic energy is converted to heat energy through the boundary layer. In high-speed flows, this heat energy is large, such that the kinetic energy which can be dissipated is high. Since the boundary layer is very hot, conduction from the layer to the freestream can occur, meaning that only a portion of the heat generated from the kinetic energy is recovered in the fluid at the solid surface. (If all the energy was recovered, the attained temperature would be the stagnation temperature.) The temperature reached from the recovered heat represents the recovery temperature (also known as adiabatic wall temperature). As recovery temperature T_{rec} is the temperature of the fluid against the wall, it actually drives the convection mechanism from the fluid to the wall:

$$h = \frac{-k\partial T/\partial z|_{z=0}}{T_o - T_{rec}} \tag{2.54}$$

Consequently, the Nusselt number can be related to this definition. It is worth noting that, in case $T_\infty < T_o < T_{rec}$, heat flows into the surface even though the surface is hotter than the freestream (Figure 2.11).

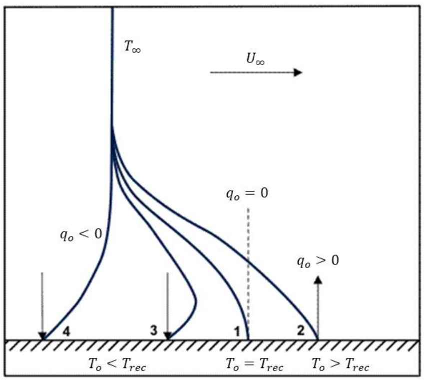

Figure 2.11 – Temperature profiles in a laminar boundary layer with viscous dissipation (adapted from Chapman 1984).

Considering a rotating cavity, in the relative frame (fluid in the cavity rotating with respect to the rotating disks) the rotation speed of the flow is close to that of the disks – a requirement for the presence of Ekman layers. This fact is documented in literature also experimentally: Bohn et al. 2000 observed a rotation of the vortex structures – and so of the cavity core – equal to 88-90% of the disk rotational speed. Assuming 8,000 rpm at a cavity outer radius of 0.24 m (dimensions consistent with the Bath Compressor-Cavity Rig, as reported in Chapter 5) and assuming a slip velocity of 15% between core flow and cavity walls, the relative peripheral velocity of the flow is around 30 m/s. The corresponding Mach number is less than 0.1, meaning that the stagnation conditions are the same as the static. Therefore, for the rotating cavity problem the recovery temperature coincides with the freestream temperature.

2.5.2 The Owen and Tang Buoyancy Model

Experimental evidence has shown that in rotating cavities with axial through-flow heated from the shroud the axisymmetry of the flow field is lost due to the occurrence of cyclonic/anticyclonic vortex pairs. There is also inflow on the disk surfaces. The main assumptions of the model are:

- the flow in the core is inviscid, compressible, three-dimensional and unsteady;
- the averaged flow in the Ekman layers is steady and axisymmetric, with the averaged radial mass flow rate constant along the radius;
- the compressibility of the core flow can be described by adiabatic transformations; the temperature is proportional to the rotation speed of the flow.

A simplified schematic of the cavity is reported in Figure 2.12. In the Buoyancy Model, radial positions are given normalised with respect to the cavity shroud ($x = r/b$), as in equation (2.1).

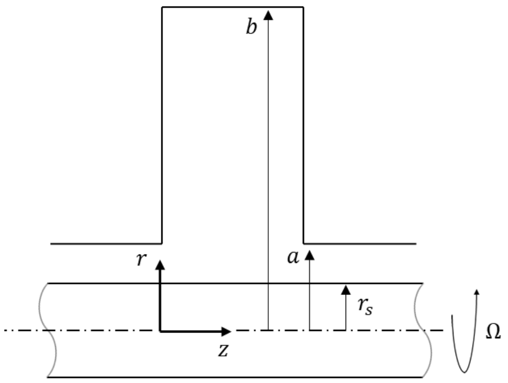

Figure 2.12 – Simplified schematic of the cavity used in the Owen and Tang Buoyancy Model.

Releasing the assumptions of axisymmetry and incompressibility from Section 2.2, equations (2.23)-(2.25) are:

$$2\rho_c\Omega\left(v_c+\frac{1}{2}\Omega r\right)=\frac{\partial p}{\partial r} \tag{2.55}$$

$$2\rho_c\Omega u_c=-\frac{1}{r}\frac{\partial p}{\partial\phi'} \tag{2.56}$$

$$\frac{\partial p}{\partial z}=0 \tag{2.57}$$

The cyclonic/anticyclonic vortex pairs in the cavity are responsible for generating the circumferential pressure gradients of equation (2.56), which are in equilibrium with the radial Coriolis acceleration. The continuity equation is shown as equation (2.6). Differentiating equation (2.55)-(2.57) along the z axis and retrieving the third term of the left hand side of equation (2.6) with the help of equations (2.55)-(2.57), the following is obtained:

$$\frac{\partial}{\partial z}[\rho w]=\frac{1}{2}\Omega\frac{\partial\rho}{\partial\phi'} \tag{2.58}$$

Since the flow is compressible and not axisymmetric, the assumptions of the Taylor-Proudman theorem are not respected: axial flow is theoretically possible. However, taking the circumferential average of equation (2.56), there cannot be a net axial mass flow rate in a symmetrically heated cavity, i.e. when the temperature distributions on the disks are the same. This results in a zero net entrainment in the Ekman layers on the disk surfaces. Considering circumferentially averaged velocities and applying the same procedure used in Section 2.2.3, the radial and momentum equations (2.55) and (2.56) become:

$$\Omega r^2\left[2\left(\frac{\rho_c v_c-\rho v}{\Omega r}\right)+(\rho_c-\rho)\right]=\frac{\partial\tau_r}{\partial z} \tag{2.59}$$

$$2\Omega(\rho u-\rho_c u_c)=\frac{\partial\tau_\phi}{\partial z} \tag{2.60}$$

The assumption of $u_c \ll u$ and the Boussinesq approximation $\rho=\rho_c(1-\beta\delta T)$ yield:

$$\rho_c\Omega r^2\left[\beta\delta T+2\frac{v_c-v}{\Omega r}\right]=\frac{\partial\tau_r}{\partial z} \tag{2.61}$$

$$2\Omega\rho u=\frac{\partial\tau_\phi}{\partial z} \tag{2.62}$$

Equations (2.61) and (2.62) are the linear Ekman layer equations valid for a symmetrically heated rotating cavity. The validity is limited to the rotating core region in case of axial-through-flow. The equations are used to calculate the velocity components in the Ekman layers, the thickness of the layer itself and the mass flow rate within. The averaged mass flow rate in the Ekman layers is assumed constant. All this information is necessary to retrieve the Nusselt number.

The Buoyancy Model considers the effects of the compressibility. Owing to the centrifugal acceleration, a radial pressure gradient builds up in the cavity, resulting in an adiabatic increase of temperature at higher radii, if the flow is assumed compressible. It is possible to relate the normalised density with the normalised radius:

$$\frac{\rho_c}{\rho_{c,a}} = \left[1 + \frac{\gamma - 1}{2}\mathrm{Ma}_c^2(x^2 - x_a^2)\right]^{\frac{1}{\gamma-1}} \tag{2.63}$$

with:

$$\mathrm{Ma}_c = \frac{\Omega_c b}{c_s} \tag{2.64}$$

$$c_s = \sqrt{\gamma R T_{c,a}} \tag{2.65}$$

At a given radius, the local heat transfer coefficient h_c can be expressed as:

$$h_c = \frac{q_o}{T_o - T_c} \tag{2.66}$$

The heat flux q_o is normal to the disk metal surface. The equation for the local Nusselt number according to the Buoyancy Model is:

$$\mathrm{Nu}_c = \frac{h_c r}{k} = \frac{1}{2}\frac{x_a^{1/2}}{I^{1/4}}\mathrm{Gr}_c^{1/4}\left[(\theta - \mathrm{Co})\left(\frac{\rho_c}{\rho_{c,b}}\right)^2 x^5\right]^{1/3} \tag{2.67}$$

with:

$$I = \int_{x_a}^{1} x^{11/3}\left[(\theta - \mathrm{Co})\left(\frac{\rho_c}{\rho_{c,b}}\right)^2\right]^{1/3} dx \tag{2.68}$$

$$\mathrm{Gr}_c = \mathrm{Re}_\phi^2 \beta (T_{o,b} - T_{c,b}) \tag{2.69}$$

$$\theta = \frac{T_o - T_c}{T_{o,b} - T_{c,b}} \tag{2.70}$$

$$\mathrm{Co} = 2\frac{|v_c|}{\Omega r}\frac{1}{\beta(T_{o,b} - T_{c,b})} \tag{2.71}$$

Gr_c is the local Grashof number calculated at the outer radius, Co is an empirical constant called the Coriolis parameter, which takes into account the difference in angular velocity between core and cavity, θ is the non-dimensional disk temperature.

To validate the Nusselt numbers provided by the Buoyancy Model, the core temperature distribution has to be determined. However, accurate values with high resolution are hard to achieve. For this reason, the heat transfer coefficient can be based on the through-flow:

$$h_f = \frac{q_o}{T_o - T_f} \tag{2.72}$$

A related non-invariant Nusselt number can be defined:

$$\mathrm{Nu}_f = \frac{h_f r}{k} \tag{2.73}$$

Combining equations (2.66) and (2.72), the ratio between the heat transfer coefficient based on the through-flow and that based on the local core temperature is:

$$\frac{h_f}{h_c} = \frac{T_o - T_c}{T_o - T_f} \tag{2.74}$$

The relation between the Nusselt number based on the through-flow and that based on the local core temperature follows:

$$\mathrm{Nu}_f = \frac{T_o - T_c}{T_o - T_f} \mathrm{Nu}_c \tag{2.75}$$

Nu_f is a non-dimensional parameter with a different meaning with respect to equation (2.47), as the reference temperature used is not the core temperature in the cavity but the through-flow temperature. This is because measuring the through-flow temperature is experimentally possible, while measuring the core temperature with a good spatial density is likely not feasible (or at least no attempt in such sense is reported in literature). The use of the through-flow temperature T_f as reference means that Nu_f is not invariant and will not necessarily scale from rig to rig. The relation between Nu_f (based on the through-flow temperature) and Nu_c, which is invariant, is reported in equation (2.75). As will be detailed in Chapter 5, The Bath Compressor-Cavity Rig is designed with the capability to host a few temperature measurements in the cavity core, which will be exploited in the future.

In the same fashion of Nu_f, the Grashof number in equation (2.37) is actually Gr_f since it is based on the through-flow (so it is measurable) and not on the local fluid core temperature as the invariant non-dimensional Gr_c in equation (2.69).

2.5.3 Prediction of disk temperature and Nusselt number distribution

This section highlights how the Buoyancy Model can be used to predict the temperature and Nusselt number distribution along the disk radii. This is useful to engine designers. Equation (2.67) must be solved with a heat transfer equation. The heat transfer problem in a compressor cavity is conjugate: the conduction in the metal disks is coupled with the natural convection between disks and core flow. The disks can be considered circular fins (Tang et al. 2015), meaning that the fin equation can be used. In non-dimensional terms:

$$\frac{d^2\Theta}{dx^2}+\frac{1}{x}\frac{d\Theta}{dx}-\mathrm{Bi}\Theta=0 \tag{2.76}$$

where

$$\Theta=\frac{T_o-T_f}{T_{o,b}-T_f} \tag{2.77}$$

Equation (2.76) has an analytical solution. The relative intensity of the convection with respect to the conduction is summarised by the Biot number, which is defined for the purpose as:

$$\mathrm{Bi}=2\frac{b^2h_f}{t_dk_o} \tag{2.78}$$

Predictions can be made coupling equations (2.67) and (2.76). The non-dimensional temperature Θ is based on the through-flow (non-invariant), while the non-dimensional temperature θ of equation (2.70) is based on the core temperature (invariant). The same considerations of the previous section on the scalability from rig to rig apply. The relation between the two is straightforward:

$$\Theta=\frac{T_o-T_f}{T_o-T_c}\frac{T_{o,b}-T_{c,b}}{T_{o,b}-T_f}\theta \tag{2.79}$$

2.5.4 Validation method for the Buoyancy Model

Validation of the Buoyancy Model passes through experimental data confirming the temperature and the Nusselt number distributions. The calculation of the disk Nusselt number is made using equation (2.76), where the experimental temperatures are the inputs and the Nusselt number is retrieved through the Biot number. This is an inverse heat transfer problem, thus the results suffer from high errors even for limited uncertainties in the input temperatures. Conventional polynomial fits yield “wavy” behaviours of the resulting Biot number. As alternative, Bayesian statistics have been proven successful. A smoothing condition is applied to the Biot number, then Bayesian methods provide the results and a 95% confidence interval (Tang et al. 2015).

Thanks to the high enough spatial density of the measurement points, the procedure outlined above was applied to the results of the Sussex Multi-Cavity rig (Atkins and Kanjirakkad 2014) across the whole ranges of non-dimensional parameters, with the Coriolis parameter estimated from the experimental values. Temperatures and Nusselt numbers were in good agreement, with the Nusselt number increasing monotonically with

Gr_f and decreasing with Ro for other fixed conditions. Buoyancy effects were not detected for Gr_f less than $\sim 10^9$. Evidence of the compressibility effects induced by the rotational speed was captured by the model. As Re_ϕ increased above a certain value, the Nusselt number started to decrease.

Validity of the model was tested also with closed cavities (Tang and Owen 2018). The method was applied to the results provided by the RWTH Aachen rig presented in Bohn et al. 1995, showing good agreement across the non-dimensional parameter ranges. Once again, compressibility effects diminished the Nusselt numbers above a given Re_ϕ.

A comprehensive framing of the heat transfer problem in open rotating cavities with axial through-flow of coolant has been given by Tang et al. 2018. With reference to Figure 2.13, four heat transfer mechanisms occur:

- Heat transfer from disks to core: the application of the Buoyancy Model together with the circular fin equation results in the temperature and Nusselt number distributions, with the caveat that it is not known – a priori – the extent of the buoyancy dominated region.
- Heat transfer from shroud to core: a conventional correlation for laminar natural convection can be used:

$$\mathrm{Nu}_{sh} = C(\mathrm{Gr}_{sh}\mathrm{Pr})^{1/4} \tag{2.80}$$

where the subscript sh denotes shroud, $\mathrm{Pr} = c_p\mu/k$ is the Prandtl number, and C is an experimental parameter (e.g. 0.54 for horizontal plates). The shroud Grashof number is:

$$\mathrm{Gr}_{sh} = \frac{\rho_{c,b}\Omega_c^2 b}{\mu_{c,b}^2}\frac{T_{sh} - T_{c,b}}{T_{c,b}}\left(\frac{s}{2}\right)^3 \tag{2.81}$$

- Heat transfer from disk cob to axial through-flow: a forced convection correlation based only on the flow velocity can be used:

$$\mathrm{Nu}_{cob} = A\mathrm{Re}_T^B \tag{2.82}$$

  with A, B empirical constants and:

$$\mathrm{Re}_T = \frac{\rho_f U l}{\mu_f} \tag{2.83}$$

$$U = \sqrt{W^2 + (\Omega a)^2} \tag{2.84}$$

  where l is the axial length of the cob. The empirical constants have to be determined by imposing a convective boundary condition when solving the circular fin equation.
- Temperature rise of the axial through-flow: it is calculated via a control volume approach. The total thermal power resulting from the three heat transfer mechanisms concur, at steady state, to increase the temperature of the through-flow:

$$\Delta T_f = \frac{2\dot{Q}_d + \dot{Q}_{sh} + \dot{Q}_{cob}}{c_p \dot{m}_f} \tag{2.85}$$

It had been assumed that the disk thermal power divides equally between the two adjacent cavities.

Previously published experimental data support the validity of the method and the models presented here.

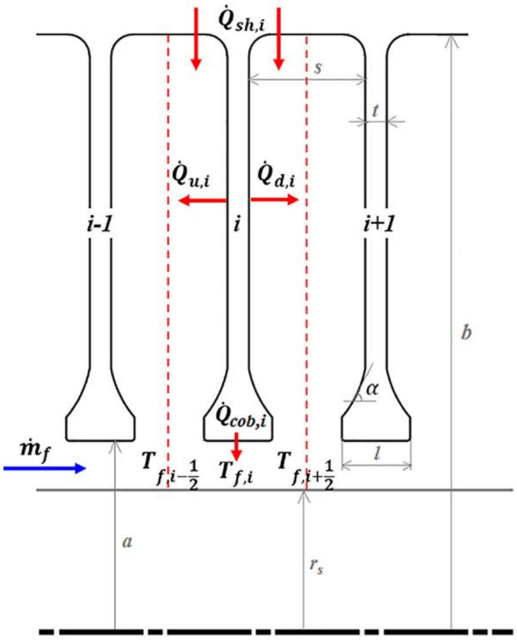

Figure 2.13 – Heat balance in a heated rotating cavity with axial through-flow (Tang et al. 2018).

All models introduced here are based on the assumption of laminar flow. The good agreement (even at the highest Grashof numbers reported in literature) is explicable considering the limited difference in rotational velocity between the cavity walls and the fluid core.

All models introduced here are based on a symmetrically heated cavity, meaning that both disks feature the same temperature and Nusselt number distributions. In a real aero engine at steady state, the downstream disk is hotter. There is little knowledge, on both the theoretical and experimental side, about the consequences of such a condition. Furthermore, during transients the temperature distributions can be reversed with stable stratified flow. The possibility of investigating differential heating of disks and transient temperature profiles is crucial to assess the ranges of validity of the model, advance the understanding of the physics and ultimately help the engine designer.

2.6 BRIEF OUTLINE OF CFD ON COMPRESSOR CAVITIES WITH AXIAL THROUGH-FLOW

Computational fluid dynamics (CFD) is a powerful tool to design the features of the internal air systems, though challenges emerge when dealing with buoyant flows in rotating cavities. Experimental evidence suggests that these flows are three-dimensional and unsteady, highlighting flow structures such as radial arms of inflow and vortex pairs. Two distinguished regimes have been identified: the first dominated by the axial through-flow (when buoyancy effects are weak) and the second dominated by buoyancy effects. Large Eddy Simulation (LES) has been proven more effective to tackle buoyancy-induced flows, even though computational efforts are much higher (Sun et al. 2007). Compared to Reynolds Averaged Navier-Stokes (RANS) methods, calculation better matched experimental velocities and heat transfer measurements for Gr in the range 10^8-10^9. A finer structure was also obtained. LES are capable of capturing both the larger eddies – interacting with the axial through-flow – and the smaller eddies responsible for the heat transfer at the disk surfaces.

Linear stability analysis and Direct Navier-Stokes (DNS) methods were used to investigate the onset of convection in a heated rotating cavity (Pitz et al. 2017). The start of convection mechanisms is associated to the formation of contra-rotating vortex pairs along the tangential direction, underpinning the hypothesis of the Rayleigh-Bénard convection. Results showed an almost homogeneous flow axially, supporting the applicability of the Taylor-Proudman theorem.

Detailed analysis of unsteady structures have been conducted on closed and open cavities via LES to calculate the flow time- and spatially-averaged statistics. The closed cavity case is relevant since buoyancy effects can be studied in isolation from the axial through-flow. In the closed cavity (Pitz et al. 2019), the calculated boundary layer thickness and velocities were approximately consistent with the analytical solution of the Ekman layer. This proved that the disk boundary layers behave as Ekman layers. The heat transfer from the shroud was found to be consistent with natural convection in horizontal plates in gravitational field, while the temperature of the cavity core was almost uniform. Calculations on the open cavity with axial though-flow were conducted for Gr ~ 10^8 (Pitz et al. 2019). Owing to the coolant flow, results revealed a significantly lower temperature in the cavity (both solid walls and core) and presence of radial arms. Once again, boundary layer thickness and velocity profiles within are consistent with the Ekman layer solution, but the agreement of velocities is qualitative. The spectral analysis showed turbulent flow in the cavity, laminar flow in the axial through-flow and unsteady laminar flow in the Ekman layers. The buoyancy-dominated region is strongly influenced by the axial flow, which generally increases the frequency content of the fluctuations in the cavity.

Thus far CFD approaches to buoyancy-induced flow in compressor cavities have proved a valid tool to give confidence to theoretical insight and support experimental data. The limited number of simulation cases and the limited magnitudes of Gr in these calculations are due to the limited computational power available.

2.7 COMPRESSOR DISK MODELLING FOR RADIAL GROWTH AND TIP CLEARANCE PREDICTION

As highlighted in Chapter 1, the overall pressure ratio of future aircraft engines will target values up to 70:1 from the current 50:1. The related tip leakage loss, especially for unshrouded rotors as those of aero-engines, would become significantly higher for the last stages of the high-pressure compressor. The ratio between the blade height and the clearance is the key parameter influencing the tip leakage loss. The reduction of the blade height is associated to the need to control tighter clearances across all the operating conditions the engine experiences. This is a very complex challenge for the designer. Accurate prediction of the tip clearance in the design stage is related to the capability of accurate modelling of the compressor rotor.

For given operating conditions, the gap G_{tip} between the blade tip and the casing can be expressed as:

$$G_{tip} = G_{CB} + \delta_{CS} - \delta_{BT} \tag{2.86}$$

where G_{CB} is the cold-build clearance (i.e. the clearance at ambient condition when the engine is off) δ_{CS} is the radial growth (i.e. radial displacement of the casing taken at the inner radius and the one at risk of rubbing the blades), and δ_{BT} is the radial growth of the blade taken at the blade tip, which is largely dependent on the growth of the disk underneath. The radial growth δ_{TOT} of the disk is calculated via the temperature distribution of the rotating cavity. It can be expressed as the sum of the thermal expansion δ_E of the material, the rotational growth δ_R due to the radial and tangential stresses induced by the rotational speed, the thermal growth δ_T due to the stresses resulting from the radial temperature gradients:

$$\delta_{TOT} = \delta_E + \delta_R + \delta_T \tag{2.87}$$

Among the components, the thermal growth has the greatest uncertainty, since it depends on the estimation of the temperature distribution on the cavity.

Simple models to calculate the time response of the tip gap of compressors during common engine transients are reported in the literature. These models are typically ready to use and fast to solve, but might be inaccurate. Agarwal et al. 2008 calculated the tip clearance during a turbine rotor transient assuming a unique bulk temperature for the ensemble of disk and blades. In the lumped methodology proposed by Kypuros and Melcher 2003 for an air-cooled turbine disk from idle to maximum power, the external shroud of the disk is in contact with the hot air in the annulus and the blades are considered disjointly from the disk. The compressor discharge temperature is considered the reference disk temperature. Such a model takes into account the thermal expansion and the rotational growth, but all the information about the thermal growth is lost in the assumption made for the disk temperature. The transient model reported by Pilidis and Maccallum 1984 has been applied for both compressors and turbines. The disk is schematised in three parts: hub, diaphragm and shroud, with experimental correlations used to evaluate the disk temperature field. However, the model has not been validated against experimental data nor FEA. A rigorous approach has been developed by Yepifanov et al. 2015. Three different 2D models were merged to predict the tip clearance and the performance changes in a turbine stage. The first is a full-rotor model with distributed forces in place of the blades and empirical correlations used to estimate heat transfer at the disk surfaces. The second is a blade model, the third a casing model. Calculations of displacements were performed on the single models via finite-element analysis, results merged afterwards. For axial compressors, the steady-state model proposed by Dong et al. 2014 was validated against available experimental data. It was based on the three sub-models of disk, shroud and blade. The shroud was simply a ring featuring thermal expansion and subject to annulus-cavity differential pressure. Experimental correlations provided the Nusselt numbers on the disk surfaces to retrieve the temperatures. The transient effects on the compressor blade clearances of common engine manoeuvres have been considered by Atkins 2013. A nominal, baseline tip clearance lumped model was fitted to engine data and a fully coupled FEA whole engine model.

As highlighted from the above review, disk modelling for tip clearance calculation is a complex topic, which can be tackled with different levels of approximation – and thus allowed inaccuracy. An experimentally validated Buoyancy Model overcomes all the empirical correlations needed for such calculations, but it is not clear how much it affects the resulting clearance values. However, at the current state the Buoyancy Model still requires empiricism and is based on a reference through-flow temperature, so that applicability to scaled designs or different geometries shall be checked case by case.

Chapter 3

Influence of temperature distribution on the radial growth of compressor disks

This Chapter originates from the paper:
Luberti, D., Tang, H., Scobie, J., Pountney, O.J., Owen, J.M. and Lock, G., 2020. *Influence of Temperature Distribution on Radial Growth of Compressor Disks. Journal of Engineering for Gas Turbines and Power,* 142(7): 071004 (10 pages). https://doi.org/10.1115/1.4046704.
It highlights and stresses the importance of disk cavity modelling to determine accurately the tip clearance of a compressor at all operating conditions reported in Section 2.7. The influence of the radial temperature profile on a HPC disk is investigated. It is demonstrated that the radial growth of the disk – which is directly related to the tip gap – is very sensitive to the temperature gradients along the disk itself.

A geometrically representative disk has been considered in isolation and modelled in three parts, i.e. a thick hub, a diaphragm and a thick shroud. The radial growth has been calculated via both a 1D model based on theoretical equations and a 2D numerical model (FEA). Results have been retrieved for three values of OPR (50, 60 and 70 to 1, from the perspective of future engines) and different temperature distributions along the disk radius. Among these distributions, the one resulting from the Buoyancy Model has been taken as a datum and compared to linear, quadratic, cubic and quartic profiles. The methodology has been extended to transient conditions as well, though through a zero-dimensional model.

3.1 INTRODUCTION

From Section 2.7, equation (2.86) and (2.87) for the tip gap and the radial growth of a disk are here recalled for convenience:

$$G_{tip} = G_{CB} + \delta_{CS} - \delta_{BT} \tag{3.1}$$

$$\delta_{TOT} = \delta_E + \delta_R + \delta_T \tag{3.2}$$

Figure 3.1 describes the three components and clarifies the difference between thermal expansion and thermal growth. The rotational growth δ_R depends on the rotational speed of the disk, which is given. Both the thermal expansion δ_E and the thermal growth δ_T depend on the operating temperature distribution of the disk. The thermal expansion is direct consequence of a physical phenomenon and related to the difference between the actual and the cold-build temperature, while the thermal growth is a consequence of the radial and tangential stresses induced on the disk by the gradients of the temperature distribution. The thermal expansion δ_E has been considered from cold-build (T_{CB}) to the temperature at the inner radius of the disk. Starting from that, the temperature increases up to the value at the shroud, causing the thermal growth.

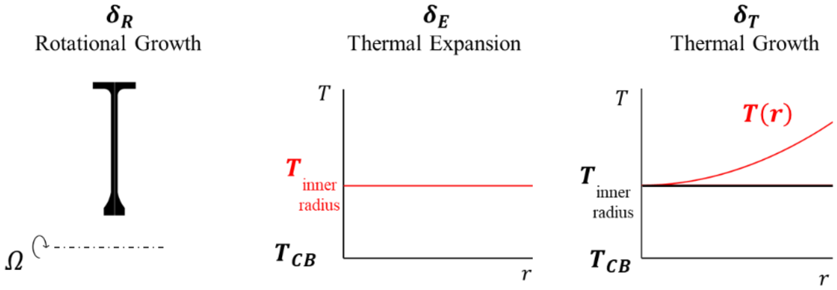

Figure 3.1 - Visual representation of the three components of growth: rotational (left), thermal expansion (centre), thermal growth (right).

The thermal growth δ_T is affected by the highest uncertainty since it is based on the assumed temperature field on the cavity walls. The core of the work was to calculate the magnitude of the thermal growth with respect to the other growth components and to compare to typical values of running tip clearance at engine-operating conditions.

3.2 DISK MODEL

When these calculation were made, the Bath Compressor-Cavity Rig was still under design. The geometry of the Multi-Cavity rig at the University of Sussex was judged as appropriately representative, though 70% scaled, of the Trent engine family (Alexiou 2000, Long et al. 2007, Atkins and Kanjirakkad 2014). For the calculations reported here that geometry has been converted back to full size. The disk was divided in three parts, i.e. a thick hub, a thin diaphragm and a thick peripheral shroud, with fillets ensuring a smooth transition at interfaces. The radial thickness of the shroud – not reported in the literature – was assumed equal to the thickness of the disk. Figure 3.2 shows the disk geometry and the dimensions used for the calculations.

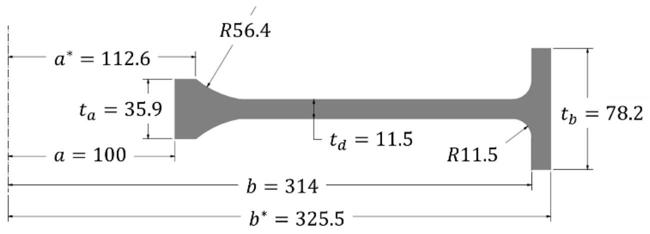

Figure 3.2 – Dimensions of the disk model expressed in mm.

High-Pressure Compressor rotors are typically made by titanium alloy, which cannot operate at more than 870 K. Owing to the very high temperatures attained in the last stages, it is common to prefer super-alloys for the last two disks (Cumpsty 2003). The continuous increase of OPR in aero-engines will promote more and more disks made of super-alloy in the future, regardless of the additional complexity given by the inertial and thermal mismatch with neighbouring titanium disks. For this reason, Inconel 718, which is one of the most common used in turbomachinery (Muktinutalapati 2011), has been selected, with properties reported in Table 3.1. The calculations have been performed assuming material properties not constant with temperature. The values reported here were linearly interpolated to build up a temperature function. For a given calculation case, the value of the property was assumed the average between inner and outer radius. FEA runs verified that this assumption does not affect significantly the results.

Table 3.1 – Properties of Inconel 718 and their dependence on temperature. The variation of density with temperature is negligible compared to the other properties.

	21°C	93°C	204°C	316°C	538°C	649°C
ρ [kg/m^2]				8193		
E [GPa]	204	199	194	187	176	169
υ	0.294	0.288	0.280	0.272	0.271	0.283
α [10^{-5} °C^{-1}] (from ambient)	/	1.28	1.35	1.39	1.44	1.51
k [W/(m°C)]	11.0	12.4	14.2	16.0	19.5	21.2

3.3 CALCULATION METHODOLOGY

At steady state, the working conditions of the engine are estimated as follows:

- Steady state (engine at cruise)
- Flight Mach number 0.85
- Altitude 10,000 m
- Ambient static temperature -50 ˚C
- Ambient static pressure 0.265 bar
- HPC rotational speed 10,000 rpm

3.3.1 Application of the Buoyancy Model

The assumptions of the Buoyancy Model were assumed valid for the analysis. The model is applied together with the 1D circular fin equation to retrieve the temperature profile and the Nusselt number along the disk radius, as described in Section 2.5.

Input values of the calculation are the air pressure in the cavity at the inner radius (p_a), the temperature at the inner disk radius (T_a) and the temperature at the disk outer radius (T_{b^*}). Assumptions have been made to estimate such values:

- The air pressure at the inner disk radius (p_a) was assumed equal to the pressure of the axial through-flow. The pressure of the axial through-flow was set equal to the IPC discharge pressure. With $OPR = 50$, this means around 14 times the inlet total pressure of the engine. This estimation comes from assumptions made on the number of stages pertaining to the compressor bodies. The through-flow pressure was assumed to increase proportionally with the OPR.
- The IPC and HPC discharge temperature were calculated assuming a polytropic efficiency of 0.95.
- The ratio given by the temperature difference between disk inner radius and HPC discharge divided by the temperature difference between IPC discharge and HPC discharge was assumed equal to 0.3 for all OPRs. The value of $\beta\Delta T$ is thus $\sim$0.3. This is believed common in modern aero-engines (Tang et al. 2018). This assumption leads to the estimation of T_a.
- The temperature at the disk outer radius (T_{b^*}) has been assumed equal to the discharge temperature of the HPC. This value has been obtained via an adiabatic compression process from ambient temperature with pressure ration equal to OPR (assumed polytropic efficiency 0.95).

Other relevant assumtions were:

- The temperature of the disk at $r = b$ has been assumed equal to the temperature of the cavity shroud. This value has been calculated via 1D heat transfer calculation across the shroud.
- The Coriolis parameter, i.e. an empirical input of the model, has been set to 0.03 to be representative of engine conditions (Tang et al. 2018).

The actual values of p_a, T_a and T_{b^*} – needed to run the calculations – are unknown. These assumptions aim at providing representative conditions starting from the published literature. Furthermore, the resulting value of the Grashof number is in the range of 10^{13}, whilst by the time these calculations were performed, the model had been only validated up to 10^{12}.

3.3.2 Finite-element calculation of temperature and radial growth

The finite-element analysis (FEA) was executed via the commercial software ANSYS v18.1. Due to axisymmetry, the disk was considered as a 2D geometry, where the centreline symmetry allowed to model only half of the cross-section profile. The mesh featured about 12,000 elements at 0.4 mm size. The temperature, stress and growth results were shown to be unchanged when the element size was reduced, confirming the grid independence.

The boundary conditions applied to the disk surfaces were (Figure 3.3):

A. Radial distribution of heat transfer coefficient between $r = a$ and $r = b$ (fillets included). The values originate from the Nusselt numbers from the Buoyancy Model.
B. Adiabatic line to represent the hidden half of the disk that behaves identically.
C. Adiabatic line to model the shroud of a neighbouring disk. Even though in real engines the shroud temperature shows an axial gradient, an adiabatic boundary is consistent with the assumptions of the Buoyancy Model.
D. Inner shroud heat transfer coefficient, as per Section 2.5.
E. T_{b^*} as assumed in Section 3.3.1 (HPC discharge temperature to model the hot air in the main annulus).
F. T_a as assumed in Section 3.3.1 (disk bore temperature).

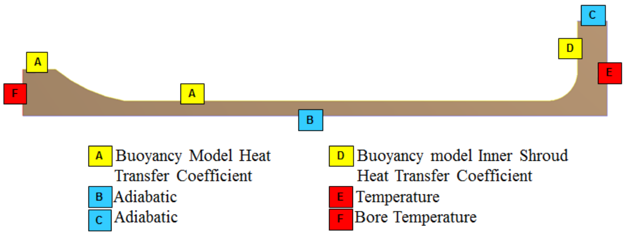

Figure 3.3 – Thermal FEA model and boundary conditions.

The Buoyancy Model, when used in combination with the 1D fin equation, predicts both Nusselt numbers and temperatures. The heat transfer coefficients, derived from the Nusselt numbers, have been applied to the FEA. Since the FEA and the Buoyancy Model had the same heat transfer coefficient, the only differences are related to the fillets, which are captured by FEA (differences in Figure 3.4 would be exaggerated in absolute scale).

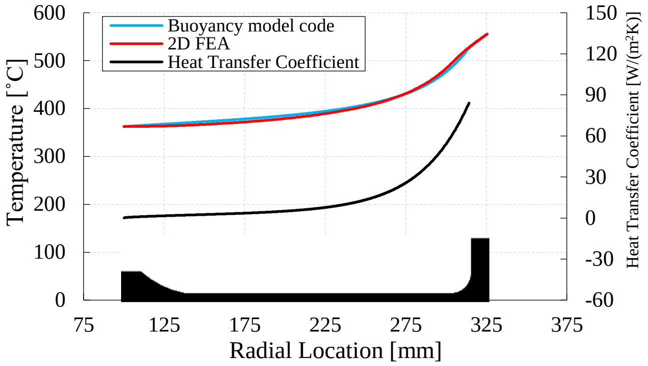

Figure 3.4 - Variation of disk temperature with radius: comparison of FEA and Buoyancy Model for OPR = 50. FEA temperature have been taken at the centreline.

3.3.3 1D stress model for radial growth

The geometry considered for the 1D stress and growth model was the same as Figure 3.2 without fillets. Comparison with respect to the original is shown in Figure 3.5. For the 1D model, the radial temperature resulting from the Buoyancy Model was considered an input.

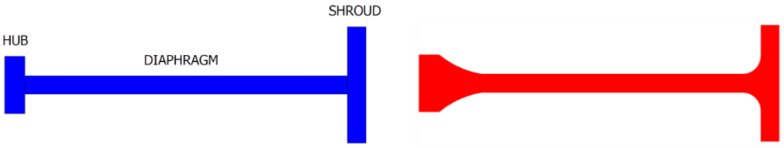

1D Model 2D FEA

Figure 3.5 – Comparison between the geometry used in the 1D model (left) and the original disk geometry (right). The latter has been used in the FEA.

Three parts were identified to comprise the disk: hub, diaphragm and shroud. For a disk featuring thermal expansion with respect to ambient conditions, rotation and radial temperature gradients, the radial stress σ_r, the tangential stress σ_t and the radial growth δ can be written as function of the radius (Vullo and Vivio 2013):

$$\sigma_r(r) = -\frac{3+\nu}{8}\,r^2\rho\Omega^2 - \frac{\alpha E}{r^2}\int_a^{b^*}(T-T_{CB})r\,dr + \frac{K_1E}{2(1-\nu)} - \frac{K_2E}{r^2(1+\nu)} \tag{3.3}$$

$$\begin{aligned}\sigma_t(r) = -\frac{1+3\nu}{8}\,r^2\rho\Omega^2 + \alpha E\left[\frac{1}{r^2}\int_a^{b^*}(T-T_{CB})r\,dr - (T-T_{CB})\right] \\ + \frac{K_1E}{2(1-\nu)} + \frac{K_2E}{r^2(1+\nu)}\end{aligned} \tag{3.4}$$

$$\delta_{TOT}(r) = -(1-\nu^2)\frac{r^3\rho\Omega^2}{8E} + \frac{\alpha(1+\nu)}{r}\int_a^{b^*}(T-T_{CB})r\,dr + K_1\frac{r}{2} + \frac{K_2}{r} \tag{3.5}$$

where symbols either have been introduced or can be found in nomenclature. Note that K_1 and K_2 are integration constants. The first terms of each equation account for the effect of the rotational speed, the second terms for the effect of the temperature field, the third terms represent the homogeneous term determined by the boundary conditions. For the sake of clarity, what is here referred to radial growth of the disk is the value of the δ_r function at $r = b^*$.

The previous equations have been specified for each of the three parts – hub, diaphragm and shroud – thus obtaining six unknowns in total (K_1^{hub}, K_2^{hub}, $K_1^{diaphram}$, $K_2^{diaphragm}$, K_1^{shroud}, K_2^{shroud}). Equations (3.3) and (3.4), specified for the three parts of the disk, dive rise to a system of six equations in six unknowns. Equation (3.5) is a linear combination of equations (3.3) and (3.4) via the Hooke's law, it can be used alternatively to one of the others. The following boundary conditions have been applied to the system:

- $\sigma_r^{shroud}(r = b^*) = 0$. The radial stress at the outer shroud radius is equal to zero. If blades were to be modelled, a distributed force, i.e. a pressure, would have been applied.
- $\sigma_r^{hub}(r = a) = 0$, as no constraints are applied to the bore, since the disk is considered in isolation.
- $\sigma_r^{diaphragm} = \frac{t_b}{t_d}\sigma_r^{shroud}$ at $r = a^*$. The shroud-diaphragm interface has to be in radial equilibrium. Thus, the radial stress at the outer radius of the diaphragm is equal the radial stress at the inner surface of the shroud, except for a scaling factor equal to the ratio of the axial thicknesses. This condition represents Newton's third law along the radial direction.
- $\sigma_r^{diaphragm} = \frac{t_a}{t_d}\sigma_r^{hub}$ at $r = b$. The hub-diaphragm interface has to be in radial equilibrium. Thus, the radial stress at the outer radius of the diaphragm is equal the radial stress at the inner surface of the shroud, except for a scaling factor equal to the ratio of the axial thicknesses.
- $\delta^{diaphragm} = \delta^{shroud}$ at $r = b$. The geometric compatibility imposes the same radial growth at the shroud-diaphragm interface.
- $\delta^{diaphragm} = \delta^{hub}$ at $r = a^*$. The geometric compatibility imposes the same radial growth at the hub-diaphragm interface.

The system solution gives the values of the six integration constants and thus the radial stress, tangential stress and radial growth functions.

Solving the system without the temperature-related terms isolates stresses and growth accountable only to rotation, i.e. the rotational stress ($\sigma_{r,R}$ and $\sigma_{t,R}$).

Solving the system with no rotation and constant temperature equal to the temperature of the inner radius (T_a) retrieves the thermal expansion. The cold-build temperature T_{CB} = 15 °C was chosen as reference ambient temperature for the thermal expansion. In this condition, the solution of the system represents the thermal expansion δ_E from the cold-build. The associated stresses $\sigma_{r,E}$ and $\sigma_{t,E}$ are zero, since a uniform temperature and no external constraints allow a free expansion.

Finally, solving the system with the temperature distribution given by the Buoyancy Model but without rotation, the thermal stresses $\sigma_{r,T}$ and $\sigma_{t,T}$ are calculated, but the resulting growth is the sum $\delta_E + \delta_T$, from which the thermal growth is retrieved.

The total stresses can be written as:

$$\sigma_r = \sigma_{r,R} + \sigma_{r,T} \tag{3.6}$$

$$\sigma_t = \sigma_{t,R} + \sigma_{t,T} \tag{3.7}$$

It is worth emphasising that the thermal growth and the thermal stresses depend only upon the temperature gradients, and not upon the actual values, as per equations (3.3)-(3.5).

3.4 COMPARISON BETWEEN FEA AND 1D RESULTS

The results for the FEA are compared with those for the 1D model at cruise conditions and OPR 50:1. This OPR is typical of state-of-the-art turbofan engines.

Figure 3.6 shows the variation of the radial and tangential stress with disk radius, comparing the solutions from the 1D theoretical model and the 2D FEA. There is general qualitative and quantitative agreement between the two solutions. The largest differences occur at the hub-diaphragm interface and at the diaphragm-shroud interface where the 1D theoretical model does not account for the fillet radii. The fillets remove the non-physical discontinuities in stress and reduce the tangential stress at all radii of the disk.

Following the approach described in the previous section, calculations were performed to isolate the rotational and thermal stresses; these are shown in Figure 3.7 and Figure 3.8 respectively. Qualitatively, there are similar features to those discussed above for Figure 3.6. The stress equations (3.3) and (3.4) have a linear solution; thus, the sum of both the radial and tangential stresses in Figure 3.7 and Figure 3.8 are equal to the radial and tangential stresses in Figure 3.6.

The total radial growth of the disk with all components expressed in equation (3.2) is shown in Figure 3.9. The total growth is the sum of the rotational growth, the thermal growth and the thermal expansion. For a given temperature difference, the thermal expansion only depends linearly on the radius; hence the corresponding curves for this component collapse for the two cases. The 1D theoretical model slightly overestimates the other growth components relative to the 2D FEA.

A summary of the growths at the outer radius is shown in Table 3.2. The thermal expansion is the largest component, followed by the rotational and the thermal growth. The average difference between the 1D and FEA growths is approximately 6%.

The tip clearance of a compressor blade can be expressed with respect to the blade chord or the blade height. These ratios change over the full range of engine operating conditions. For the last compressor stage of a large turbofan engine, these values are around 1% of the chord before, 3% after, the endurance test (Baghdadi 1996). With measurement-based predictions, the same reference reports, again for the last compressor stages, a tip clearance of 0.4 and 0.1 mm for respectively 90% and 95% of the nominal rotational speed. According to (Dong et al. 2014), the last (tenth) disk of an HP compressor has a measured running clearance of 0.3 mm. The thermal growth in Table 3.2 is of the same scale as the running tip clearances reported for engines. Importantly, this growth is directly related to the assumed temperature distribution over the compressor disk.

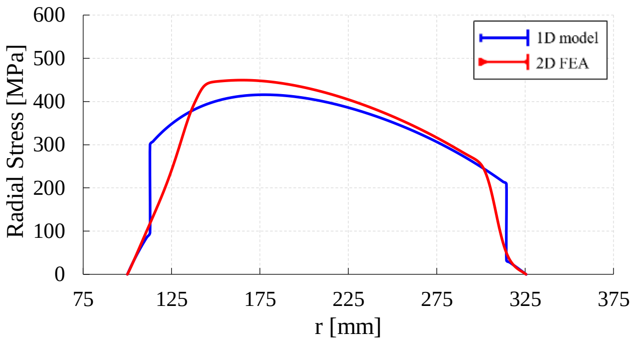

(a) Radial Stress

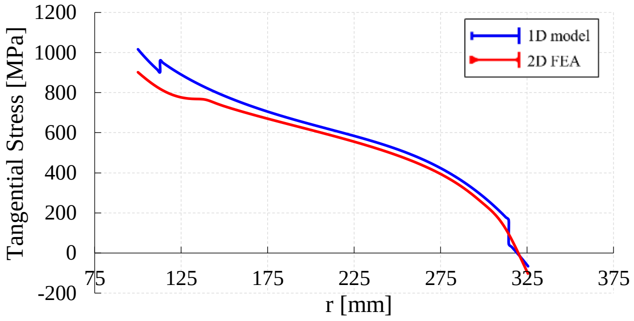

(b) Tangential Stress

Figure 3.6 - Comparison of a) radial and b) tangential stresses from the 1D theoretical model and 2D FEA (OPR = 50).

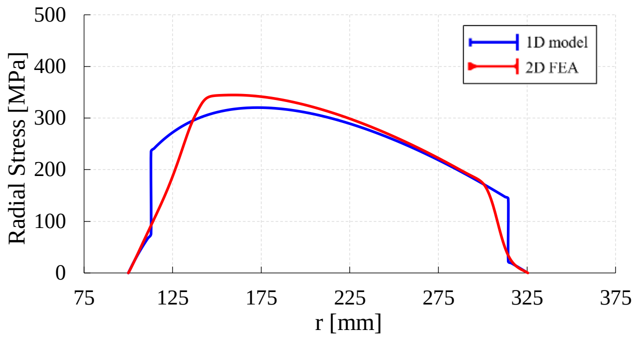

(a) Rotational part of the radial stress

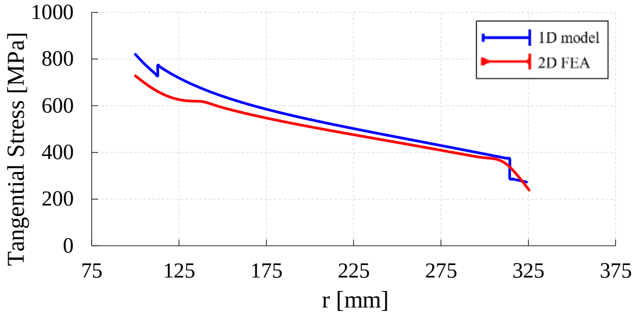

(b) Rotational part of the tangential stresses

Figure 3.7 - Comparison of the rotational part of a) radial and b) tangential stresses from 1D theoretical model and 2D FEA (OPR = 50).

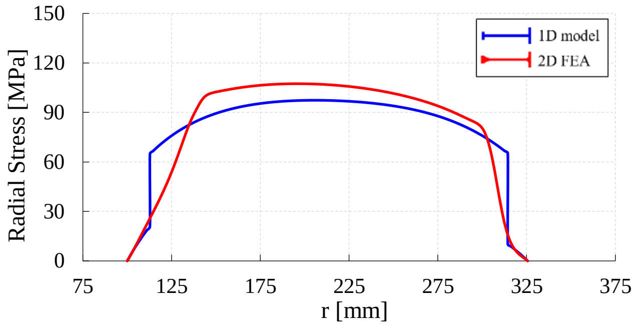

(a) Thermal part of the radial stress

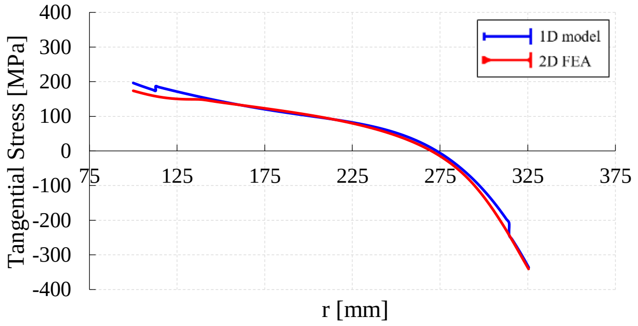

(b) Thermal part of the tangential stresses

Figure 3.8 - Comparison of thermal stresses from 1D theoretical model and 2D FEA (OPR = 50).

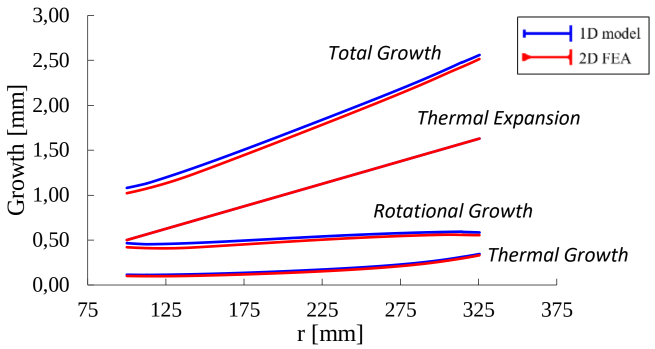

Figure 3.9 - Variation of disk growth as a function of radius; total, thermal expansion, rotational growth and thermal growth are shown (OPR = 50).

Table 3.2 – Growth components at disk outer radius (OPR = 50).

	Thermal Expansion [mm]	Rotational Growth [mm]	Thermal Growth [mm]	Total Growth [mm]
Theoretical Model	1.58	0.58	0.35	2.51
FEA	1.58	0.55	0.33	2.46

The combined solution of the coupled 1D stress and buoyancy equations took only seconds to solve on a laptop. The good agreement between the growths predicted by the 1D theoretical model and the FEA computations suggests that the combination of the 1D model and the Buoyancy Model should be useful in the preliminary calculation of blade clearances. However, as shown below, the accuracy of the predicted thermal growth depends on the accuracy of the predicted temperature distribution.

3.5 EFFECT OF OPR AND TEMPERATURE DISTRIBUTION

Previously, the temperature distribution based on the Buoyancy Model was used. This distribution has been considered a datum. The results from the datum case have been compared with those obtained using power-law temperature profiles. Power laws, which are often used for simplicity for the temperature distributions of rotating disks, provide a reasonable approximation compared to the temperature predictions obtained from the Buoyancy Model. However, although power laws might be suitable for the steady-state cases considered here, neither a single power law nor the current Buoyancy Model could fit the changing temperature profile during a thermal transient. An extension of the Buoyancy Model to transient conditions is needed to make predictions of temperatures for a given engine geometry.

Since higher pressure ratios increase the temperatures and Nusselt numbers (disk dimensions and rotational speed are here considered fixed), predictions were extended up to OPR = 70. The Grashof numbers for each pressure ratio (50:1, 60:1 and 70:1) were 1.2×10^{13}, 1.5×10^{13} and 1.7×10^{13}.

The generic power-law profile is given by

$$T(r) = T_a + K(r - a)^{n_{ex}} \tag{3.8}$$

Here the constant K for each value of n is determined by imposing the relevant outer-shroud temperature, which is assumed to be the total temperature at the HPC discharge. The exponent n_{ex} determines the *shape* of the profile, which determines the thermal stress. The power laws considered are linear, quadratic, cubic and quartic (i.e. n_{ex} = 1, 2, 3, 4).

Neither the change of temperature profile nor the overall pressure ratio alters the rotational growth (δ_R) which depends only on rotational speed (assumed constant here). However, the thermal expansion (δ_E), is affected by the OPR, as the temperature at the bore (T_a) increases with OPR. The thermal growth δ_T is affected by both the temperature distribution and the OPR.

Figure 3.10, Figure 3.11 and Figure 3.12 show the variation of thermal growth with radial position for OPR = 50, 60 and 70, respectively (all results were obtained using FEA). These figures illustrate the effect of the different temperature profiles. In all cases the Buoyancy Model, which is used as a datum, yields a thermal growth bounded by those obtained from the temperature profiles for n_{ex} = 3 and 4. Generally, results from the Buoyancy Model match the n_{ex} = 3 power law at the lower radii, with some deviation at the higher radii (in the range of 8-10% at the outer radius, according to OPR). At higher OPR (towards 70:1) results from the Buoyancy Model ~~are very close to~~ tend to match the n_{ex} = 4 power law, showing 3% difference at the outer radius.

Figure 3.13 shows the variation of calculated thermal growth at the disk outer radius with OPR. The gradient of the thermal growth obtained using the Buoyancy Model is lower than any analysed power law. The model gives a thermal growth, which is less sensitive to the overall pressure ratio.

Table 3.3 shows the thermal expansion, thermal growth, and the total growth calculated at the outer-shroud radius from the different temperature profiles at the three OPRs. The total growth includes the rotational growth. At OPR = 50, the Buoyancy Model yields a thermal growth bounded by those obtained from the temperature profiles for n_{ex} = 3 and 4; at 70:1 the calculations are much closer to that determined from the n_{ex} = 4 order profile. By contrast, a linear power-law causes errors the same magnitude as the thermal growth itself.

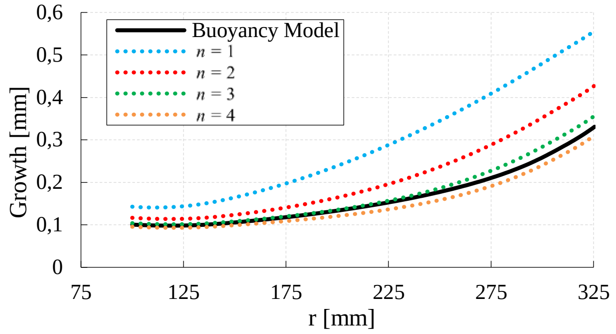

Figure 3.10 - OPR = 50: thermal growth comparison between Buoyancy Model and power-law.

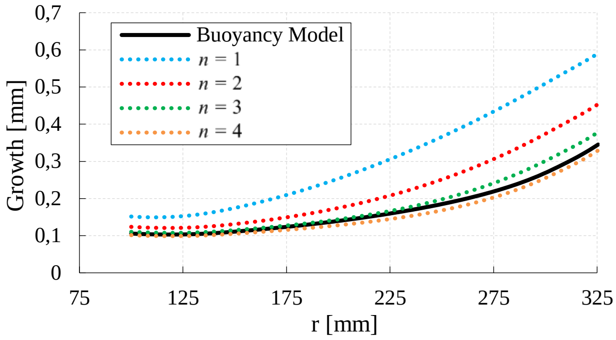

Figure 3.11 - OPR = 60: thermal growth comparison between Buoyancy Model and power-law.

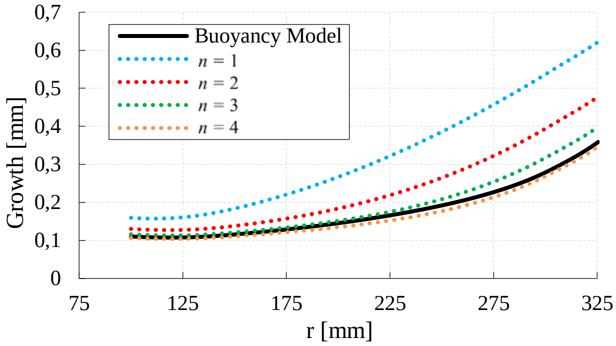

Figure 3.12 - OPR = 70: thermal growth comparison between Buoyancy Model and power-law.

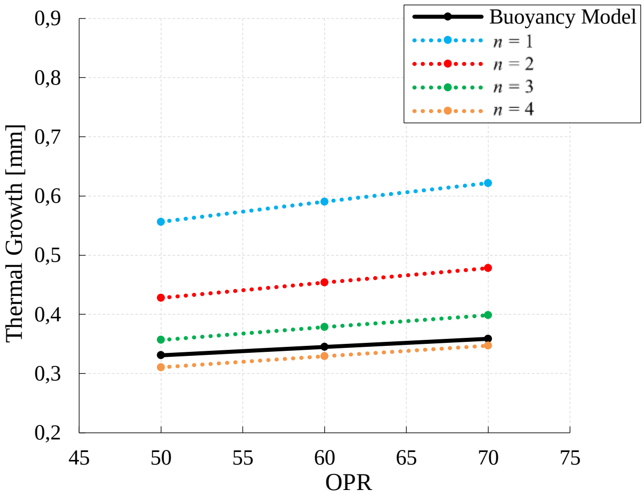

Figure 3.13 - Variation of thermal growth at disk outer radius with OPR.

Table 3.3 - Effect of temperature distribution and pressure ratio on thermal expansion, thermal growth and total growth of the disk; values in mm.

	OPR = 50		OPR = 60		OPR = 70	
Thermal Expansion	1.58		1.76		1.92	
	Thermal	Total	Thermal	Total	Thermal	Total
Buoyancy Model	0.33	2.47	0.34	2.66	0.36	2.85
$n = 1$	0.56	2.70	0.59	2.91	0.62	3.11
$n = 2$	0.43	2.57	0.45	2.77	0.48	2.97
$n = 3$	0.36	2.50	0.38	2.70	0.40	2.89
$n = 4$	0.31	2.45	0.33	2.65	0.35	2.84

3.6 EXTENSION OF THE METHOD TO TRANSIENT CONDITIONS

Aircraft engines are required to maintain the performance and avoid damages during all transient conditions. The incompatibility in thermal inertia between the HPC rotor and the casing, together with the changing engine speed, can result in minima in the tip clearance, with the possibility of rub. This flight scenario is often referred to "hot re-slam", i.e. a deceleration followed by a slam acceleration, occurring for example in case of aborted landing.

A typical transient approach for rotor growth calculation consists in modelling the single rotor parts with concentrated – or "lumped" – parameters (Pilidis and Maccallum 1984, Yepifanov et al. 2015), which involves a constant temperature and a single time constant for an entire compressor disk. That approach provides no details of the temperature *gradient*, and hence it cannot calculate the transient thermal growth. The method outlined below can be used together with a lumped transient model to show the transient response of each growth component.

First, the Buoyancy Model is solved for the initial and final steady-states to calculate the two separate distributions of the radial temperature and heat transfer coefficient. The area-averaged heat transfer coefficient $\bar{h}$ is then used to estimate a time-constant, τ_c, for each steady-state:

$$\tau_c = \frac{\rho V c}{\bar{h} A_{disk}} \tag{3.9}$$

The time-constant for the whole transient evolution is assumed to be the mean of the two values. This can be considered a best guess assumption if experimental data are not available (the Bath Compressor-Cavity Rig would provide transient data). The transient temperature is then given by:

$$T(r,t) = T_{SS1}(r) + [T_{SS2}(r) - T_{SS1}(r)](1 - e^{-\frac{t}{\tau_c}}) \tag{3.10}$$

This equation can then be applied to a transient finite-element simulation to calculate the transient growth.

A realistic flight scenario is when a reduction of cruise speed occurs, and the initial and final steady-states (SS1 and SS2) are reported in Table 3.4. The calculated mean time-constant is about 15 minutes, and Figure 3.14 shows the corresponding steady temperature distributions.

Table 3.4 - Cruise steady-states considered for the transient analysis.

	SS1	SS2
Altitude [m]	10,000	10,000
N [rpm]	10,000	9,500
OPR	50	45
Flight Mach number	0.85	0.77

In an engine manoeuvre, the rotational growth is the fastest to respond, and a deceleration of 50 rpm/s is assumed. After applying the interpolated transient temperature history from SS1 to SS2 using equation (3.10), the transient radial growths – calculated using FEA – are shown in Figure 3.15. The rotational growth decreases synchronously with the rotational speed. The thermal expansion, though with a transient, decreases as well, owing to the monotonic decrease of the bore temperature caused by deceleration. The thermal growth behaviour depends on the temperature gradient of the initial and final states, and – as the temperature gradient is lower at SS2 – the thermal growth decreases.

From the stress point of view, the highest values are attained at the disk bore also during the transients. During the engine transients, the stress values at the bore are driven by the thermal gradients inside the disk cobs. The cobs are the disk section with the highest thermal inertia, and strong temperature gradients arise during the engine heating and cooling transients. However, the effects of these gradients on the disk stresses – and thus on the growth – cannot be taken into account in the calculation shown here, as the calculation considers a transient between two steady states with only a temperature value and no heat transfer assigned at the bore (reference temperature is the through-flow).

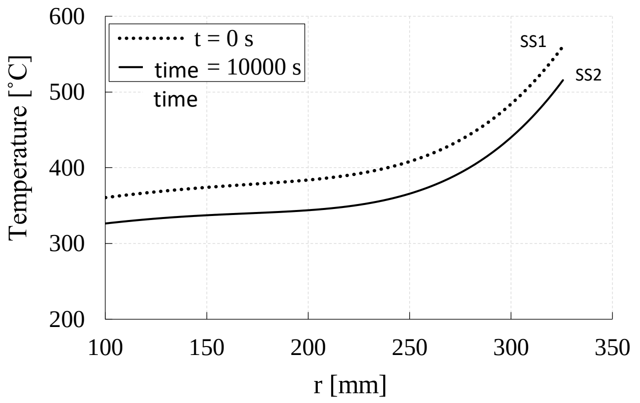

Figure 3.14 - Initial (SS1) and final (SS2) temperature distributions.

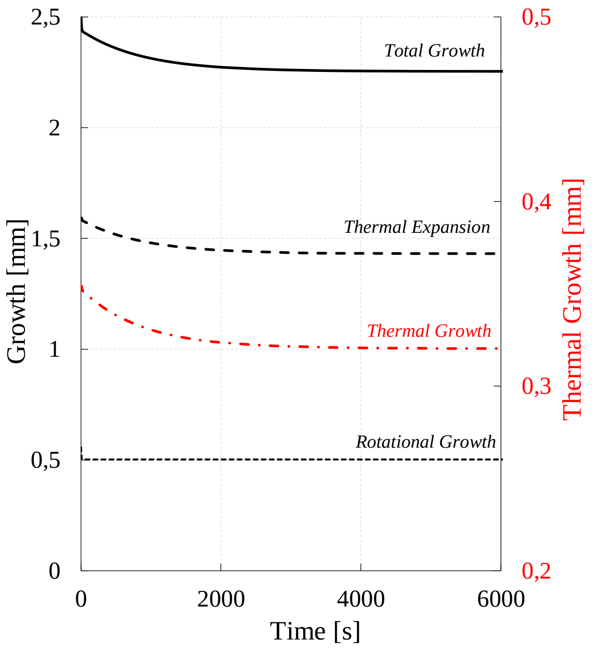

Figure 3.15 - Transient response of the disk growth components for a cruise speed reduction.

3.7 SUMMARY AND MAIN FINDINGS

The blade clearances in a compressor depend strongly on the radial growth of the disks to which the blades are attached. The overall radial growth of a compressor disk depends on: the *thermal expansion* of the material; the *rotational growth* due to the stresses created by the rotational speed of the disk; and the *thermal growth* of the disk due to the stresses created by the temperature gradients. For thermal growth, the temperature gradients depend in turn on the Nusselt numbers created by the buoyancy-induced rotating flow in the fluid core in the cavity between adjacent disks. As the Nusselt numbers depend on the radial temperature distribution in the disk, this is a complex conjugate problem, which represents a challenge for the designer.

The three growth components have been calculated separately for a single disk operating at the steady-state conditions associated with compressor pressure ratios of 50, 60 and 70 to 1. At each pressure ratio, calculations were conducted for five different temperature distributions: the distribution based on the Buoyancy Model was used as the datum case, and results from this were compared with those from linear, quadratic, cubic and quartic power laws. For the 50:1 pressure ratio, the calculations were conducted using both FEA and a theoretical 1D stress model.

For the cases considered here, the radial distribution of temperature has a significant effect on the disk growth and consequently on the blade clearance in a compressor. Although the growth due to the thermal stress is small relative to the total growth of the disk, it is the same magnitude as the blade clearance.

Using the Buoyancy Model as a datum for comparison with the growth predicted using power-law temperature distributions shows that a quartic power-law produces the most accurate results. By contrast, a linear power-law causes errors the same magnitude as the thermal growth itself. Although a power-law profile might be suitable for the steady-state cases considered here, no single power law could fit the changing temperature profile during a thermal transient. Only transient modelling is able to predict the evolution of the thermal growth during a manoeuvre. The design of the Bath Compressor-Cavity Rig allows with limited modifications the measurement of the radial growth of the disks in both steady-state and transient conditions.

For the assumptions used in the calculations, the pressure ratio has a relatively small effect on the thermal growth.

There was good agreement between the growths predicted by the 1D model and the FEA computations. This suggests that the combination of the 1D model and the Buoyancy Model could be useful in the preliminary calculation of blade clearances. Note that the combined solution of the coupled 1D stress and buoyancy equations took only seconds to solve on an ordinary laptop.

A lumped-parameters transient model has been run between two engine steady states in a deceleration scenario. Consistently with the assumptions of the calculation, the time behaviour of the thermal expansion is related to the disk bore temperature, while the time behaviour of the thermal growth depends on the initial and final shape of temperature distribution.

As a final *caveat*, the results presented in chapter were based on conditions thought to be representative of those in aero-engine compressors; they might not apply to actual conditions. In addition, it should be noted that the Grashof numbers based on the assumed conditions were higher than the values the Buoyancy Model has been, so far, fitted and validated.

Chapter 4

Thermo-mechanical analysis of the Bath Compressor-Cavity Rig

The Bath Compressor-Cavity Rig has been designed to address the unknowns of buoyancy-induced flows in heated compressor cavities with axial through-flow and meet the objectives listed in Chapter 1.

This Chapter describes the thermo-mechanical analysis of the rotating disks of the rig. The calculation of the stresses due to the mechanical and thermal loads is pivotal to support and validate the design. As of today, the rig has been constructed as part of EPSRC grant EP/P003702/1, entitled *Buoyancy-Induced Flow and Heat Transfer inside Compressor Rotors*. The grant is conducted in collaboration with Rolls-Royce plc, who have reviewed the stress calculations presented here and approved the methodology. The analysis was performed during the last stages of the design, such that few details – non-relevant for the performance – are slightly different from the actual built. Design philosophy, rig capabilities, measurements, installation and commissioning are presented in Chapter 5.

According to the calculations and the design modifications presented here, the disk pack of the rig is satisfactory in terms of life and safety requirements.

4.1 INTRODUCTION

The Bath Compressor-Cavity Rig has been designed as a partnership between Torquemeters Ltd. and the Turbomachinery Research Centre at the University of Bath. A cross-section is shown in Figure 4.1; the this analysis deals with the rotating disks only. The component marked as the “swan neck”, has a spline in its inner surface, and thus the shaft spins it. The swan neck is directly attached to a ring element, and there are four disks locating three cavities. A cylindrical element marked as the “intake” is attached to the disk pack. The disks are numbered from 1 to 4 starting from the intake side; the cavities are numbered 1 to 3 in the same direction. Inside the bore of the disk pack there is a stationary shaft. Around disks 2 and 3 static radiant heaters are located to heat the shrouds. The internal walls of cavities 1 and 3 are covered with insulating material. In the analysis, the insulation is replaced with adiabatic boundaries. The radial access to cavities 1 and 3 is obstructed by spacers made of insulating material, referred as “Surrey inserts”. At the entrance of the inner cavity, there are two ring-like elements referred as “cob attachments”.

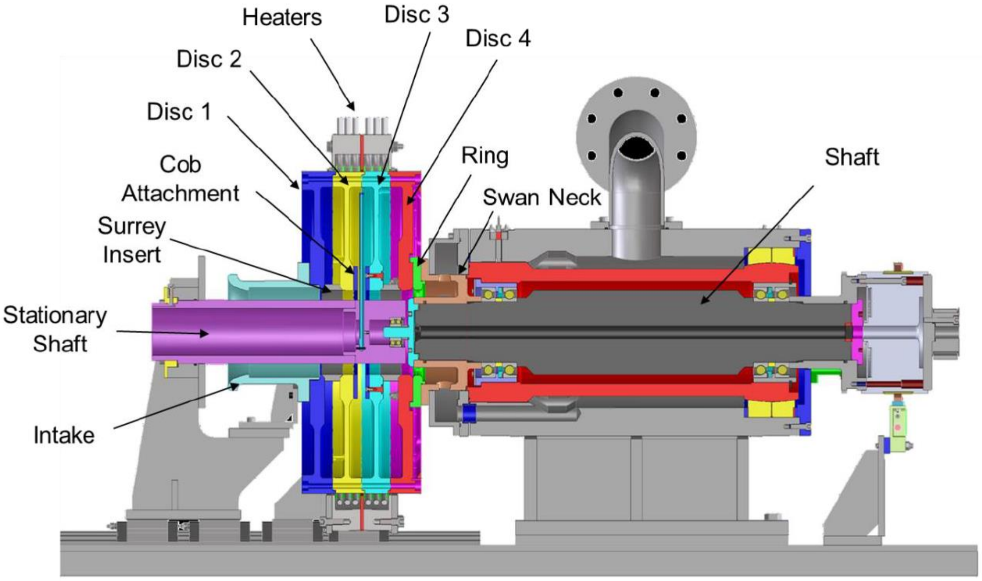

Figure 4.1 – Bath Compressor-Cavity Rig cross-section as used in the stress analysis.

4.1.1 Design requirements

The maximum rotating speed of the disk pack was specified at 8,000 rpm. The rig life is to be 10,000 cycles. The operational requirements are listed as follows:

- 10,000 cycles life;
- every cycle is from zero rotational velocity to 8,000 rpm;
- during every cycle, the outer radii of disk 1 and 2 are heated to 150 °C.

The objectives of the analysis are as follows:

- provide a qualitative and quantitative analysis of the rig behaviour under the load, understanding the way it is deformed during normal operation;
- optimise machined geometries related to the instrumentation in order to improve the rig life;
- determine the capability of the rotating components to withstand, for the 10,000 required cycles, the thermal and mechanical stresses.

4.1.2 Material data

Figure 4.2 specifies the chosen materials; all the components are made of titanium alloy, except for the attachments and the intake, made of aluminium alloy, and the inserts, made of Rohacell, an insulating material common in the aerospace sector. Table 4.1 summarises thermal and mechanical properties of interest for the analysis. The ultimate tensile strength of the selected titanium alloy is 948 MPa and the yield strength is 889 MPa. The yield strength has been used as a limit for the design, discarding the possibility for the disks to work in the plastic region at any location.

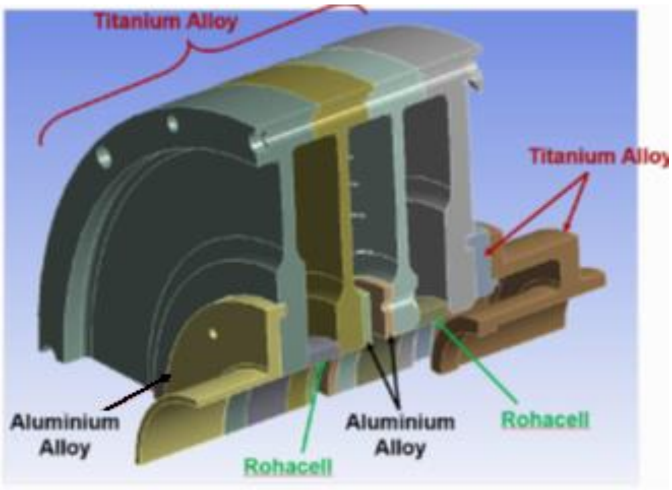

Figure 4.2 – Materials of the rotating disk pack of the rig.

Table 4.1 – Thermal and mechanical properties of the materials of the rotating disk pack.

	TITANIUM ALLOY (Ti-6Al-4V)	**ALUMINIUM ALLOY**	**ROHACELL**
Density [kg/m^3]	4620	2770	52
Thermal Expansion Coefficent [°C^{-1}]	$9.4 \cdot 10^{-6}$	$2.3 \cdot 10^{-5}$	$3.5 \cdot 10^{-5}$
Young's Modulus [GPa]	96	71	0.35
Poisson's Ratio	0.36	0.33	0.25
Yield Strength [MPa]	889	280	/
Ultimate Tensile Strengh [MPa]	948	310	2
Thermal Conductivity [W/(mK)]	7	144 (0°C) 165 (100°C)	0.03

4.1.3 Approach and methodology

The analysis was performed with an Academic License of the finite element software ANSYS v18.1.

The rotating components of the rig are subject to a combination of thermal and mechanical loads. The thermal loads are due to the heating of the periphery of the disks, which naturally result in a differential thermal growth. Thermal stresses are directly related to the temperature gradient field and also to the mechanical boundaries, since the thermal expansion of the inner disks is constrained. The applied mechanical loads are instead centrifugal load and gravity. In the software environment, thermal and mechanical loads can be accounted combined. The thermal solution is retrieved from the input geometry and material data, the results loaded in the structural module, whose solution is comprehensive of both types of loads (Figure 4.3). To reduce the computational effort, a one-quarter sector of the model is used and the spline removed. The bolts are not considered for the sake of simplicity. Transient calculations are beyond the scope of the analysis.

The analysis is organised as follows. First, the thermo-mechanical problem is solved for the disk pack as initially designed using conservative assumptions for the heat transfer. Then, design improvements to reduce the stresses in critical areas are presented. A discussion on the acceptability of the results follows. It is vital to check if resulting stress levels and the deformation modes agree with the principles of solid mechanics, increasing the confidence in the calculation setup and results. The thermal boundaries are then further refined and the results retrieved. At the end, safety assessment, fatigue analysis and crack propagation study are presented.

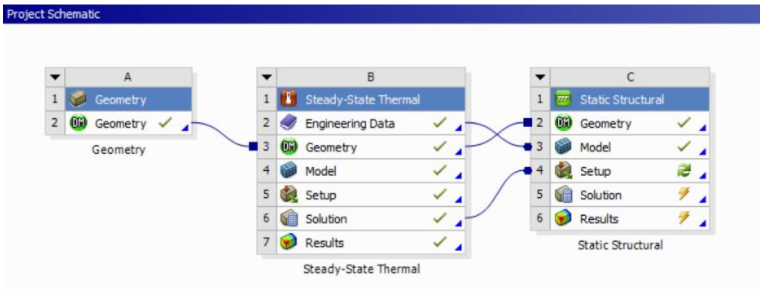

Figure 4.3 – ANSYS Calculation flowchart.

4.2 THERMAL SIMULATION

Tangential and radial stresses are generated when a disk is subjected to a radial temperature gradient (Vullo and Vivio 2013). The temperature field of the disk pack during the required working conditions – which is actually within the scope of the rig – has to be estimated.

4.2.1 Setup and boundary conditions

First, the contacts are defined. Where an axial contact is physically represented by bolt-joined surfaces, a reasonable approximation is to set the contact as “bonded”, i.e. acting as if they were welded to each other (Figure 4.4a). Where there are no bolts (e.g. radial fits and Surrey inserts), a “frictional” contact is used, with frictional coefficient equal to 0.15 for titanium-titanium and 0.2 for titanium-Rohacell contacts (Figure 4.4b). Contacts always allow for heat conduction. Radial fits between the disks are set to 0.05 mm interference, as per design.

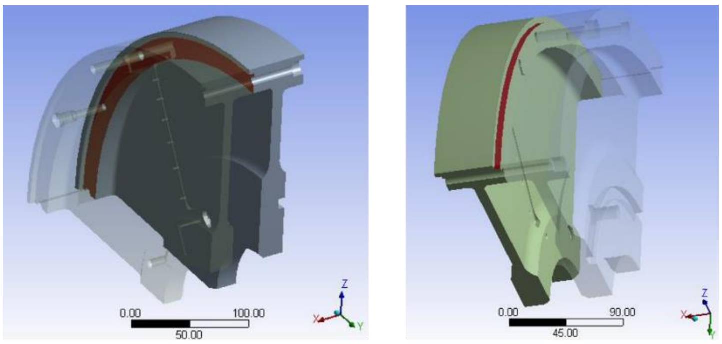

a) *b)*

Figure 4.4 – Examples of contacts in the disk pack; a) “bonded”; b) “frictional”.

A mesh with “curvature size function” was used (Figure 4.5). There was no need to refine features since this would not affect the temperature field. The process resulted in circa 325,000 elements.

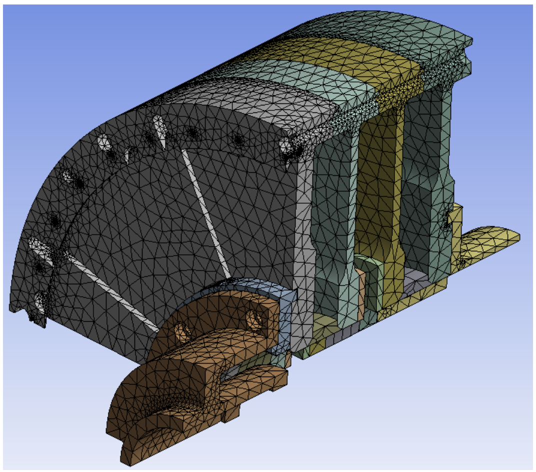

Figure 4.5 – Thermal simulation mesh.

The maximum thermal stresses occur at maximum temperature gradients. To determine the worst-case scenario, thermal boundaries that result in the highest temperature gradients must be used. For this purpose, the highest temperature difference between shroud and inner radius is considered (highest non-dimensional temperature θ) and correlations are used with the highest rotational speed. Figure 4.6 shows the boundary conditions. The free-disk convection correlation is taken from (Owen and Rogers 1989), while a correlation for a rotating cylinder provided by Dorfman 1963 is used on the external shrouds. The temperature at outer shroud on the disks is fixed at 150 °C (blue surface, as from rig specification). The disk-pack bore is set at 20 °C to maximise the temperature gradient. Internal walls of cavity 1 and 3 are adiabatic to model the Rohacell insulation layers. The inner shroud of cavity 2 has a fixed temperature of 105 °C, as estimated with the theoretical Buoyancy Model in conjunction with the fin equation – as in Tang et al. 2018 – applied to the Bath Compressor-Cavity Rig. Predictions are used to determine the surface temperatures of the disks in cavity 2. Even though validation is not complete, this method is the most updated that can be found in literature and assumed the closest to reality. To maximise the temperature gradient on the disks, shroud heat conduction from cavity 2 has been impeded.

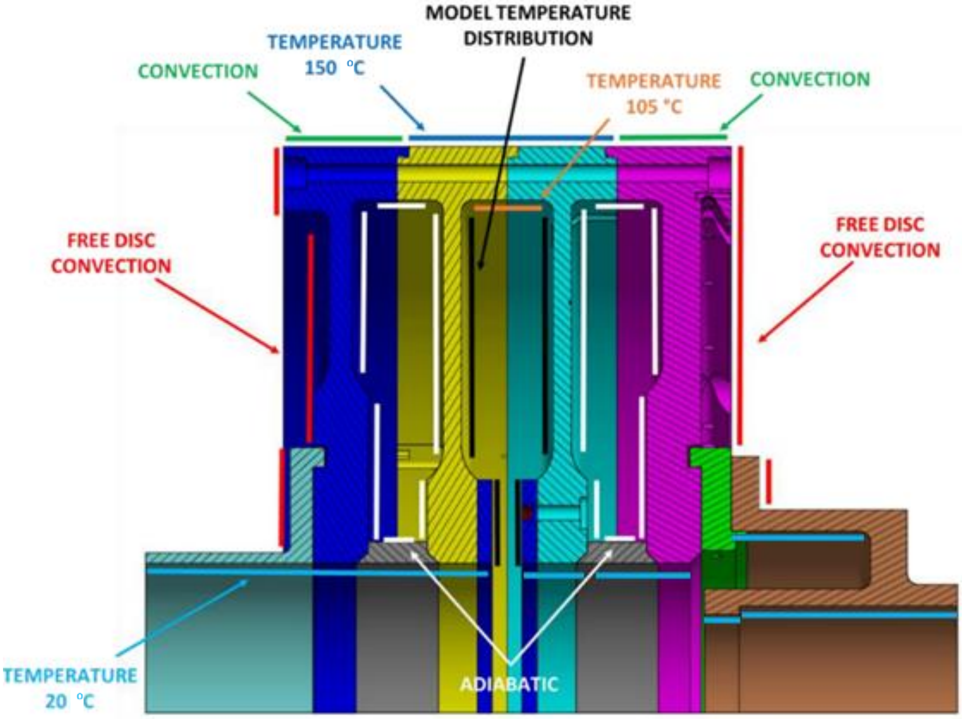

Figure 4.6 – Thermal boundary conditions.

4.2.2 Thermal results

An iterative solver was used to obtain the solution; temperature results are reported in Figure 4.7. Most of the pack is cooler than the shroud, highlighting the strong gradients along the inner disks responsible for the thermal stress.

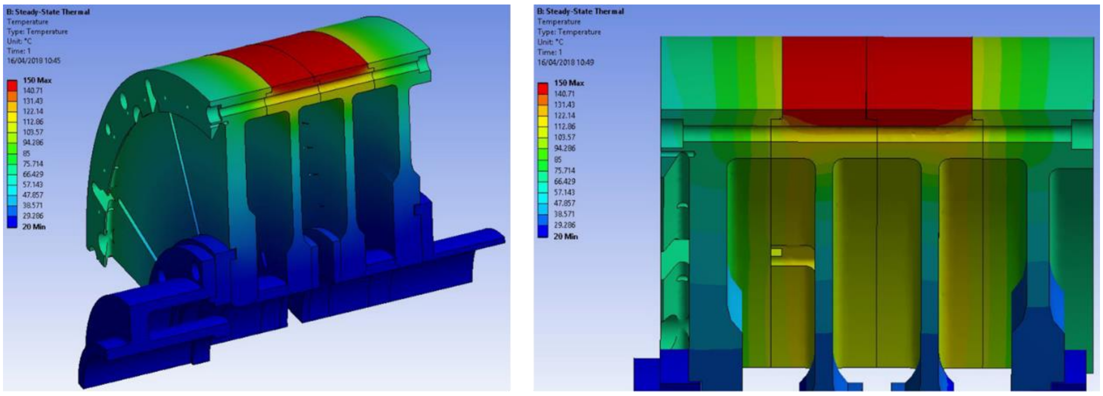

a) *b)*

Figure 4.7 – Calculated temperature field of the disk pack; a) whole sector model; b) detail of the shroud.

4.3 THERMO-MECHANICAL SIMULATION

The most critical unknown of the thermo-mechanical simulation is the position of the maximum stress. Starting from a coarse mesh, refinements can be made to the features suspected to act as stress risers. Meshing is thus an iterative process during the calculation setup.

4.3.1 Setup, boundary conditions and loads

The contacts are defined as described in section 4.2.1. A coarse mesh with “curvature size function” was used (Figure 4.8).

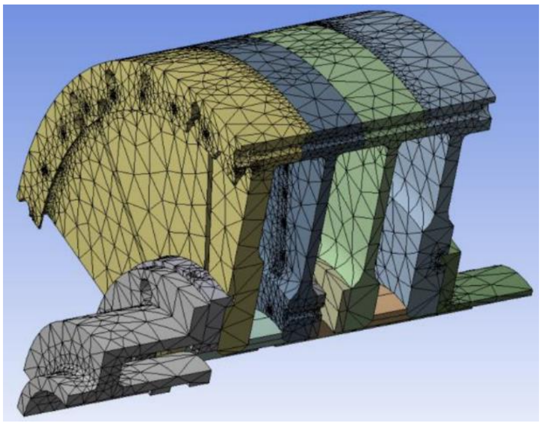

Figure 4.8 – Initial mesh of the thermo-mechanical simulation.

The thermal solution is exported to the structural simulation environment as a thermal load. The mechanical loads acting on the disk pack are gravity and centrifugal force. Gravity is neglected as it does not affect the disks significantly (the bolts are responsible for keeping the disks together – cantilever design). The rotational speed is set at 840 rad/s (8,000 rpm). Since a quarter model is simulated, on the cut surfaces a zero-normal displacement boundary has to be applied. To reproduce the presence of the shaft (whose stiffness is assumed infinite), a zero-normal displacement has been applied to the swan neck end. Mechanical power is supplied through to the spline, and thus it supports the whole pack. The representative boundary is “cylindrical support”, allowing the disks to grow in the axial and radial directions.

4.3.2 Thermo-mechanical results

The inner disks host circumferential slots to install thermocouples on the cavity walls. Each thermocouple bead is at the end of a machined groove, with the wires running tangentially until turning to the backside via a through-hole and glued along the path. The thermocouples are organised onto the disk surfaces in four sectors, and in each sector the slots are placed at different radii, spanning from the inner radius to the shroud. Further details and visual representation are provided in Chapter 5.

Meshes with refinements on the different geometrical features have been used for the calculation to spot critical locations, with the refinements stopped until mesh-independence was achieved. The most critical location for the stress is found on the disk diaphragm in the thermocouple slot at the lowest radius. The mesh refinement on the slot (front and back) is reported in Figure 4.9. The process resulted in approximately 306,000 mesh elements.

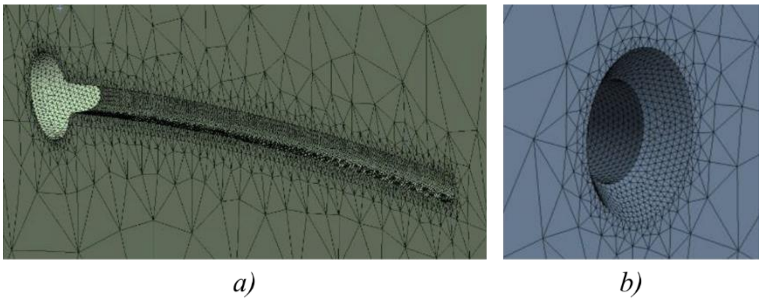

a) b)

Figure 4.9 – Details of the mesh refinements on the thermocouple slot the lowest diaphragm radius; a) inner disk surface; b) back surface.

The von Mises equivalent stress field is reported in Figure 4.10, together with the detail of the critical thermocouple feature. The highest stress location is at the intersection between the tangential groove and the through-hole. The equivalent stress attains 1140 MPa. Other thermocouple slots have been refined and tested, but stress values are lower. Note that the model used is linear elastic: the solver can show stress values higher than the yield or the ultimate tensile strength.

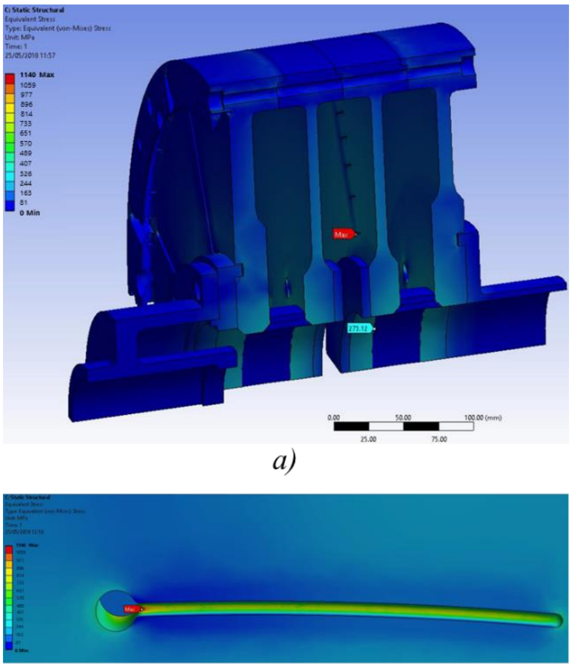

a)

b)

Figure 4.10 – Equivalent stress field (von Mises); a) whole disk pack sector; b) detail of the highest stress location (thermocouple feature).

This high level of stress in the feature would mean local areas of plastic deformation. It is preferable to have elastic deformation everywhere. This might be achieved changing the geometry. Regardless of the features acting as stress risers, the equivalent stress at the disk bores – which is the highest "*unfeatured*" stress – is ~275 MPa (Figure 4.10a). The large majority of the disk is mildly stressed compared to the yield strength of the material. Geometric changes can sensibly reduce the stress levels at the critical feature to increase the disk pack reliability.

4.4 DESIGN MODIFICATIONS

Rotation induces in a disk a tangential stress, which is the highest at the bore and lowest at the outer diameter, plus a radial stress, which is zero at the inner and outer radii but a maximum close to the bore. The centrifugal stress is everywhere larger than the radial stress. A temperature gradient induces a circumferential stress, which has a maximum at the bore and passes through zero before the outer radius, plus a radial stress, which is zero at the inner and outer radii but a maximum close to the bore (Vullo and Vivio 2013). This means that, in general, the bore radius is the most stressed location. Features in the disk diaphragms can influence the location of maximum stress.

4.4.1 Thermocouple slots on the diaphragms

To explain the location of the maximum stress in Figure 4.10, the deformation field has to be considered (Figure 4.11). At the first radial slot in the diaphragms the disks are bent, increasing the radial component of the stress at that location. A study of the deformation has been carried out to assess the level of stress, and is reported in Section 4.5.

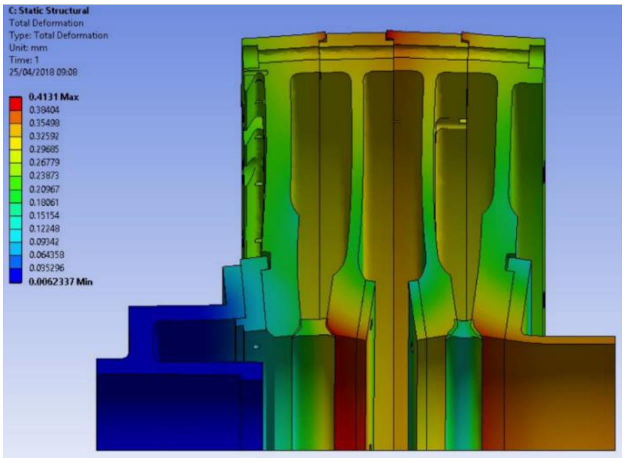

Figure 4.11 – Total deformation field of the disk pack. The deformation is expressed in absolute terms and in mm (sometimes called "displacement").

To alleviate the stress at the thermocouple slot, the fillet radius can be increased. However, the signal would experience higher thermal disturbance. To address these conflicting effects, the slot can be split in two. The first part departs from the hole with high fillet radius (2 mm) and high width (2 mm) to guarantee enough penetration in the disk surface of the bonding material. The second part has the original width and depth of 0.5 mm with 0.25 mm fillet radius. The two parts are blended together smoothly. The depth is kept constant at 0.5 mm along the entire feature. Figure 4.12 compares the improved design with the initial slot; Figure 4.13 shows a section of the improved design. A fillet radius on the hole edge has also been added on the back face. This location is also highly stressed.

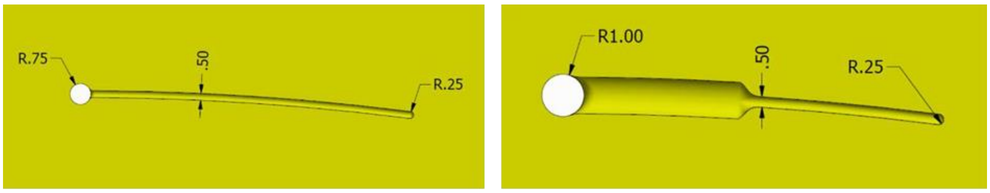

a) *b)*

Figure 4.12 – Design comparison of thermocouple slots; a) initial; b) final.

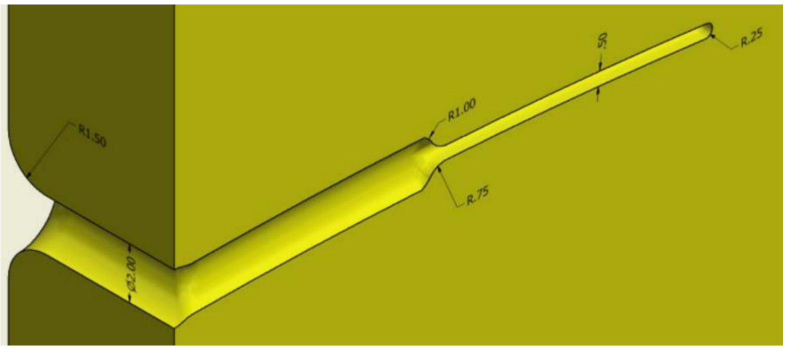

Figure 4.13 – Cross-section of the thermocouple feature. The backside edges of the hole have been rounded to reduce the stress.

4.4.2 Thermocouple slots on the cobs

Four thermocouple features were originally designed on the cob lateral surface at 90° from each other. Although the computed stress levels are below the elastic limit, good design practice suggests avoiding holes and other stress risers close to the bore. A new design was proposed and compared to original (Figure 4.14). To reduce manufacturing time, the four cob slots are grouped in two and arranged at 180° from each other, with a single hole as far from the cob as practicable. There is a common groove for the thermocouple wires, intended to be filled with epoxy.

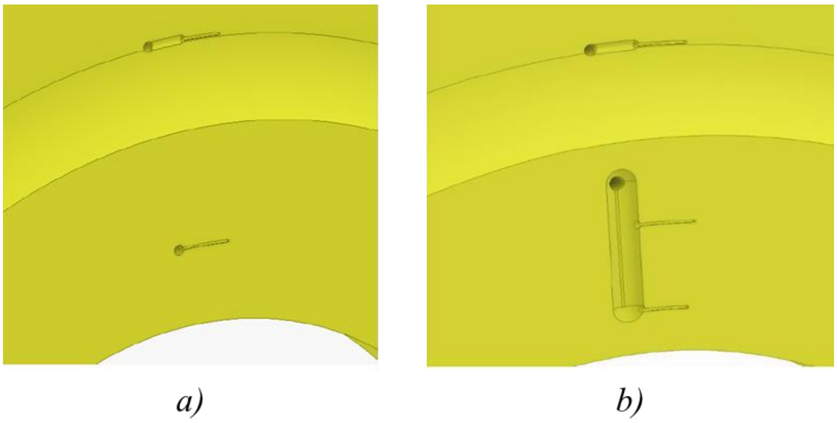

Figure 4.14 – Design comparison of cob thermocouple slots; a) initial; b) final. The holes are moved the furthest possible away from the disk bore.

4.4.3 Assessment of the design changes

The new geometries were simulated with the same methodology discussed in Sections 4.2 and 4.3, with the same boundary conditions and loads. The mesh had 5 mm elements (Figure 4.15) and refinement of the critical thermocouple slots lead to elements down to 0.06 mm (mesh growth ratio of 1.45). Details are shown in Figure 4.16. The process resulted in 2.46 million elements.

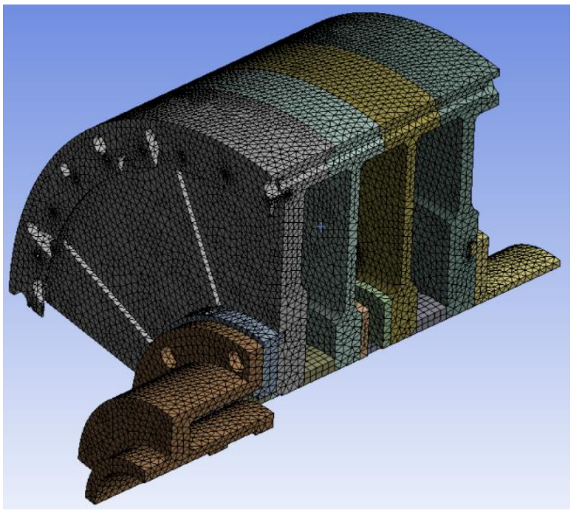

Figure 4.15 – Fine mesh of the thermo-mechanical calculation.

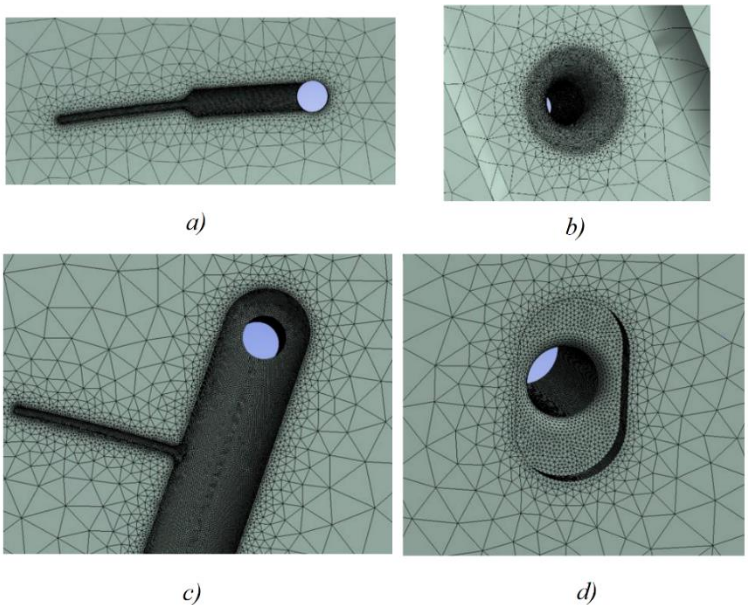

Figure 4.16 – Details of the critical thermocouple features; a) most critical thermocouple slot (inner disk surface); b) most critical thermocouple slot (backside disk surface); c) cob thermocouple slot (inner disk surface); d) hole and slot to fit the cob attachment (back face).

The design modifications concern the geometry of small features, such that the thermal solution is not affected. The temperature field was the same as Figure 4.7.

The reduction of the maximum stress concentration achieved through the design changes is significant, as illustrated in Figure 4.17. The location of maximum stress is the first radial slot in the diaphragm, in particular the narrow section close to the blend. The stress level is reduced to 773 MPa, about 370 MPa less than the initial geometry and within the elastic limit.

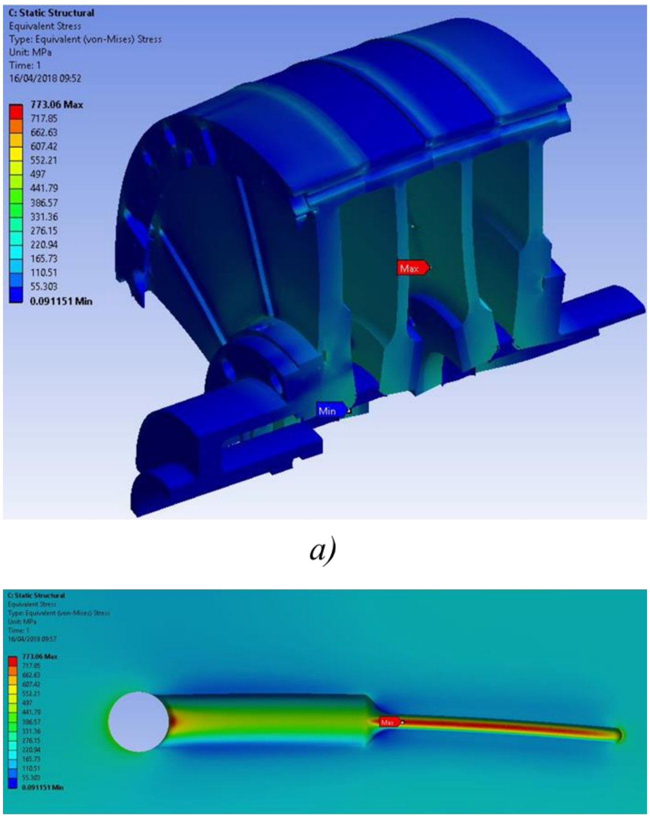

a)

b)

Figure 4.17 - Equivalent stress field (von Mises) after the design modifications; a) whole disk pack sector; b) detail of the highest stress location (thermocouple feature).

All the features at low radius might give concern and must be investigated. They include: slots and holes in cob features, low radius slots and holes in the diaphragm features. Note that these are present on both disks.

Figure 4.18 shows the equivalent stress levels on the features of disk 2; the calculated values are reported on the figure; Figure 4.19 shows the equivalent stress levels on the features of disk 3. The maximum calculated stresses are reported on the figure. The stress decay progressively along the radial direction.

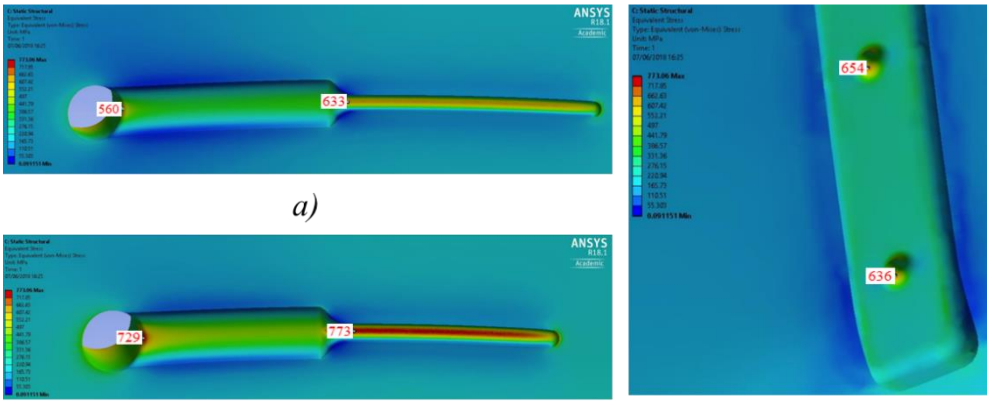

a)

b)

c)

Figure 4.18 – Equivalent stress levels on the thermocouple slots of the diaphragm of disk 2; a) second lowest radius; b) lowest radius; c) backside.

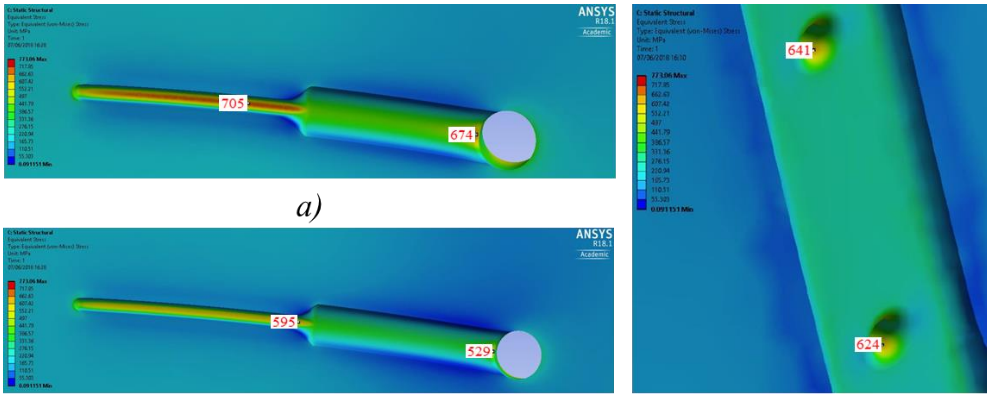

a)

b)

c)

Figure 4.19 – Equivalent stress levels on the thermocouple slots of the diaphragm of disk 3; a) second lowest radius; b) lowest radius; c) backside.

A calculation without the thermal loads was carried out to evaluate the relative levels of stress. The most critical location does not change, the highest value is 605 MPa, meaning that the thermal stress account only for 22% of the total stress. The percentage is not the same everywhere: in the features of Figure 4.19c, e.g., it accounts for 15%.

As regards the cob features, the critical geometries are the thermocouple holes and the cob attachment holes, as highlighted in Figure 4.16c and Figure 4.16d. Calculations were carried out with and without the cob attachments, revealing that the case with the cob attachments leads to higher stresses. The effect of the Surrey inserts is limited, since their stiffness is very low compared to the disks. Figure 4.20 shows the inner and outer faces of disk 3 with cob attachments and Surrey inserts (hidden in the picture). Figure 4.21 shows the inner and outer faces of disk 3 without cob attachments and Surrey inserts. Stress levels are everywhere below the elastic limit. Comments on these values are given in Section 4.5, where the disk pack deformation is discussed.

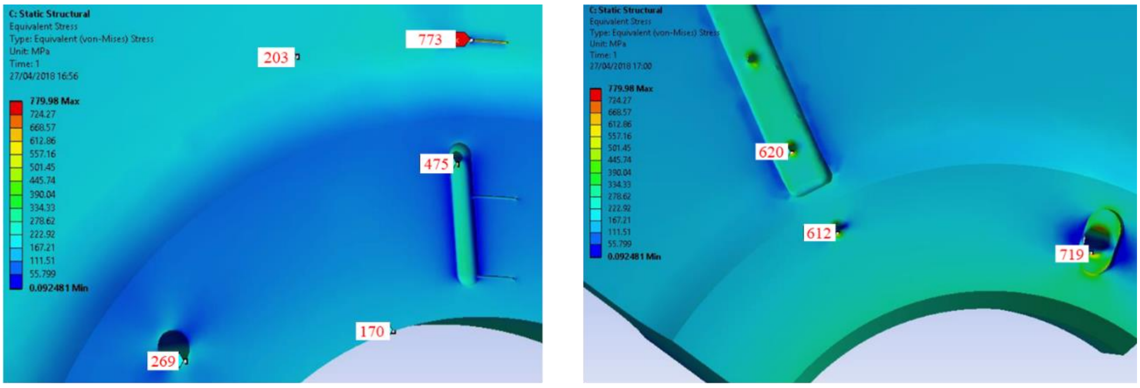

a)

b)

Figure 4.20 – Stress levels of the cob features with cob attachments and Surrey inserts (hidden); a) inner disk face; b) outer disk face.

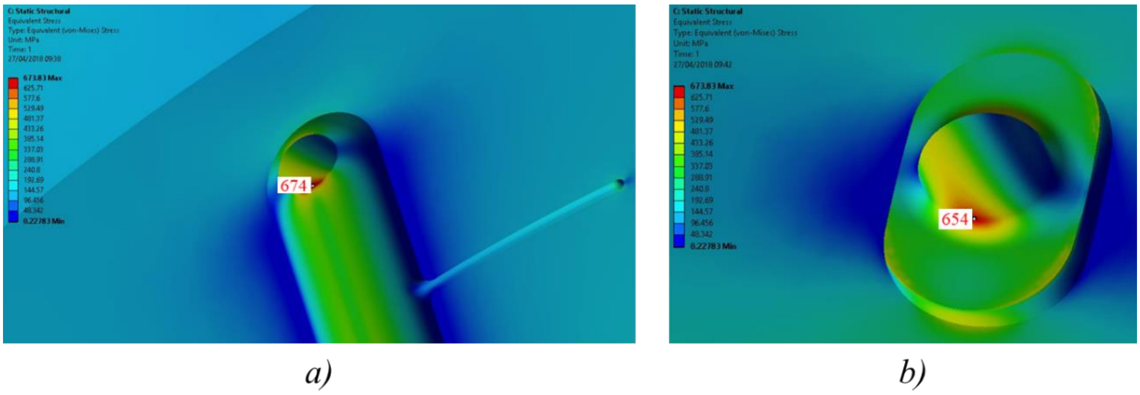

a) b)

Figure 4.21 – Stress levels of the cob features without cob attachments and Surrey inserts; a) inner disk face; b) outer disk face.

4.4.4 Design conclusions

The conclusions of the calculation are as follows:

- there are no locations where the material goes plastic;
- the components with largest stress are the internal disks;
- the location with largest stress (but still elastic deformation) is the first radial thermocouple slot on the diaphragm of disk 2;
- other highly-stressed locations (but still within elastic deformation) are at edges of the low-radius thermocouple slots (on both font and back faces of the diaphragms) and the holes at the cobs.

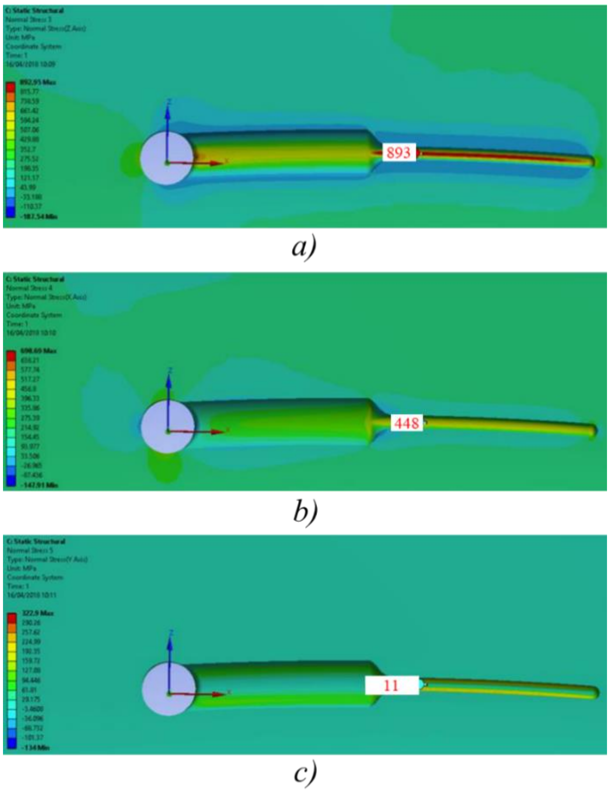

a)

b)

c)

Figure 4.22 – Principal stresses in the most critical location; a) radial; b) tangential (circumferential) direction; c) axial direction.

Importantly, the location of maximum stress experiences an equivalent (von Mises) stress equal to 773 MPa. The principal stresses at this location are radial (maximum), circumferential, and axial (minimum), as reported in Figure 4.22. Their values are respectively 893 MPa, 448 MPa and 11 MPa. As the axial stress is small the material nearby is in plane stress state, which is a normal condition for solid rotating disks (Vullo and Vivio 2013).

4.5 RESULTS DISCUSSION

The aim of this section is to assess the validity of the simulation results by means of basic engineering concepts. With reference to the disk-pack deformation field (Figure 4.11) and the stress levels previously reported, the issues under investigation are as follows:

- how are the disk constraints affecting the deformation field?
- why are the inner disks bending as shown?
- is it possible to estimate the computed stress values using analytical methods?

With regard the first question, the deformation mode should be assessed. The intake and the swan neck (plus the ring-like element) are bolted onto disks 1 and 4 respectively; these are components with low external radius, while the four disks have a 530 mm external diameter. Low-radius components constrain the centrifugal growth of high-radius components they are attached to, bending them. Moreover, the lack of symmetry of the disk shrouds bends the interface with the inner disks outwards. This effect is even more marked in disk 2 and 3 since they have higher temperatures, especially at the shroud. This causes the diaphragms to bulge inwards. The external shrouds surface is instead forced to a dome-shaped profile. The diaphragms of the internal disks bend inwards only at the higher radii, while at the cob radii they bend oppositely. This is discussed below.

4.5.1 Disk bending deformation

To fully understand the deformation of the internal disks, several cases were run, adding and removing components and changing the shape of the cobs (thus varying the distribution of mass). The same conditions described in the previous sections have been applied. All the features have been removed to simplify the meshing and the solution process.

The first set of results shows the axial deformation for three cases (Figure 4.23):

- disk pack without inserts and attachments;
- disk pack without inserts;

- full disk pack.

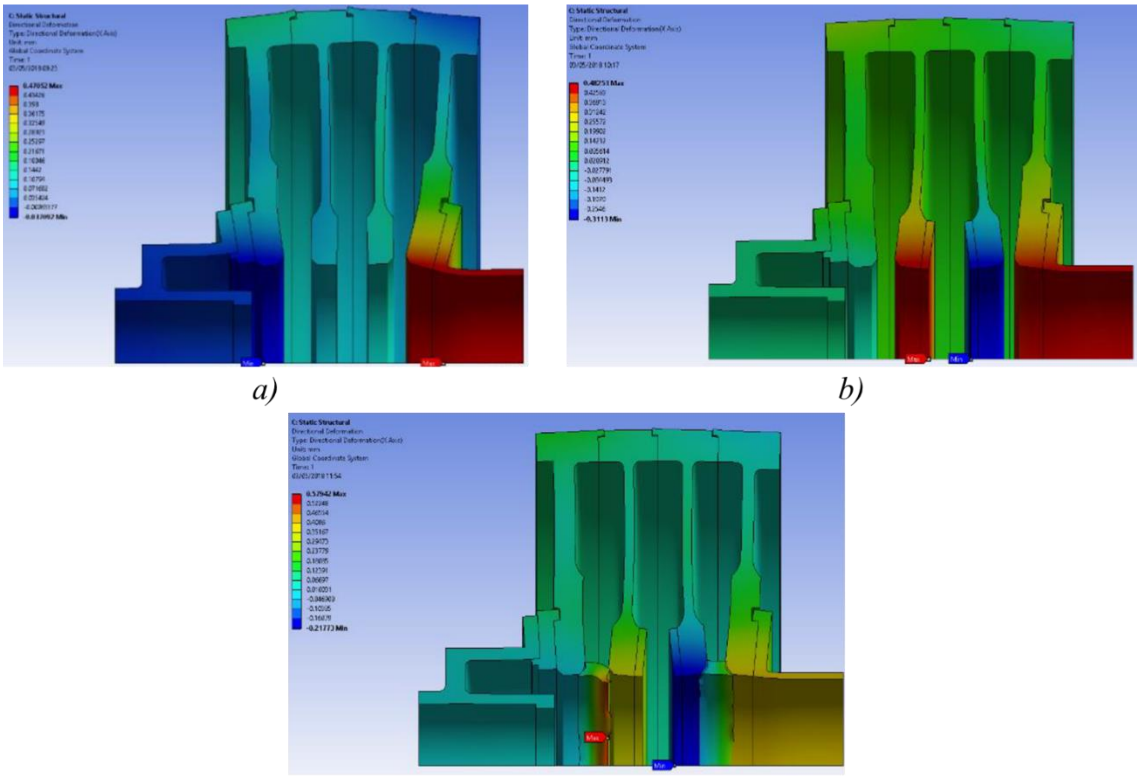

a) b)

c)

Figure 4.23 – Axial deformation fields; a) without cob attachments and Surrey inserts; b) with only cob attachments; c) with cob attachments and Surrey inserts.

The first case (Figure 4.23a) shows a small outward bending, confined at the cob. In the other cases the effect is more intense. The diaphragms are bent more than the cobs. The Surrey inserts behave as soft material spacers taking a large part of the axial deformation since their stiffness is low. They do not make a significant difference in terms of axial displacement of the cobs. The conclusions of these results are as follows:

- every mass asymmetry at low radius bends the disks on the opposite side with respect to where the mass is added;
- the cobs can be considered rings, namely elements whose bending stiffness is very high – thus they oppose to the diaphragm displacement.

To support these conclusions and to investigate further the mechanics, the disk pack was simplified into more basic geometries, and another set of cases was simulated:

- thin cobs disks (Figure 4.24a);
- solid symmetric cobs (Figure 4.24b);
- thin cobs disks with internal attachments (Figure 4.24c);
- thin cobs disks with external attachments (Figure 4.24d).

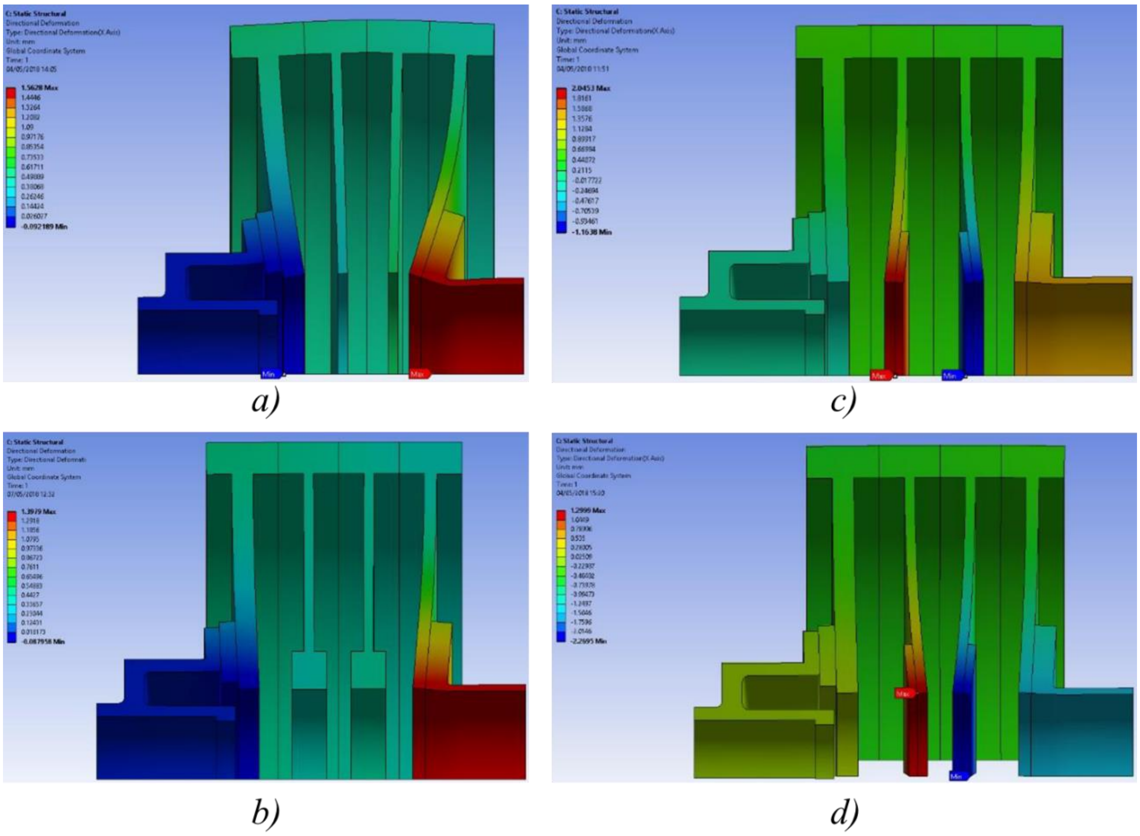

Figure 4.24 – Axial deformation fields on different cases of a simplified disk pack; a) thin disks; b) thick symmetric cobs; c) thin disks with attachments on the inner side; d) thin disks with attachments on the outer side.

The figures refer again to the axial deformation. For cases c) and d), it is readily confirmed that if mass is attached to one side of the disk, it bends to the opposite side. Figure 4.25 shows with simple silhouettes this mechanical behaviour. The black component is a disk, the red is an attachment. The coloured arrows in the left-hand side represent the centrifugal forces to which each component is subjected. The differences in forces create a differential growth but due to the mechanical constraint the components exchange opposite reactions at the common interface, resulting in a bending moment for each.

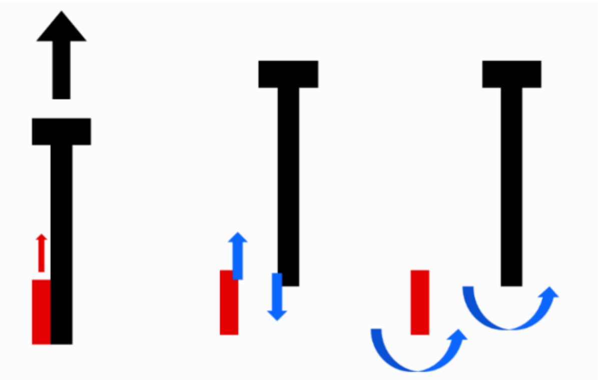

Figure 4.25 – Bending mechanisms of rotating disks (black) constrained at the inner radius by ring-like elements (red).

Figure 4.24a shows the deformation of thin diaphragms. The interfaces at the disk shrouds exert a moment to bend inwards. This effect is marked if the disk thickness is low (a thin plate has low bending stiffness). A thick symmetric cob stiffens the disk bore, leading to a limited deformation (Figure 4.24b). The behaviour is highlighted in Figure 4.26, where the thick cobs have nearly zero rotation.

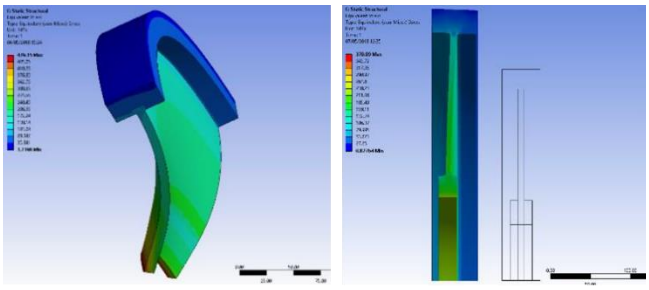
a) b)

Figure 4.26 – Deformed shapes of the simplified disk pack; a) thin disks; b) thick cobs. Deformation fields have the same magnification scale.

The bending analysis qualitatively supports the simulation results. The attachments are principally responsible for the outward bending of the internal disks. The case without inserts and attachments (Figure 4.23a) still exhibits a small outward bending because of the cob asymmetry – the cob external edges are chamfered. The thicker cobs increase the bending stiffness of the disks at low radii and thus the cobs are not compliant in following the diaphragms inwards.

As a secondary effect, the deformation of the disks due to mass asymmetry generates the bowing of the cobs, especially at the bore radius (Figure 4.27). This results in a tension of the outer surface and a compression of the inner surface, which adds to the hoop stress. This explains the difference of equivalent stress in the cob features between the case with cob attachments (Figure 4.20) and the case without (Figure 4.21).

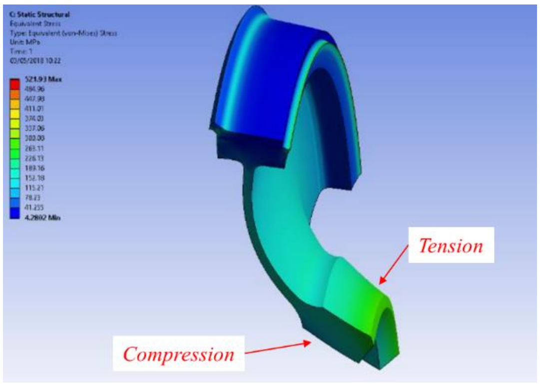

Figure 4.27 – Bowing deformation mode of the cobs (all other components are hidden).

4.5.2 Analysis of the unfeatured disk pack and validation of the stress concentration factors

The calculated stress values are discussed in this section. The rationale is as follows:

- All geometric features to accommodate the thermocouples are removed to calculate the *unfeatured* stress values.
- Retrieve the stress concentration factors for the designed thermocouple slot.
- Apply the stress concentration factors to the *unfeatured* stresses to compare with the *featured* stress values obtained via the numerical calculation.

As a reference value, the highest stress location of a single, rotating, constant-thickness disk is the inner radius, according to the equations (Vullo and Vivio 2013):

$$\sigma_r(r) = \frac{3+\nu}{8}\rho\Omega^2\left(b^2 + a^2 + \frac{b^2a^2}{r^2} - r^2\right) \tag{4.1}$$

$$\sigma_c(r) = \frac{3+\nu}{8}\rho\Omega^2\left(b^2 + a^2 + \frac{b^2a^2}{r^2}\right) - \frac{1+3\nu}{8}\rho\Omega^2 r^2 \tag{4.2}$$

If applied to the analysed case (single disk with same inner and outer radius, rotating at 8,000 rpm with no thermal load), the equivalent stress at the bore is around 200 MPa. Any deviation from this reference is attributed to thermal stress and/or further mechanical stress due to the constraints.

Table 4.2 reports the unfeatured radial and tangential stresses calculated at the same radius of the critical thermocouple slot, for both the inner surface and the outer surface of disk 2.

Table 4.2 – Unfeatured radial and tangential stress in the three analysed cases at the most critical thermocouple location.

		Radial Stress [MPa]	Tangential Stress [MPa]
No cob attachments	*Inner surface*	187	197
No Surrey insert	*Outer surface*	174	194
Cob attachments	*Inner surface*	210	186
No Surrey inserts	*Outer surface*	160	197
Cob attachments	*Inner surface*	221	194
Surrey inserts	*Outer surface*	144	192

The table shows that the tangential stress is modestly affected by the addition of Surrey inserts and cob attachments. The radial stresses between inner and outer faces are instead rather different. However, the mean value between the two faces is always constant. The magnitude of this variation is directly related to the disk bending. The addition of the attachments bends the diaphragms outwards, tensioning the inner surface and compressing the outer. This phenomenon is magnified when the inserts are in place, since they act as a further constraint opposing the free axial displacement of the bore. To some extent, the diaphragm acts like a built-in beam. This effect is limited by the low stiffness of the Surrey inserts (made of Rohacell). A calculation carried out with inserts made of titanium showed much higher values of stress.

Common engineering practice is to retrieve the stress concentration factors from reference technical charts, and then apply them to the unfeatured stress to compare with the numerical results. The thermocouple slot is not a common geometry and there are no standard reference charts.

At first, the stress concentration factor of the actual geometry has been simulated in a test case – different from the actual thermocouple slot – for which a reference chart exists. This assessment was made to check that the simulation is able to pick up the right factor. A test plate with a pair of semi-circular grooves has been simulated (Figure 4.28). An arbitrary normal force pulls the plate, which is cantilevered. With a mesh-independent solution, the computed stress intensity factor is equal to 2.91.

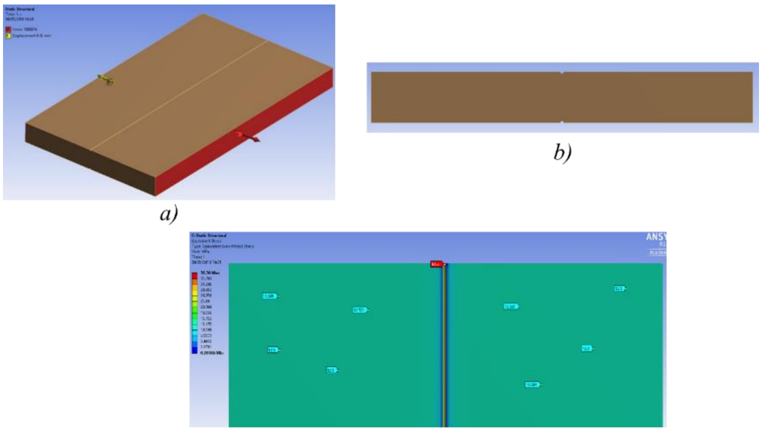
a)

b)

c)

Figure 4.28 – Simulated stress intensity factor test; a) test force pulling the test piece with a round slot; b) cross-section of the test piece; c) equivalent stress with a maximum in the centreline of the feature.

Figure 4.29 reports a technical design chart for the feature of the test plate. Using the same input geometry (r = 0.25 mm, *w* = 8 mm, *r/d* = 0.0333, *w/d* = 1.067), the diagram gives a factor ~3. The numerical calculation is therefore able to predict the correct stress concentration factor.

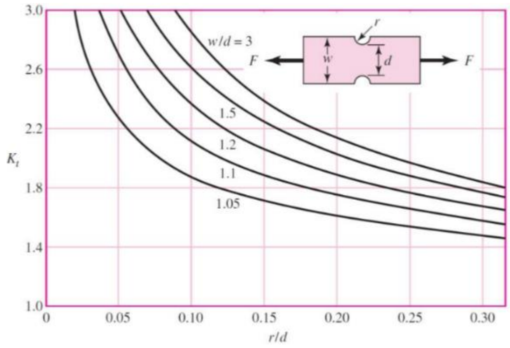

Figure 4.29 – Technical chart of stress concentration factors for a feature equal to the test piece, from Budynas and Nisbett 2010.

The stress concentration factor is strongly dependent on the geometry of the feature (shape and dimensions) and also on the direction of the load. In disks 2 and 3 the radial stress is partly given by the centrifugal load and partly by the bending moment. With reference to the case with cob attachments and Surrey inserts reported in Table 4.2, the radial stress of disk 2 can be divided into a constant centrifugal part equal to the mean of both sides, and an alternated part due to a bending moment, as depicted in Figure 4.30. These two stress components are related to two different stress concentration factors.

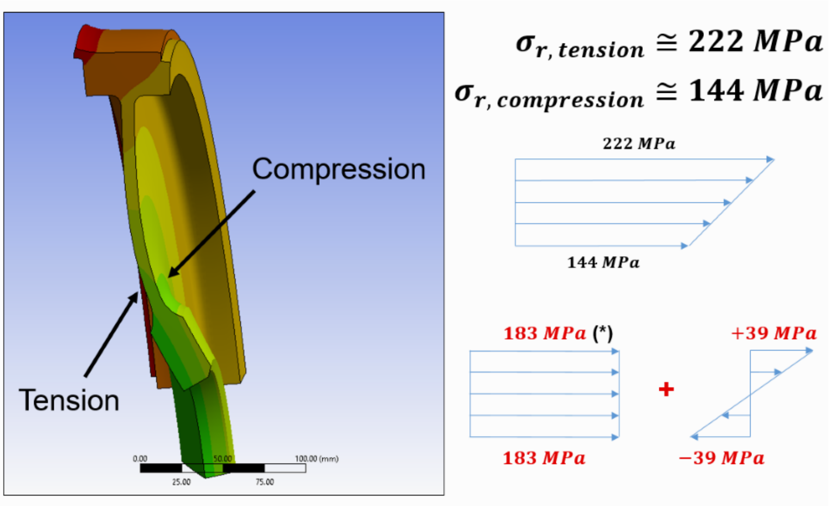

Figure 4.30 – Breakup of the unfeatured radial stress of disk 2. The mean between the two sides is summed to an alternated part due to the bending mode.

The actual geometry of the thermocouple feature was reproduced in a test plate with the same thickness of the diaphragms, tested with a force normal to the groove to simulate the centrifugal force (Figure 4.31a), and a moment to simulate the disk bending (Figure 4.31b).

The computed stress concentration factors are 4.03 for the force normal to the groove ($k_{e,radial}$), 3.77 for the bending moment ($k_{e,bending}$). This means:

$$\sigma_{r,total} \cong k_{e,radial} 183MPa + k_{e,bending} 39MPa \cong 885MPa \tag{4.3}$$

This value matches the principal radial stress of the full simulation of 893 MPa (Figure 4.22a).

When the full slot is reproduced in the test plate and loaded with a force normal to the groove as before, a longitudinal stress – corresponding to the tangential stress on the disk – is generated in the slot (Figure 4.32).

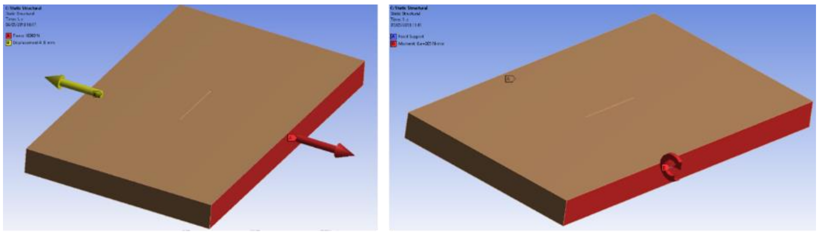
a) b)

Figure 4.31 – Test force (a) and test bending moment (b) to calculate the two stress concentration factors of the thermocouple groove.

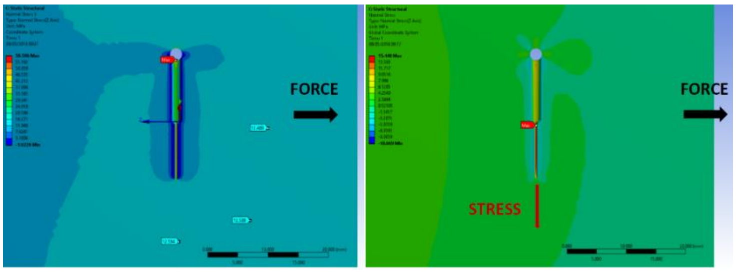

Figure 4.32 – Test piece with full slot reproduction to evaluate the effect of a force normal to the groove (radial on the disk) on the longitudinal stress (tangential on the disk).

Normal forces and moments generate additional circumferential stresses in the slot. The stress concentration factor $k_{e,tangential}$ is equal to 1.24; the ratio between the unfeatured radial stress and the generated circumferential stress. The total tangential stress in the feature is given thus by adding this effect to the the unfeatured tangential stress (equal to 194 MPa, Table 4.2):

$$\sigma_{t,total} \cong 194MPa + k_{e,tangential}\sigma_{r,tension} \cong 468MPa \tag{4.4}$$

This result is close to the full simulation hoop stress, which is 448 MPa (Figure 4.22b).

The method provides close agreement with the full simulation in terms of the radial and the circumferential stresses at the location of maximum stress. This gives confidence to the described physical understanding of the disk behaviour under load and to the quantitative results obtained.

4.6 REFINEMENT OF BOUNDARY CONDITIONS AND RESULTS

The thermal boundary conditions applied in Section 4.2.1 represent a first guess approach to the worst-case-scenario for the radial temperature gradients, and consequently for the thermal stress. They derive from conservative assumptions such as the imposition of the ambient temperature at the disk bore – constituting a worst-case scenario. Since the temperature distribution is unknown until experiments are run, a refinement of the boundary conditions might highlight the sensitivity of the stress results with respect to errors. For the calculations presented in this section, the mesh used in the thermal model was also refined.

4.6.1 Thermal analysis

Figure 4.33 shows the refined boundaries which are believed to be representative of the experiments. No surface-temperature conditions are applied to the disks, only heat transfer coefficients. Again, their values are taken from the theoretical predictions in Tang et al. 2018 and applied along the inner shroud (orange), the radial inner surface (black) and the cobs (light green). The radiant heaters are modelled as a constant heat flux at the external shroud of the inner disks. The already mentioned convection correlation for a rotating cylinder as reported in Dorfman 1963 has been extended to the swan neck and the intake. A fixed temperature of 20°C is set at the spline location of the swan neck to model the shaft (considered at the ambient fixed temperature). The external temperature is fixed at 20°C.

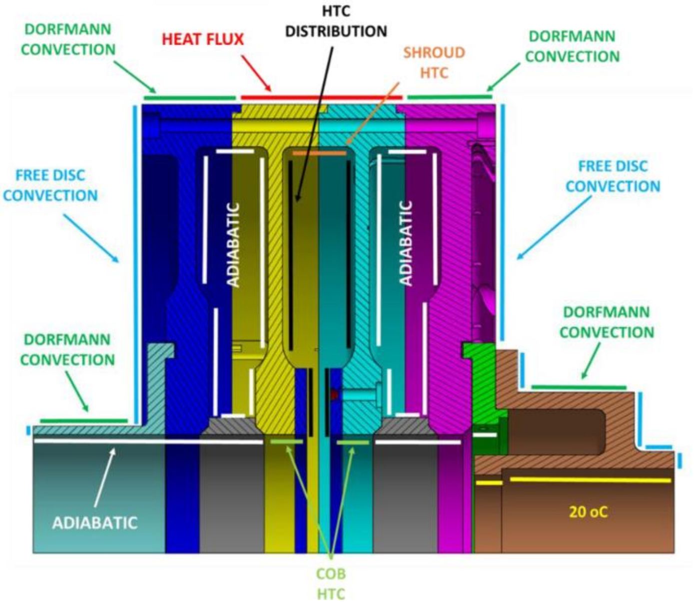

Figure 4.33 – Refined thermal boundary conditions

A fine mesh was used, resulting in 1.64 million elements (Figure 4.34).

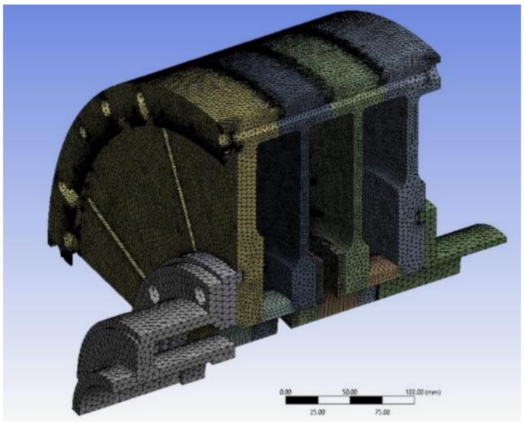

Figure 4.34 – Fine mesh used for the refined thermal boundary conditions.

The results are shown in Figure 4.35. The input heat flux was chosen so to obtain 100°C at the inner shroud of disks 2 and 3. The heat flux is 12.7 kW/m^2, which results in about 2 kW power. This values informs the selection of the rating of the radiant heaters. The cob temperature rise is less than 10 °C and the isotherms show a smoother decay compared to the previous solution (Figure 4.35).

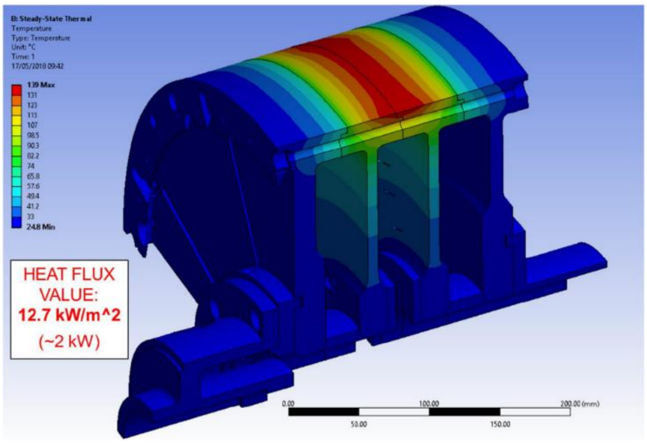

Figure 4.35 – Temperature field on the disk pack with refined thermal boundaries. The heat flux value results in about 2 kW.

4.6.2 Thermo-mechanical analysis

The updated thermo-mechanical simulation was carried out with the refined thermal load. All other boundary and load conditions are the same as those described in Section 4.3.1. The deformation and the equivalent stress field presents the same features discussed previously, as reported in Figure 4.36.

The location of maximum stress is the first radial feature in the diaphragm of disk 2, with the equivalent (von Mises) stress of 703 MPa. Removing the thermal load, the value drops to ~600 MPa, which is consistent to the previous simulation. The detail of the equivalent and principal stresses at the slot location is illustrated in Figure 4.37. The location is again in a state of plane stress.

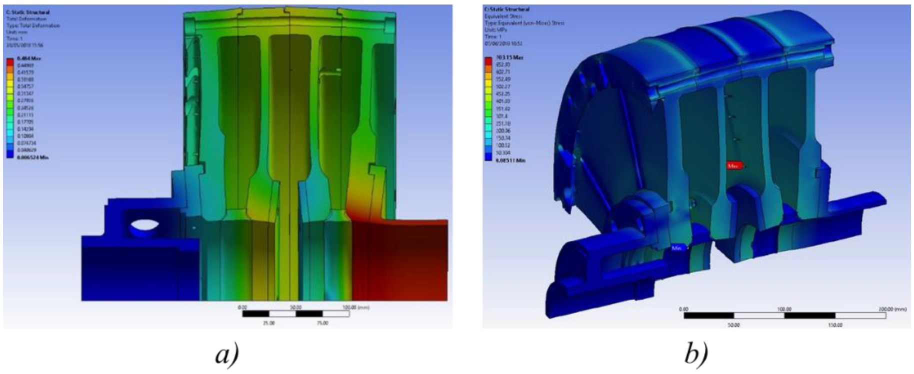
a) b)

Figure 4.36 – Results of the thermo-mechanical calculation; a) deformation field; b) equivalent (von Mises) stress. The most critical location is the same.

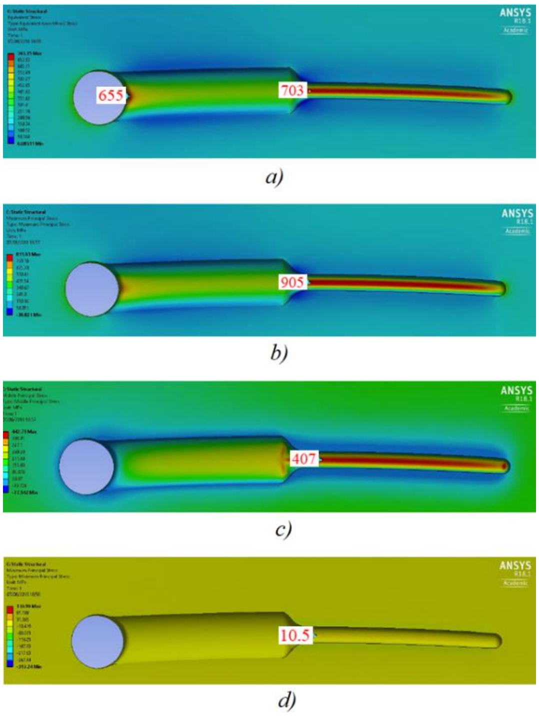

a) b) c) d)

Figure 4.37 – Stresses in the most critical thermocouple feature; a) equivalent (von Mises); b) radial; c) tangential; d) axial.

The other features at low radius such as other thermocouple slots (on the diaphragm and the cob) or features to fix the cob attachments have been investigated. With few exceptions, the calculated equivalent stresses are below 600 MPa.

4.6.3 Effect of radial interference

The radial interference was investigated to assess the effects on the highest stress and if combination of the static fit and the differential growth of the disks results in acceptable values for the spigots. It was found that:

- the most critical location (i.e. lowest-radius thermocouple feature on the diaphragm) is affected in a negligible way;
- The spigot stresses are well below the yield strength of the material (280 MPa at the interface between disk 3 and 4, considering a 0.2 mm tool tip radius at the spigot).

The radial interference has been specified 0.05 mm in the final design.

4.7 RIG DESIGN VALIDATION

This section applies classic failure criteria in terms of the static, fatigue and crack propagation to the critical locations of the design. The static-safety analysis is carried out through the maximum distortion energy criterion (Hencky-Huber-von Mises); the fatigue analysis through the Basquin approximation of the S-N curve (sometimes referred to as Wöhler curve) and then the Soderberg line method; the crack propagation analysis through the integration of the Paris law for the basic surface crack case.

4.7.1 Static safety factor

Referring to Table 4.1, the chosen material has a yield strength of 889 MPa. To assess the static safety through the expressed criterion it is sufficient to compare this value to the maximum equivalent stress obtained from the simulation (~700 MPa). *This leads to a static safety factor = 1.26.*

4.7.2 Fatigue safety factor

According to the specification, the rig requirement is to withstand 10,000 cycles at full thermal and mechanical load. This is simulated in a fatigue cycle shown in Figure 4.38. Both the mean and the alternated stresses are equal to half of the cycle maximum stress. The unfeatured equivalent stress has to be considered as cycle maximum value.

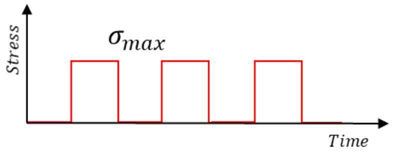

Figure 4.38 – Load cycle assumed for the fatigue analysis.

The fatigue criterion adopted is the Soderberg line: it is the most conservative compared to the others and it is analytically simple. It consists in retrieving the fatigue safety factor X_f from the following equation:

$$\frac{k\sigma_{a,unf}}{b''\sigma_N} + \frac{\sigma_{m,unf}}{\sigma_y} = \frac{1}{X_f} \tag{4.5}$$

where the product $k\sigma_{a,unf}$ is the featured alternated value, σ_N is the fatigue strength at N = 10^4 cycles, $\sigma_{m,unf}$ is the unfeatured mean stress, σ_y is the yield strength of the material, b'' is a coefficient to take into account the surface state (a rough surface is more likely to start a crack, reducing the actual fatigue life). Both mean and alternated stresses are considered equivalent stresses: in other words, the S-N curve and the fatigue criteria are here considered valid for the plane stress state if the von Mises stresses are considered. Other assumptions in Juvinall and Marshek 2011 are possible, but they do not significantly alter the outcome of the present study.

The Basquin approximation of the fatigue behaviour of the material consists in drawing a straight line from two points of the S-N curve: the first defined by 90% of the ultimate tensile strength on the stress axis and 10^3 on the cycle number axis, the second defined by the fatigue limit. Before and after this line, there are straight lines approximating the low cycle fatigue (left) and the fatigue limit (right). The fatigue strength at 10^6 cycles is assumed as fatigue limit, and from the open source material data can be set at 510 MPa (Figure 4.39). From the curve, the fatigue strength at the required 10^4 cycles is equal to 719 MPa. Once the disks were manufactured, four fatigue samples were machined from the scraps and tested via rotating bending. All the samples passed the test, confirming that a fatigue strength equal to 719 MPa represents a good assumption.

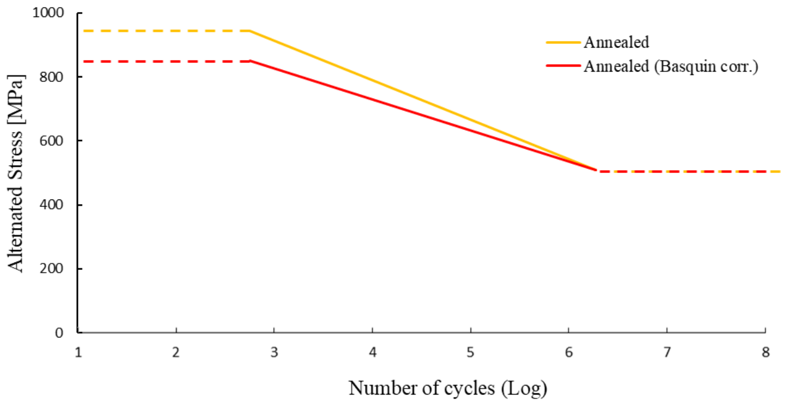

Figure 4.39 – S-N curve of the material used with the Basquin approximation. The orange line refers to annealed Ti6Al4V (as the one supplied); the red line is the Basquin correction used to estimate the fatigue strength at 10^3 cycles.

At the slot location, the unfeatured equivalent stress is given by inner surface radial and tangential components reported in Table 4.2:

$$\sigma_{eq,unf} = \sqrt{\sigma_{r,unf}^2 + \sigma_{t,unf}^2 - \sigma_{r,unf}\sigma_{t,unf}} \cong 209\ MPa \tag{4.6}$$

This results in a mean unfeatured stress equal to 105 MPa. From Figure 4.37a the featured equivalent stress is about 700 MPa, thus resulting in a featured alternated stress of 350 MPa. In this approach the unfeatured stress values are taken from Table 4.2, which, strictly speaking, is obtained with the conservative thermal boundaries. Although less accurate, this is a conservative assumption on the mean stress. The value b'' is chosen to equal 0.8, in agreement with Budynas and Nisbett 2010. *Solving equation (4.5), the criterion gives a fatigue safety factor equal to 1.37.* The Soderberg diagram is shown in Figure 4.40, where the dashed line takes into account the factor b''; the safety factor is thus identified with the distance from the working point to this line.

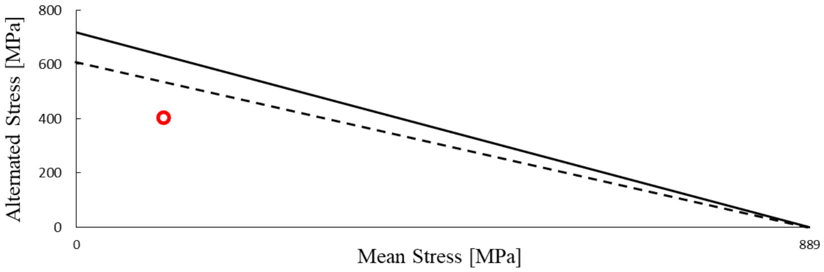

Figure 4.40 – Soderberg diagram of the fatigue analysis. The red circle represent the working conditions of the most critical point; the dashed line marks the b'' factor correction.

4.7.3 Crack propagation analysis

The crack-propagation analysis is carried out through the concept of fracture toughness. Two reference values are considered: Ti-6Al-4V (Grade 5) STA and Ti-6Al-4V (Grade 5) Annealed (at 700-785 °C). The alloy supplied for the present application is annealed. Annealing increases the ductility of the alloy, protecting it from brittle fracture at the expense of the yield and ultimate tensile strength. The fracture toughness depends on the material, the working process and the metallurgical treatment; for titanium alloys it is 42.9 MPa$^{0.5}$ for the standard and 74.6 MPa$^{0.5}$ for the annealed (BSI 2017). According to the supplier, the material used was annealed up to 750 °C.

To compute the failure crack size, the following equation is used:

$$a_f = \frac{1}{\pi}\left(\frac{K_{IC}}{Y\sigma_{eq,unf}}\right)^2 \tag{4.7}$$

where K_{IC} is the fracture toughness, Y is a shape factor (ideally 1.12 for surface cracks) and $\sigma_{eq,unf}$ is the unfeatured equivalent stress. At the location of maximum stress (thermocouple slot, $\sigma_{eq,unf} = 211\ MPa$) the computed value is 31.8 mm, while at the disk inner radius ($\sigma_{eq,unf}$ = 290 MPa or less) and the value is 16.8 mm. These calculations should be compared with the minimum detectable crack size. According to SAE International 1972, the minimum detectable size with ultrasonic inspection is 1.2 mm. This is an appropriate reference value for the cob, while for the thermocouple slot an additional 0.5 mm due to the slot geometry itself should be considered, leading to 1.8 mm as a reference. In both cases, the computed failure crack size is larger than the minimum detectable. In a worst-case analysis, these values are assumed as initial pre-existing crack sizes.

The integration of the Paris equation allows computing the number of cycles before a given initial crack reaches the failure size previously estimated. The finite resulting equation is:

$$N_f = \frac{a_f^{1-n_{crack}/2} - a_0^{1-n_{crack}/2}}{\left(1-\frac{n_{crack}}{2}\right) C_{crack} \left(Y \Delta\sigma \sqrt{\pi}\right)^{n_{crack}}} \tag{4.8}$$

where a_0 is the initial crack length, n_{crack} and C_{crack} are material properties (equal to 2.2 and 6×10^{-10} m respectively, Wang et al. 2014), Y is the aforementioned shape factor (1.12) and $\Delta\sigma$ is the cycle stress range (*i.e.* the difference between the unfeatured maximum and the unfeatured minimum stresses values for the cycle). At the thermocouple slot location, the stress range is 211 MPa (zero minimum fatigue cycle), the initial crack size is 1.8 mm; this results in a life of ~13,300 cycles for the annealed alloy. At the disk bore, the stress is 290 MPa with an initial crack size of 1.2 mm, resulting in a life of ~6,400 cycles for the annealed alloy.

Although the models here used are relatively old (1950s) and not exhaustive, they are reliable and ready to use; Keller 2015 shows the application of same methodology for gas turbine rotor disks analysis.

4.8 OUTCOMES OF THE THERMO-MECHANICAL ANALYSIS

The calculations presented in this Chapter show that the design successfully meets the requirements of life and safety. Some concluding remarks are added here.

The loads and boundary conditions are representative of the rig tests, while the calculation assessment has provided insight into the disk deformation, following a comprehensive assessment of the rig behaviour. Calculations from an initial design led to an improved design, which has been shown to be successful in terms of stress limit and acceptable life. Under the maximum expected load, there are no locations where the disk material is stressed above the elastic limit.

The maximum stresses (static and fatigue failure) in the disk pack are located at the first two thermocouple slots on the disk diaphragms (especially on disk 2) and on all the features in the cob. Of critical importance, the equivalent stress values at these locations are always below the yield strength of the disk material, with a static safety factor of at least 1.26 and a fatigue safety factor of at least 1.37, meaning that the fatigue safety is slightly less demanding than the static. This result is not surprising, since the required number of cycles (10^4) is at the border of the so-called high cycle fatigue region, where fatigue safety starts to take over static. Of further importance, the fatigue model and the mean stress values are both conservative. The maximum stress levels have been compared favourably to an engineering study for an unfeatured disk pack and a stress-concentration-factor study. This provides further confidence on the reliability of the solution.

It was shown that a successful standard ultrasonic test allows pre-existing cracks which do not raise concerns with regards the static failure. Surface cracks on the disk bore and on the features were not visually detected. Starting from raw material, the disks were bored out via a slow wire erosion process to prevent inner cracks in the material nearby. The disk features were manufactured with conventional techniques at low speed for the same purpose. Additional comments are stated here. First, for the sake of simplicity, the crack analysis only deals with the case of ideal surface cracks, not subsurface cracks of differently shapes. Secondly, there is always uncertainty in the material parameters characterizing the crack-propagation behaviour and in how ambient and working conditions affect these parameters. The analysed cases take into account surface cracks oriented normally with respect the material surface and located *exactly* in the locations of maximum stress – this event is unlikely and there is a very small associated risk. In conclusion, there is no reasonable concern regarding crack propagation.

With regards the disk-shroud fittings, the simulations are based on interference fits equal to 0.05 mm. Additional simulations showed that the removal of the interferences is slightly beneficial to the rig life, but no concern arise from the designed values.

Finally, the operating conditions of the rig will not always be at full speed (8,000 rpm) with maximum heating – consequently this will result in an increased safety factor and expected life. The stress and fatigue analysis presented in this chapter were reviewed by Rolls-Royce and considered appropriate.

Chapter 5

Design, commissioning and testing of the Bath Compressor-Cavity rig

This Chapter originates from the paper:

Luberti, D., Patinios, M., Jackson, R. W., Tang, H., Pountney, O. J., Scobie, J. A., Sangan, C. M., Owen, J. M. and Lock, G. D., 2021. *Design and Testing of a Rig to Investigate Buoyancy-Induced Heat Transfer in Aero-Engine Compressor Rotors. Journal of Engineering for Gas Turbines and Power,* Vol. 143(4): 041030 (11pages). https://doi.org/10.1115/1.4048601.

It presents and critically discusses the design of the Bath Compressor-Cavity rig, whose aim is to investigate the heat transfer and the fluid dynamics – which are coupled – in a HPC compressor cavity in a number of experimental conditions.

As introduced in Chapter 4, the test section includes four rotating disks enclosing three cavities. Two disks in the central cavity are instrumented with thermocouples to provide the radial distribution of temperature; the two outer cavities are thermally insulated to create appropriate boundary conditions for the heat transfer analysis. An axial through-flow of air is supplied between a stationary shaft and the bore of the disks. The geometry of the test cavity can be changed by fitting attachments, including a pair that create a closed cavity. Two independently controlled radiant heaters allow also differential shroud temperatures for the upstream and downstream disks.

The commissioning of the rig – i.e. the set of gathered data confirming that the rig perform and can be operated according to the requirements – is documented by measurements of maximum vibration at the shaft bearings and by measurement of the disk and through-flow temperatures for some cases.

5.1 INTRODUCTION

Figure 5.1 is a conceptual illustration of an HPC featuring a stack of co-rotating disks and cavities. The primary flow of air through the outer annulus is compressed through blades and vanes and heat is transferred to the shrouds of the cavities. Secondary air extracted from upstream stages creates (in the steady-state) a relatively cool axial through-flow in the annular gap between the disk cobs and the shaft. Buoyancy-induced flow occurs inside the open rotating cavities formed by the co-rotating disks and shroud, with an exchange of enthalpy and momentum between the through-flow and the air inside the cavity. The flow can be broadly divided into two convection regions. The non-dimensional parameters involved with their analytical definitions has been presented in Section 2.3.4 of Chapter 2, and are here briefly recalled. The axial through-flow has a strong influence in the region near the cobs, and the size of this region is governed by the Rossby Number (Ro), which is proportional to the ratio between Re_z and Re_ϕ. Typically, Ro < 1 under engine conditions. The outer convection region is governed by buoyancy. The buoyant effect can be quantified in non-dimensional terms by the Grashof number (Gr), which combines the contribution of rotation and temperature difference, being proportional to Re_ϕ and to $\beta\Delta T$. At engine conditions, Gr is expected in the order of 10^{13}. The set of non-dimensional parameters is completed by the buoyancy number (Bo), which is the ratio of buoyancy to Coriolis forces and useful in determining the relative dominance of forced to free convection in the cavity.

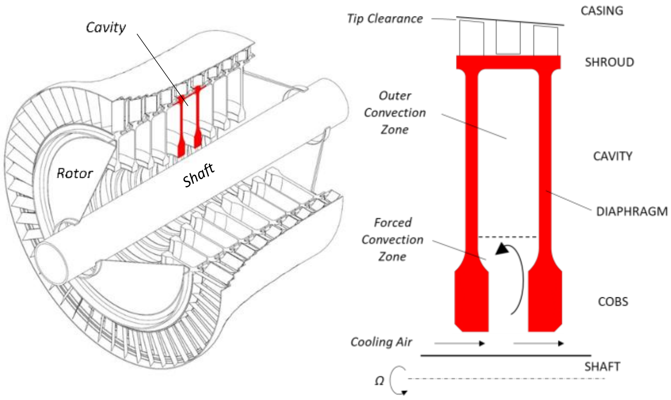

Figure 5.1 - Typical aero-engine HPC (left) with a 2D sketch of the rotating cavity (right) illustrating two convection regions.

Buoyancy-induced flow, which is intrinsically three-dimensional and unstable, presents a challenge for computational fluid dynamics, since achieving accurate results can be prohibitive due to the high computational effort (LES and DNS). With reference to Figure 5.1, the experimental rig has to replicate physically the geometry and the working conditions of a HPC cavity and provide meaningful measurements of temperature and heat transfer along the cavity walls. The design was influenced by the requirement to install the instrumentation and route the cabling in such a way to retain integrity under stress during rig operation.

5.2 DESIGN OF THE RIG

The Bath Compressor-Cavity Rig includes many of the features found in the Sussex rig described in Chapter 2. However, it is a three-cavity rig, where disk and shroud temperatures are measured only in the central cavity; the surfaces of the outer cavities are thermally insulated to make sure that there is no axial gradient across the disk. This is an important design feature directly supporting the use of the fin model (Tang et al. 2015), which implicitly assumes there are no axial temperature differences within the disk; the zero axial temperature gradient is equivalent to a symmetry axis on the insulated surface. The rig includes other features not found in (or not reported for) the rigs described in Section 2. The shroud can be differentially heated to produce temperature differences between the upstream and downstream disks, as found in operating compressors. In addition, measurements of temperature can be obtained on both upstream and downstream disks simultaneously.

The cob geometry can be readily changed, and the axial through-flow can be heated to produce negative values of $\beta \Delta T$, which could be used to determine when stratified flow occurs inside the cavity. In these cases, or when buoyancy effects are weak, radiation between the internal surfaces of the cavity can be significant. So that any radiant heat transfer can be accurately calculated, these surfaces are painted with matt black paint.

Careful consideration was also given to the analysis of the data and to the estimation of the uncertainties in the calculated Nusselt numbers. As this is an inverse problem, in which small uncertainties in the temperature measurement lead to very large uncertainties in the calculated heat fluxes, a Bayesian statistical model was used to calculate the fluxes; details of this are given in Chapter 6. As buoyancy-induced flow is a conjugate problem, in which the conduction in the disks is coupled to convection in the air inside the cavity, the Bayesian model was used in conjunction with a one-dimensional circular fin equation for the conduction solution. This model not only provides an estimate of the radial distribution of the Nusselt numbers, it also provides the 95% confidence interval for these estimates and the associated standard deviation for the radial distribution of the temperature measurements themselves. These uncertainties are dependent on the number of thermocouples used to measure the radial distribution of disk temperature – 28 were used on each disk in the rig – and the Bayesian estimates of the uncertainties in the temperature distribution is more meaningful than the estimated uncertainty of an individual thermocouple.

Figure 5.2 is a cross-sectional view of the Bath Compressor-Cavity Rig, which was designed and constructed in partnership with Torquemeters Ltd. (Northampton, UK). The rotating and stationary components are marked red and blue, respectively. The rotating shaft spins the disk pack through a spline. The drive unit features a supercritical design, meaning that the maximum rotational speed by design is higher than the first resonance speed of the rotor shaft assembly. The shaft is supported by two bearings contained within a sleeve, itself located within an external casing and frame. The radial movement of the shaft is dampened by four springs at the disk end, located between the casing and the bearing sleeve. The downstream end (right-hand side) of the shaft is equipped with a telemetry unit supplied by Datatel Telemetry (Langenhagen, Germany). Owing to the high rotational speed of the disks, slip rings for the measurement wires would result in a considerable wear and consequent high replacement rate. The telemetry makes the wires longer and harder to handle during installation, but does not have to be replaced. At the left-hand side, a stationary shaft is located within a bracket, while the rotating shaft is supported by a small bearing.

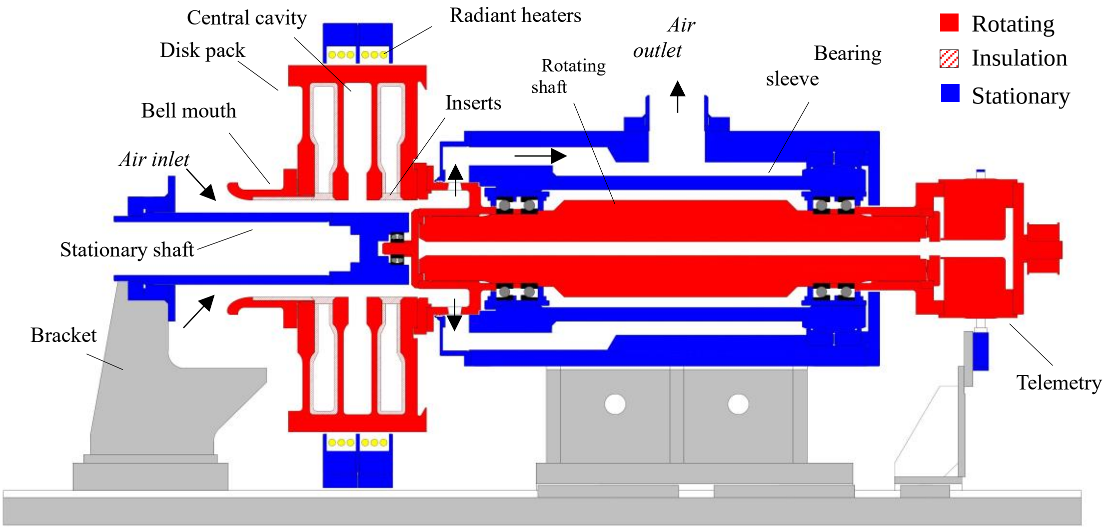

Figure 5.2 - Compressor-cavity rig at the University of Bath.

Tang et al. 2018 noted that the rotational speed of the central shaft appeared to have no significant effect on the heat transfer from the disks in the Sussex multi-cavity rig. This observation is consistent with Long and Childs 2007 and with Long et al. 2003, who saw no significant effect of the shaft rotation on the heat transfer from the shroud in their experiments. For this reason, a stationary shaft was used in the Bath Compressor-Cavity Rig.

The air flow is left to right, entering the rig through an aluminium bell-mouth inlet and creating an axial through-flow in the annular gap between the disk cobs and the stationary central shaft. By means of an extraction unit, the air passes through the driveshaft assembly via radial holes; a labyrinth seal reduces leakage/ingress to < 1% of the through-flow rate. Calculation was made by measuring the pressure drop across the seal during the rig commissioning and using a seal model provided by Rolls-Royce. For conservativism, the cold-built clearance was assumed in the calculation (0.03 mm).

An isometric view of the rig is shown in Figure 5.3 with the air inlet, disk pack, drive-shaft assembly and air outlet to the extractor shown. The disk drum and a belt drive system are positioned at opposite ends of a rotating shaft, which is driven by a three-phase 30 kW motor up to shaft speeds of 8,000 rpm. The through-flow is set by a variable speed Becker (SV300/1, 7.5 kW) extraction unit for mass flow rates up to 0.15 kg/s, measured by a Bronkhorst thermal flowmeter to within ±0.0005 kg/s. The through-flow can be heated to investigate cases with negative values of Gr, which can occur during engine accelerations and decelerations when this through-flow is hotter than the shroud.

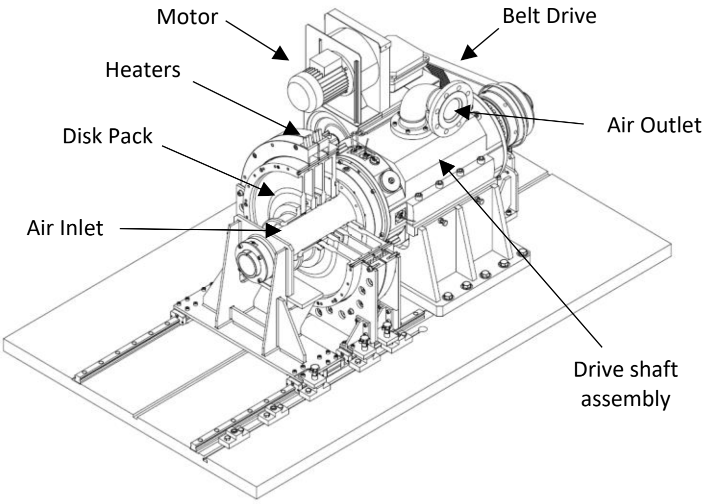

Figure 5.3 – Overview of the Bath Compressor-Cavity rig.

In the test section of the rig, four bolted titanium (Ti-6Al-4V) disks enclose three cavities: upstream, central and downstream. The two central disks are instrumented with thermocouples and heat flux-gauges for measurements in the central cavity. The back surfaces of these disks, in the upstream and downstream cavities, were insulated with Rohacell, a low-conductivity machinable foam (thermal conductivity 0.03 W/mK); the insulation was bonded to the titanium surfaces using Loctite EA9794. For the tests reported here, enthalpy and momentum exchange to the upstream and downstream cavities is prevented by modular, Rohacell inserts; these were held in place and located by a spigot. The shroud is heated by two sets of circumferential radiant heaters (2 kW each); these can be independently controlled and allow differential shroud temperatures for the central disks. Typical under-shroud temperatures are 100 ˚C; this temperature is limited by the thermal properties of the thermal insulation and the allowable stress in the rotating disks.

Figure 5.4 shows the current operating limits of the Bath Compressor-Cavity Rig in terms of Gr, $\beta\Delta T$, Ro and Re_z. The boundaries are determined by the maximum rotational speed (fundamentally limited by the stresses in the disks), the maximum operating temperature of the insulating materials, and the limitation on the through-flow rate. The rig is designed to capture engine-representative data with $10^{10} < \mathrm{Gr} < 10^{12}$. The lower value (which corresponds to the lowest feasible rotational speed of 800 rpm) is useful for computational fluid dynamics computations when large eddy simulation is used.

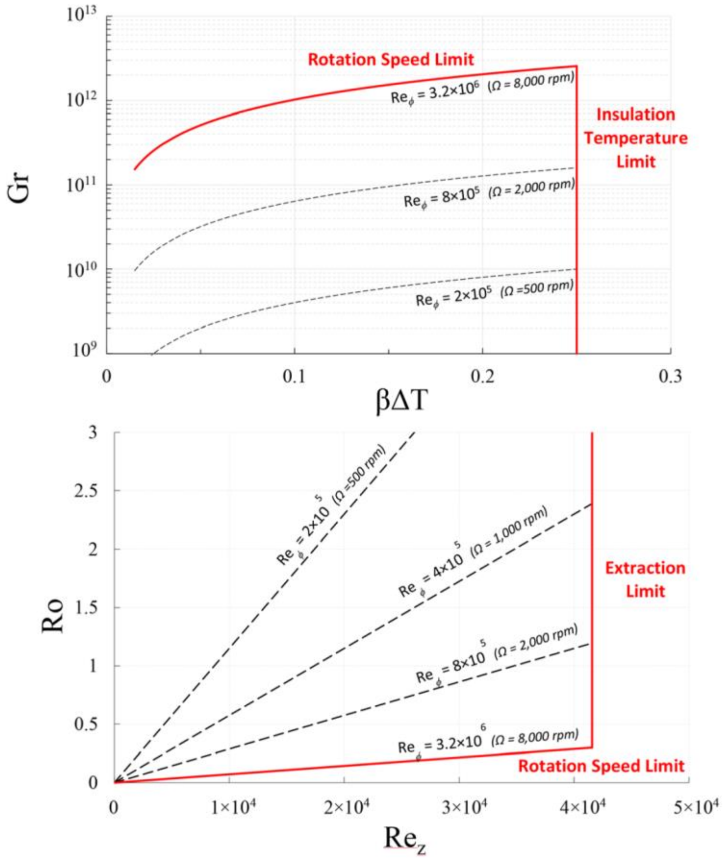

Figure 5.4 - Buoyancy-Induced Flow rig operating limits: Grashof number and buoyancy parameter (top); Rossby number and axial through-flow Reynolds number (bottom).

Modularity and flexibility have been addressed by the design of the rig. A rail system allows movement of the disk pack relative to the drive unit and access to the test section. Separate aluminium attachments can be fitted to the cobs of both central disks; the attachments reduce the axial gap between the cobs – reducing the gap to zero creates a closed cavity, which exists in some compressor designs. Figure 5.5 illustrates the three cob geometries that can be tested and defines the principal dimensions of the test section.

Symbols are further defined in the nomenclature. Rig geometric details and operating parameters are summarized in Table 5.1.

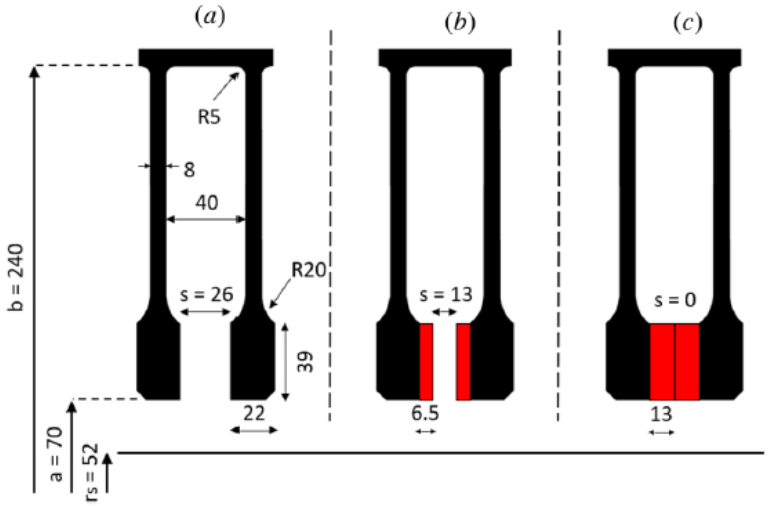

Figure 5.5 - Geometrical dimensions of the cavity and possible cob configurations (dimensions in mm).

Table 5.1 - Rig geometrical and operating parameters.

Shroud radius	b [mm]	240
Cavity ratio	a/b	0.29
Shaft radius ratio	r_s/a	0.74
Gap ratio	s/b	0 – 0.11
Rotational speed	Ω [rpm]	800 – 8,000
Mass flow rate	$\dot{m}$ [kg/s]	0 – 0.15
Shroud temperature (max)	$T_{b,max}$ [°C]	105
Rotational Reynolds number (max)	$\mathrm{Re}_{\phi,max}$	3.2×10^6
Axial Reynolds number (max)	$\mathrm{Re}_{z,max}$	1.2×10^5
Rossby number	Ro	0.1 – 3.4
Buoyancy parameter (max)	$\beta\Delta T_{max}$	0.25
Grashof number (max)	Gr_{max}	2.6×10^{12}

5.3 INSTRUMENTATION

This section first describes the use of thermocouples on the rotating disks, including methods to minimize thermal disturbance. The routing of the instrumentation to the telemetry unit is also discussed. In the stationary frame of reference, the temperature of the through-flow air is measured using thermocouples in rakes upstream and downstream of the central cavity.

5.3.1 Rotating instrumentation

A cross-section of the test section (for no cob attachments) and the instrumentation on the disks is shown in Figure 5.6. Note that the four disks in the co-rotating stack are listed disk 1-4 in the downstream direction, with disks 2 and 3 forming the central cavity. Both disks feature a radial distribution of 28 thermocouples across the cob and diaphragm regions. The radii and relative circumferential locations of the measurements are further illustrated in Figure 5.7. The thermocouples were made in-house from a single AWG36 (0.13 mm diameter) batch of K-type thermocouple wire pairs (Omega GG-KI-36-SLE). The ends of the wires were welded using a SR80 universal welder to form a bead with a diameter < 0.4 mm.

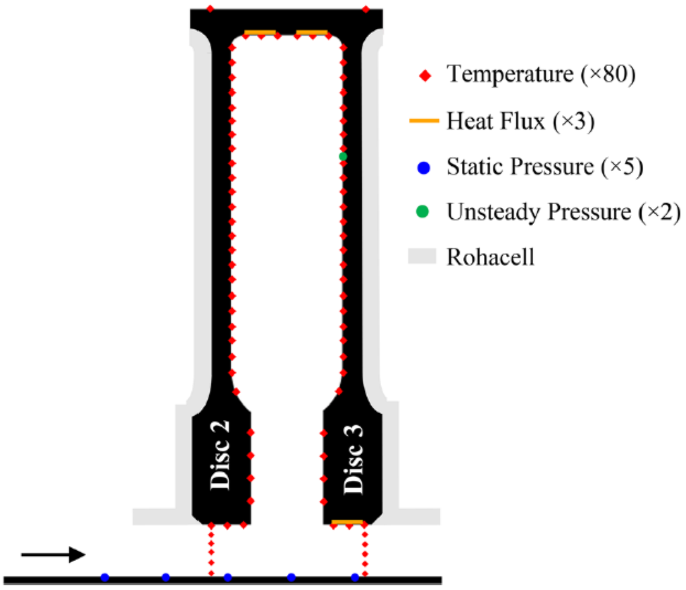

Figure 5.6 – Overview of cavity instrumentation.

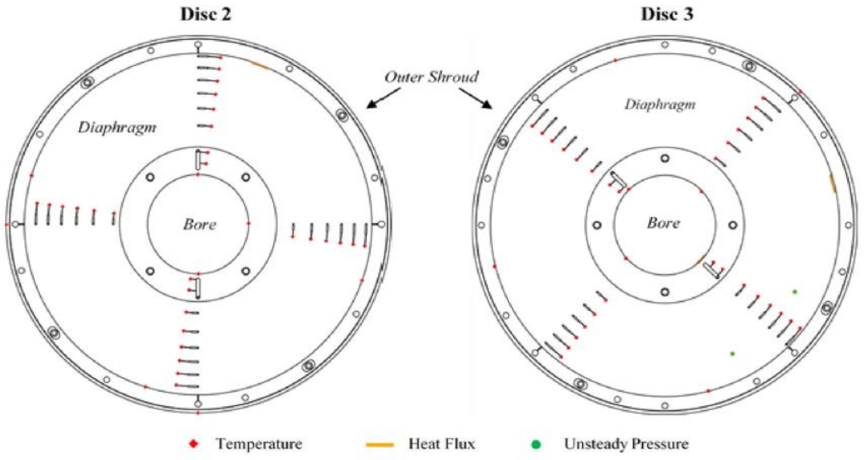

Figure 5.7 – Instrumentation locations on the disk faces.

Figure 5.8 illustrates the circumferential grooves (slots) machined into the titanium disks for the thermocouples, and how the wires were passed through the disk to the back surface, from where they are routed radially outward and eventually to the telemetry system. The thermocouples were arranged in bundles and passed freely through axial holes in the shroud to the back face of disk 4. Slack in the cables was secured under a “lip” machined on the shroud of disk 4; this slack ensured that the disks could be separated when adding or removing the cob attachments. The thermocouple wires were potted directly in the narrow portion of the slot, singly insulated in the wider portion, and double insulated in the through-hole and beyond. The shape of the slots on the disk surface was designed to reduce local stress concentrations as discussed in Chapter 4.

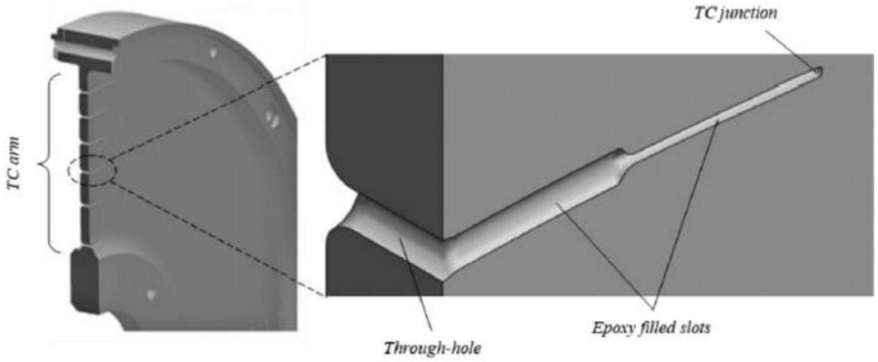

Figure 5.8 – Details of the thermocouple slots.

The slot grooves were designed to span an isotherm at constant radius as the temperature distribution on the disk surfaces was assumed axisymmetric. The thermocouple junctions were placed at the end of the slot, flush with the surface, and the slot was then filled with epoxy resin. The thermal-disturbance error was minimized in two ways. First, the amount of resin in the vicinity of the junction was reduced by sizing the slot to be as small as possible; the end of the slot is rounded with a radius of 0.5 mm. Second, the epoxy resin was specifically selected to satisfy both adhesive criteria (sheer and peel strength) and thermal conductivity; the latter should ideally match the titanium (see Table 5.2). Section 5.4 describes the finite element analysis that was used to estimate the magnitude of the thermal-disturbance error. The maximum error was found to be < 0.25 ˚C, which is less than the uncertainty of the temperature measurement.

In addition to the thermocouples on the disk surfaces, three thin-foil thermocouples were secured to the underside of the cobs at the bore and to the inner surface of the shrouds. Also, at the bore and shroud were three RdF 27160-C-L-A01 thermopile heat flux gauges, each individually calibrated for steady-state measurements between 0.5 and 8 kW/m^2 and gauge temperatures up to 110 ˚C. These gauges each had 54 thermopile junctions made from copper-constantan pairs; the thickness and thermal conductivity of the polyimide film used to separate the junctions were unknown and their values were determined by a Maximum Likelihood Estimation based on the experimental calibration (Pountney et al. 2021).

Two fast-response (100 kHz) unsteady pressure sensors (Kulite XCQ-080, range 1.5 bara) were installed into the surface of disk 3 in order to determine the unsteady cyclonic/anticyclonic structures in the cavity.

Table 5.2 - Relevant mechanical and thermal properties of titanium and epoxy resin.

Titanium (Ti-6Al-4V)	
Density [kg/m^3]	4620
Young's modulus [GPa]	96
Poisson's ratio	0.36
Yield strength [MPa]	889
Thermal expansion coefficient [°C^{-1}]	9.4×10^{-6}
Thermal conductivity [Wm^{-1}K^{-1})	7
Epoxy resin Loctite EA9497 (cured)	
Density (settled) [kg/m]	~2,000
Young's modulus [GPa]	2.4
Thermal expansion coefficient [°C^{-1}]	50×10^{-6}
Thermal conductivity [Wm^{-1}K^{-1}]	1.4
Shear Strength on steel [N/mm^2]	9

5.3.2 Stationary instrumentation

Figure 5.6 shows that the air temperature of the through-flow at the inlet and outlet of the central cavity were measured by means of rakes, each with five thermocouples evenly spaced in the annulus between the stationary shaft and the disk bore. The pressure drop for the through-flow was recorded through five static pressure sensors (ESI Technology Ltd. PR3204) in the stationary shaft.

In future tests, the temperature and the pressure in the cavity core will be measured at various radial locations by one of two stationary instrumented probes, attached to the central shaft; one probe contains K-type thermocouples and the other unsteady pressure sensors (Kulite XCQ-080, range 1.5 bara). To reduce the drag on the probes and the disturbance of the rotating core, each probe has a symmetrical aerofoil section. Future experiments will also involve modifications to incorporate a radial inflow bleed to the instrumented cavity.

Table 5.3 shows the distribution of the instrumentation.

Table 5.3 – Summary of the instrumentation on the Bath Compressor-Cavity rig.

	TC (K-type, in-house welding)	TC (K-type, thin foil)	Heat Flux Gauges	Static Pressure Transducers	Unsteady Pressure Transducers
Shaft				5 (multiple axial locations)	
Annulus	10 (5 per rake, 1 rake per disk)				
Bore D2		3	1		
Bore D3		3			
Diaphragm D2	28				
Diaphragm D3	28				2
Shroud D2		3	1		
Shroud D3		3	1		
Outer Shroud D2	1				
Outer Shroud D3	1				
Total	68	12	3	5	2

5.3.3 Data acquisition system

The wires for the rotating instrumentation were routed to a telemetry unit at the drive-end of the shaft. Six separate modules within the Datatel telemetry unit were able to handle 71 thermocouple and heat flux gauge signals (at 10 Hz), plus two 10 kHz signals (for the fast-response pressure transducers). All the thermocouple signals were cold-junction compensated through a locally installed Pt100 resistance temperature detector. The uncertainty in the temperature of the cold junction is estimated to be ±0.2 ˚C. All thermocouples were made from the same batches of chromel and alumel wires; a sample was calibrated in a water bath up to 100 ˚C, and the standard deviation from the National Institute of Standards and Technology standard was 0.1 ˚C. The data were transmitted to a receiver using an antenna; the overall uncertainty of the temperature acquired from the rotating thermocouples following compensation was estimated to be ±0.5 ˚C, at a 1σ confidence level.

5.4 THERMAL DISTURBANCE ERROR

The thermal-disturbance error is the difference between the undisturbed surface temperature and the temperature measured by the embedded thermocouple bead. It depends on the heat flux and on the ratio of the thermal conductivity of the thermocouple wires, together with the adhesive surrounding them, to that of the titanium disk. The disturbance error is a bias and not a random uncertainty in the temperature measurement.

In the experimental rig, the narrow part of the slot containing the thermocouple bead was 0.5 mm wide and 0.5 mm deep. The chromel and alumel wires were 0.13 mm diameter, with thermal conductivities taken as 19 and 30 W/mK, respectively, and the bead diameter was less than 0.4 mm. The wires and bead were bonded into the slot using an epoxy adhesive (Loctite EA9497) with a thermal conductivity of 1.4 W/mK according to the manufacturer. The surface of the epoxy was made flush with that of the titanium disk (k = 7 W/mK).

The disturbance error was modelled with a steady finite element analysis (FEA) using the ANSYS v18.1 code, and the geometry, based on a 3D segment of the disk containing a thermocouple slot, is shown in Figure 5.9. The unstructured mesh contained 1.69×10^6 elements; the sizes of the elements were 1.5 mm for the disk, 0.08 mm for the slot material and for the disk surfaces in contact with that material, and 0.03 mm at the curved tip of the slot. The actual thermal conductivity of the slot material was assumed to be the volume-weighted-average of the conductivities of the wires, the bead and the adhesive. Three cases were considered for the slot conductivity: pure adhesive (k = 1.4 W/mK); wires and epoxy (k = 3.82 W/mK); bead and epoxy (k = 12.9 W/mK).

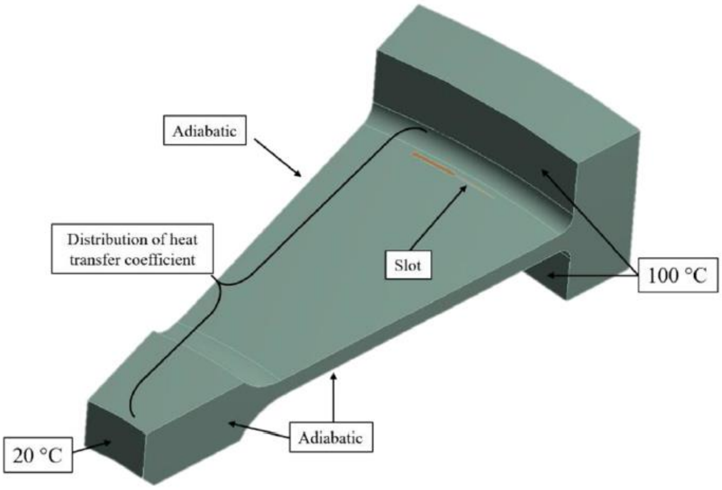

Figure 5.9 – Boundary conditions of the FEA model.

The temperatures of the inner and outer surfaces of the segment were 20 ˚C and 100 ˚C, respectively, and the underside and edges of the segment were assumed to be adiabatic. The heat transfer coefficients for the top surface were calculated using the Buoyancy Model, based on the maximum rotational speed of 8,000 rpm. As the radial location of the slot was the same as that of the outermost thermocouple on the disk, the thermal disturbance error was assumed to be the maximum that would be experienced during the experiments.

The computed angular distribution of surface temperature at the radial centre and circumferential edge of the slot is shown in Figure 5.10 for the three effective slot conductivities referred to above. For the pure epoxy case (k = 1.4 W/mK), the magnitude of the disturbance of the temperature of the slot surface is a maximum (0.24 ˚C); as the heat transfer is from the disk to the air, the surface temperature of the slot is lower than that of the undisturbed temperature. For the wires and epoxy (k = 3.82 W/mK), the maximum magnitude is 0.049 ˚C. For the bead and epoxy (k = 12.9 W/mK), the maximum magnitude is 0.025 ˚C; for this case, where the slot has a higher conductivity than the substrate, the surface temperature of the slot is higher than that of the undisturbed temperature. (It can be seen that the three asymptotic temperatures in the substrate away from the slot differ by a very small amount, < 0.05 ˚C. This difference is caused by the fact that the temperature of the substrate has been altered by the presence of the slot material.)

It is considered that 0.24 ˚C is a conservative maximum and the actual error will be less than this. At the other radial locations and for lower heat fluxes, the errors will be even smaller and therefore insignificant.

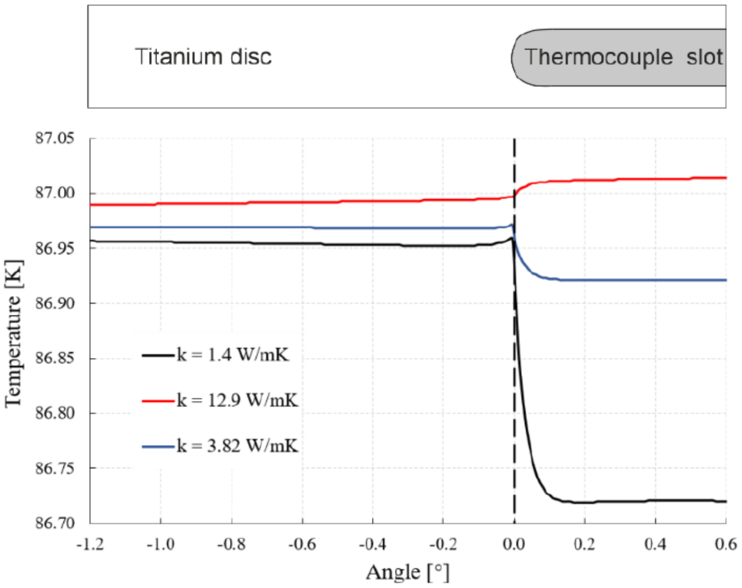

Figure 5.10 - Effect of slot conductivity on computed angular distribution of surface temperature distribution.

5.5 COMMISSIONING AND TESTING

5.5.1 Commissioning

The principal commissioning tests were to establish the rotor-dynamic behaviour of the rig and ensure data could be captured through the telemetry system. The instrumented disks were assembled onto the drive unit with the wiring pinned and connected to the telemetry unit. The disk pack was trim balanced and vibrations monitored over the full operating range (800-8,000 rpm). The maximum allowable vibration of the front bearing was set at 20 μm peak-to-peak (pk–pk). Dynamic calculations for the supercritical design predicted a potential resonance frequency in the range 3,000-4,000 rpm. The design allowed an adjustment of the stiffness of four springs at the front bearing location (near the disks) to control or damp the vibration response.

The variation of the bearing vibration characteristics is shown against rotational speed in Figure 5.11 for both acceleration and deceleration. The data was collected over the period of one hour and the peak-to-peak vibration was less than 7 μm. The data reveals a small degree of hysteresis between acceleration and deceleration. Local resonance peaks were detected in the range 5,000-5,500 rpm, and a more significant peak near 7,000 rpm. The rotor-dynamic response was considered satisfactory to allow rig operation at all rotational speeds up to 8,000 rpm. The vibration data shown in Figure 5.11 were acquired without the cob attachments; repetition of the tests with the cob attachments revealed no detectable change in the vibration characteristics.

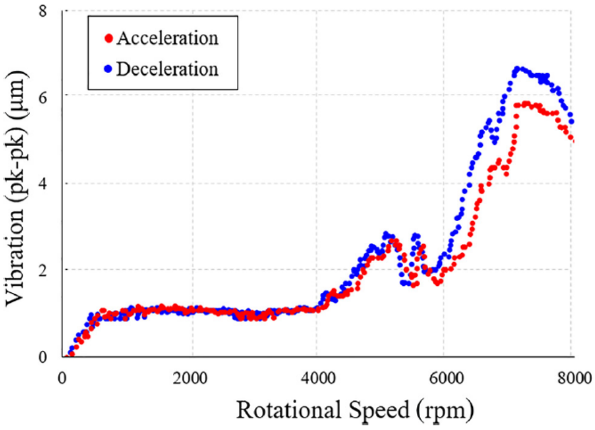

Figure 5.11 - Measured peak-to-peak vibrations in rig acceleration and deceleration (post-trim balancing). Data points refer to moving average of the collected data.

About 70% of the thermocouples on the rotating disks were functioning after the rig commissioning. Most of the losses, however, were encountered in the many handling stages required by the installation rather than the testing itself.

Initial tests of the rig were used to explore steady-state buoyancy-induced flow and heat transfer, with 33 steady-state temperature distributions measured over a range of Gr, $\beta\Delta T$, Ro and Re_z, all with symmetrical heating to the shrouds. A selection of the collected data is discussed below; further analysis of the data is reported in Chapter 7.

5.5.2 Temperature measurements

Figure 5.12 shows the variation of temperature with non-dimensional radius for the following non-dimensional conditions: Re_{ϕ} = 1.6×10^6, $\beta\Delta T$ = 0.24, Ro = 0.2 and Gr = 5.9×10^{11}. The silhouette of the central cavity indicates measurement points, which are aligned radially with the data presented.

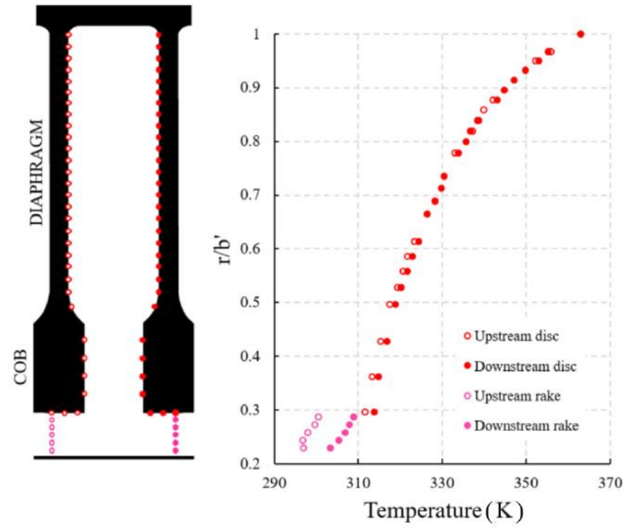

Figure 5.12 - Upstream and downstream disk and rake temperatures: Re_{ϕ} *= 1.6×10*^{6}*;* $\beta\Delta T$ *= 0.24;* Ro *= 0.2;* Gr *= 5.9×10*^{11}*.*

The axial through-flow is left-to-right; the closed and open symbols are for data on the upstream and downstream rotating disks, respectively. Also shown are the air temperatures of the axial through-flow measured just upstream and downstream of the rotating cavity. The temperature rise of the axial through-flow is caused by heat transfer from the rotating surfaces to the through-flow. As shown in Figure 5.1, there is a forced convection region between the through-flow and the core. Referring to Figure 5.12, at the larger radii (r/b > 0.6), toward the shroud and for most of the diaphragm, the differences between the temperatures of the upstream and downstream disks temperatures on the upstream and downstream disks are negligible. The average is used to create a radial distribution for each condition.

Although the estimated uncertainty in individual thermocouple measurements was ±0.5 ºC, it is more meaningful to consider the uncertainty in the disk temperatures estimated from the Bayesian model. The radial distribution of disk temperatures and the standard deviation obtained from the Bayesian model are shown in Figure 5.13. (It is shown in Chapter 6 that the uncertainty in the Nusselt numbers is different than that in the temperatures.) It should be noted that, as the temperature difference between the two disks was very small, the average values are used in this Figure.

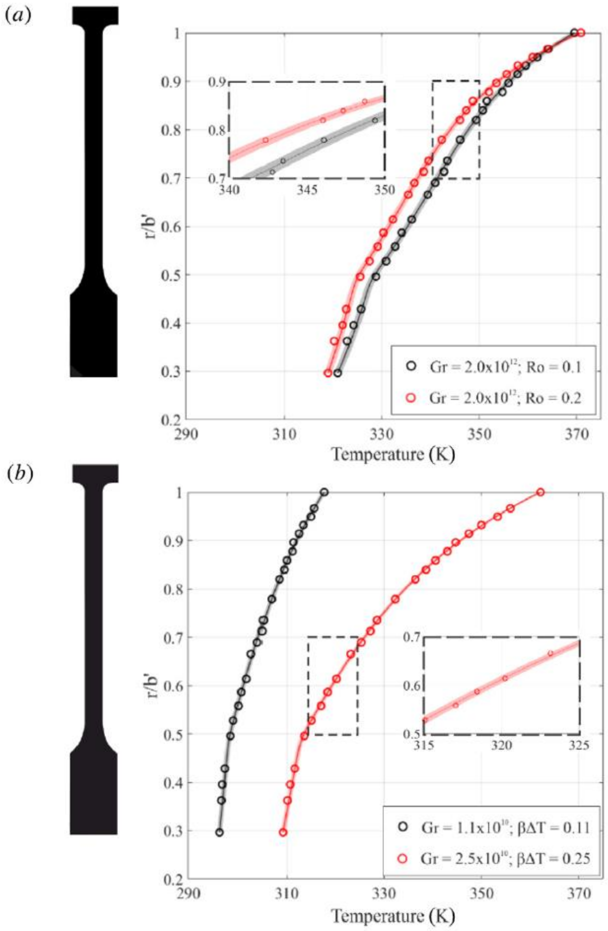

Figure 5.13 - Effect of (a) Rossby number, and (b) $\beta\Delta T$ *on the radial temperature distribution, at two different magnitudes of* Gr*. 95% confidence bounds are shown on the Bayesian distribution. The insert figures show a magnified portion of the curve. For (a),* Re_ϕ *=* 3.0×10^6, Gr *=* 2.0×10^{12} *and* $\beta\Delta T$ *= 0.22. For (b),* Re_ϕ *=* 3.2310^5, Gr *=* 10^{10} *and* Ro *= 0.5.*

Figure 5.13a shows the effect of Rossby numbers for a Grashof number of 2.0×10^{12}, where the standard deviation in the temperature was approximately 0.4 ˚C. The higher Ro increases the forced convection in the cob region, resulting in lower temperatures, especially at low radius. An increase in Ro does not significantly change the profile of the temperature gradient, as the buoyancy forces are constant. However, as the through-flow acts as a stronger heat sink with more enthalpy transfer, the temperatures on the disks are reduced. Figure 5.13b shows the effect of $\beta\Delta T$ for a rotational Reynolds number of 3.2×10^5 where the standard deviation was approximately 0.25 ˚C. Although an approximate doubling of $\beta\Delta T$ has a large effect on the temperature distribution, this is primarily due to the fact that the temperature of the shroud has been increased.

Figure 5.14 shows typical radial distributions of Θ, the non-dimensional temperature of the axial through-flow, whose definition is recalled:

$$\Theta = \frac{T_0 - T_f}{T_{0,b'} - T_f} \tag{5.1}$$

Here T_f is the upstream average temperature of the through-flow, T_o is the local through-flow temperature, and $T_{o,b'}$ is the disk temperature at $r = b'$. As expected, Θ increases as $\beta\Delta T$ increases and as Ro (which is proportional to the flow rate) decreases. The turning point in the downstream distributions of temperature is attributed to the mixing between the cold through-flow and the heated recirculating flow in the inner region of the cavity. As part of the ongoing research program, the through-flow temperatures will be used to provide a heat balance between the heat transfer from the rotating surfaces and the enthalpy rise of the through-flow.

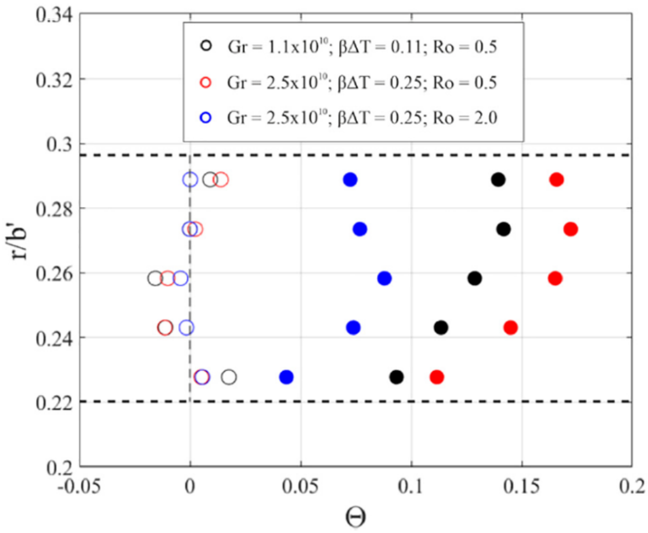

Figure 5.14 - Effect of $\beta\Delta T$ and Ro *number on the radial temperature distribution in the axial through-flow upstream and downstream of the test cavity. Refer to Figure 5.6 for locations of the rakes.* Re_ϕ = *3.2×10*^{5}.

5.6 SUMMARY AND MAIN FINDINGS

The Bath Compressor-Cavity Rig has been designed to investigate the buoyancy-induced heat transfer that occurs inside the compressor rotors of aero-engines. The test section includes four rotating disks enclosing three cavities; the central cavity is instrumented with thermocouples and the outer cavities are thermally insulated. There is an axial through-flow of air between a stationary central shaft and the bore of the disks. For a cold through-flow, the outer shroud of the central cavity is heated by two radiant heaters, which allow different shroud temperatures on the upstream and downstream disks. There is provision for the through-flow to be heated to investigate cases with negative Grashof numbers, which can occur during engine accelerations and decelerations when the through-flow is hotter than the shroud. As stratified flow could occur under these conditions – significantly reducing convection in the cavity so that radiation could be dominant – all internal surfaces of the cavity were painted matt black; this allows the accurate calculation of the radiant heat transfer.

Modularity and flexibility have been addressed in the design of the rig. A rail system allows movement of the disk pack relative to the drive unit and access to the test section. Separate attachments can be fitted to the cobs of both central disks; the attachments reduce the axial gap between the cobs – reducing the gap to zero creates a closed cavity, which can occur in some compressor designs. The whole disk pack might be substituted without changing the rest of the installations, if needed. This might occur in case of instrumentation loss (due to wear) or extensive changes required in the geometry of the cavity (e.g. thermocouples in multiple cavities and real engine geometries falling outside the current flexibility).

Both titanium disks forming the central cavity featured a radial distribution of 28 thermocouples across the cob and diaphragm regions. The thermocouples were located in circumferential slots designed to minimize stress concentrations and thermal disturbance. Other instrumentation on the rotating disks included heat-flux gauges and high-frequency pressure transducers. Attention has been given to experimental errors, including the computation of thermal-disturbance errors, caused by thermocouples embedded in the rotating disks and estimated via FEA, and the use of a Bayesian model to reduce the effect of uncertainties in temperature measurements on the calculation of Nu.

In non-dimensional terms, the rig can operate over the range $-1.2\times10^{12} < \mathrm{Gr} < 2\times10^{12}$, $0.1 < \mathrm{Ro} < 0.8$, and up to $\mathrm{Re}_\phi = 3\times10^6$, $\mathrm{Re}_z = 4\times10^4$ and $\beta\Delta T = 0.25$. The effect of Ro and $\beta\Delta T$ on the radial distribution of both the disk and through-flow temperatures has been shown for some typical cases. Disk temperatures measured on the rig are used in Chapter 6 to determine the effect of Re_ϕ, Ro and $\beta\Delta T$ on the radial distribution of Nu.

Chapter 6

Measurement and analysis of buoyancy-induced heat transfer in the Bath Compressor-Cavity rig

This Chapter originates from the paper:
Jackson, R. W., Luberti, D., Tang, H., Pountney, O. J., Scobie, J. A., Sangan, C. M., Owen, J. M., and Lock, G. D., 2021. *Measurement and Analysis of Buoyancy-Induced Heat Transfer in Aero-Engine Compressor Rotors. ASME. J. Eng. Gas Turbines Power. June 2021*, 143(6): 061004. https://doi.org/10.1115/1.4049100.

This Chapter shows the results of the first experimental campaign performed with the Bath Compressor-Cavity Rig. Steady-state temperature data were collected over a range of engine-representative parameters. The radial distributions of disk temperature were measured under carefully controlled thermal boundary conditions appropriate for analysis using a Bayesian model combined with the equations for a circular fin. The Owen-Tang Buoyancy Model has been used to compare predicted radial distributions of disk temperatures and Nusselt numbers with some of the experimentally determined values, taking also account of radiation between the interior surfaces of the cavity.

The non-dimensional parameters used in the investigations are the Nusselt number Nu (which uses the heat transfer coefficient h_f based on the through-flow temperature T_f), the rotational Reynolds number Re_ϕ, the Grashof number Gr, the Rossby number Ro and the buoyancy number Bo. All the definitions were reported in Chapter 2.

The results provide critical insight of the effect of the buoyancy forces on the heat transfer in the cavity and its dependence on the non-dimensional parameters (particularly rotational Reynolds number). Applying the Bayesian model and the circular fin equation, the Nusselt number results lower at lower radii, much higher at higher radii, suggesting the presence of two zones dominated by different heat transfer mechanisms.

6.1 REVIEW OF MODELS USED FOR DATA ANALYSIS

Experimental data can be analysed via the three different mathematical models presented in Chapter 2: the Bayesian statistics, the circular-fin equation, and the Owen and Tang Buoyancy Model. The relevant aspects for the data analysis are highlighted below.

6.1.1 Bayesian model

Thermocouple measurements are prone to several sources of error. These include conduction errors (owing to conduction down the wires), thermal-disturbance errors (caused by differences between the thermal conductivity of the thermocouples and that of the substrate), and sparseness of data (owing to an insufficient number of thermocouples to reduce statistical uncertainties in the calculated fluxes). The instrumentation has been fitted to minimize these errors yet the resulting uncertainty in the measured temperatures was still estimated to be ±0.5 °C. Determining the heat transfer coefficient, h, from temperature measurements is an inverse problem; small uncertainties in the measurements can create very large uncertainties in the calculated values of h (Owen 1979).

Bayesian statistics are widely used to solve inverse problems and Tang et al. 2015 showed how a Bayesian model could be used to accurately determine Biot numbers, Bi from measured disk temperatures (here Bi $= h_f b/k_o$ and k_o is the thermal conductivity of the disk). The model assumed that there was a smooth radial distribution of Nusselt number, which was then used as the boundary condition for the *direct* solution (as opposed to the *inverse* solution) of the circular fin equation – which is discussed below – to calculate the disk temperatures. Using the Bayes theorem, the distribution of Bi was changed iteratively until satisfactory convergence was achieved between the calculated and measured temperatures.

Using simulated ‘noisy’ temperature measurements, the effectiveness of the Bayesian model was demonstrated, producing a smooth distribution of Bi, and the computed 95% confidence interval captured the true distribution. By contrast, conventional curve fitting of the noisy temperatures, used as boundary conditions for the inverse solution of the fin equation, resulted in large oscillations and inaccurate results.

6.1.2 Circular-fin models

The axial temperature difference across the thin diaphragm section of each disk is usually negligible (Atkins and Kanjirakkad 2014, Tang et al. 2018). As the temperature distribution is axisymmetric, the circular-fin equation, which is one-dimensional, can be used to calculate the radial distribution of disk temperature. Tang et al. 2015 used the term *special fin equation* for the diaphragm section with a constant thermal conductivity, and *general fin equation* for the case where the disk thickness and conductivity varied with radius. The *special fin equation* is used below with the Tang-Owen Buoyancy Model, and the general fin equation is used with the Bayesian model. In both cases, it is necessary to specify the temperature or heat flux at the inner and outer radii of both disks in the cavity.

The use of the fin model implicitly assumes there are no axial temperature differences within a disk. Consequently, either the convective boundary conditions on the two surfaces must be the same or one surface must be insulated; the zero axial temperature gradient is equivalent to a symmetry axis on the insulated surface. The flow, and therefore the Nusselt numbers, in adjacent cavities in a multi-cavity rig are in principle not identical.

The Bath Compressor-Cavity Rig is a three-cavity rig, and the temperatures of both disks and shrouds are measured only in the central cavity; the surfaces of the outer cavities are thermally insulated. Importantly, only one surface of a disk needs to be instrumented if the (1D) fin equation is used for the analysis, whereas both surfaces must be instrumented if a 2D solver is used. That is, for a given number of thermocouples, twice as many disks can be analysed using the fin equation.

6.1.3 Owen-Tang Buoyancy Model

A simplified representation of the assumed flow structure is shown in Figure 6.1. The Buoyancy Model assumes buoyancy-induced Ekman-layer flow on the rotating disks in the cavity and an inviscid rotating core of fluid between the Ekman layers. In practice, cyclonic and anticyclonic vortices are formed in the core, but in the model the flow is assumed to be axisymmetric (average flow).

The Buoyancy Model comprises the three sub-models described below: the Ekman-layer equations, compressible flow in the core, and the circular-fin equation.

The linear laminar Ekman-layer equations are solved for the disks, and the compressible adiabatic equations are solved for the core temperature; these two coupled equations are referred to here as the buoyancy equations. The circular fin equation is used to calculate the disk temperatures, using Nusselt numbers determined from the buoyancy equations, and the calculated temperatures are then used in the buoyancy equations to update the Nusselt numbers. The coupled buoyancy and fin equations are solved iteratively until convergence is achieved. The distributions of the Nusselt numbers and disk temperatures predicted by the combined fin and buoyancy equations can then be compared with the distributions obtained from the Bayesian model.

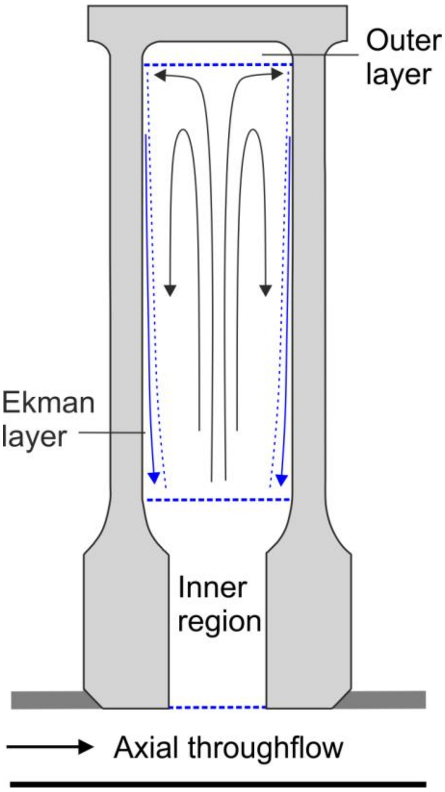

Figure 6.1 – Compressor cavity flow structure.

The Owen and Tang Buoyancy Model includes an empirical Coriolis parameter, Co, which is the ratio of buoyancy to Coriolis forces in the Ekman layers. In Tang and Owen 2017 a sensitivity in the Co parameter was performed, showing that doubling the parameter value would result in an increase of 10% of the averaged Nusselt number. A value $Co = 0.03$ was used by Tang et al. 2018 to predict experimental data from the Sussex rig, and that value is used in this Chapter. (Tang et al. 2018 assumed that, at the inner radius of the disk, the Nusselt number was zero and the core temperature was equal to that of the disk. Although these assumptions were consistent with the published experimental data, it is shown in this Chapter that they are not universally valid). With reference to equation (2.71), the Coriolis parameter depends on the slip velocity of the fluid in the cavity with respect to the disks and on the temperature difference between disk and core at $r = b$. The Bath Compressor-Cavity rig has been designed with the capability to estimate these quantities and provide, if needed, a better value for this parameter. However, as regards the slip velocity, experimental observations in early rigs estimated a constant slip velocity of 10-12% (Bohn et al. 2000), which is consistent with the presence of Ekman layers (Section 2.1.2).

Unlike the Bayesian model, the Buoyancy Model does not use the measured distribution of disk temperature. However, as stated above, the fin equation does require temperatures or fluxes to be specified for the boundary conditions at the inner and outer radii of the disk. (Although the 1D fin equation is used for convenience, the buoyancy equations can be readily used with 2D conduction solvers.) In this thesis, the boundary conditions for the fin equation were the measured temperatures at the inner and outer radii of the disk diaphragm (i.e. $r = a'$ and $r = b'$). Furthermore, the Buoyancy Model has been applied to the buoyancy-dominated region on the disk diaphragm, assuming a starting point of $\mathrm{Nu_c}$ = 0 (and thus $\mathrm{Nu}_f = 0$) at the outer radius of the cob fillet ($r = a'$). These choices are consistent with Tang and Owen 2017.

A flow chart of the Buoyancy Model is reported in Figure 6.2 to show how it has been used throughout this Chapter.

The term ‘*experimentally-derived values*’ is used in this Chapter to refer to the measured temperatures, and to the temperatures and Nusselt numbers determined using the Bayesian model; ‘*theoretical values*' refer to the temperatures and Nusselt numbers predicted from the Buoyancy Model. If not directly specified, in this Chapter Nu and Gr refer to Nu_f and Gr_f.

Twenty-nine tests for open cavities (Tang et al. 2018, Tang and Owen 2017) and 194 tests for closed cavities (Tang and Owen 2018) have been analysed by these models over a wide range of experimental parameters, and good agreement was achieved in most cases. An important finding from the analysis of all these experiments is that – owing to the temperature rise created by the compressible flow of the core – at high rotational speeds Nusselt numbers can decrease as the speed increases. This effect has been experimentally observed (Section 6.4).

At *prima facie*, it might seem surprising that laminar Buoyancy Models are appropriate for large Grashof numbers ($\mathrm{Gr} \sim 10^{12}$), where turbulent flow would be expected. However, the large Coriolis accelerations will attenuate turbulence in the fluid core and the differences between the rotational speed of the core (near solid-body rotation) and the disks is relatively small.

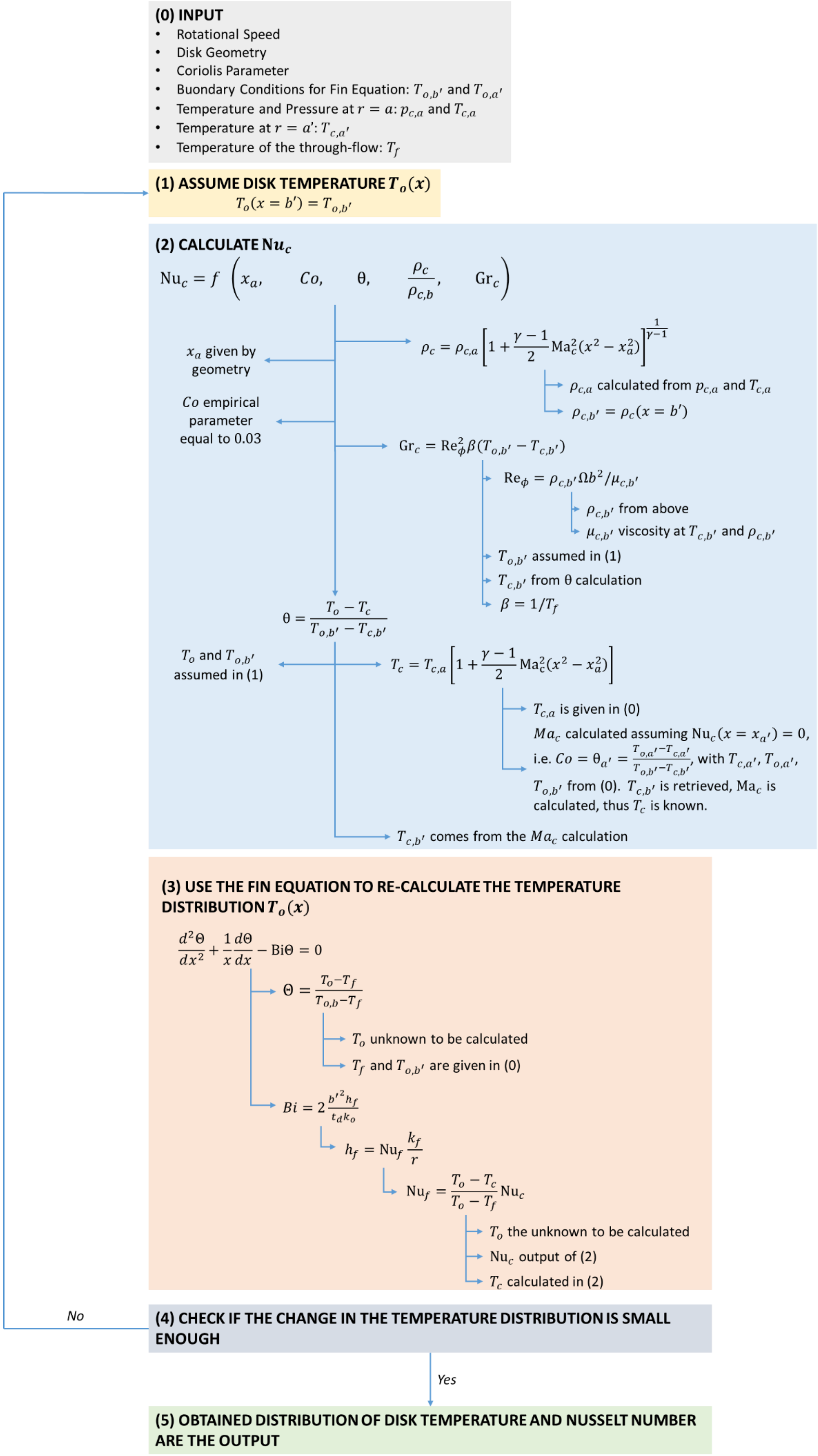

Figure 6.2 – Flow chart of the use of the Buoyancy Model together with the fin equation.

6.2 BATH COMPRESSOR-CAVITY RIG

The Bath Compressor-Cavity Rig and its capabilities have been presented in Chapter 5.

A sectional view of the central cavity showing the principal dimensions and the locations of the disk instrumentation is shown in Figure 6.3. The inner surfaces of the upstream and downstream cavities (either side of the test cavity) were lined with Rohacell, a low-conductivity machinable foam (thermal conductivity 0.03 W/mK). This arrangement creates a near adiabatic boundary on the external surfaces of the disks in the test cavity: this is important for the accurate application of the circular-fin model.

Both upstream and downstream disks feature a radial distribution of 28 K-type thermocouples across the cob and diaphragm regions. The thermocouple wires were potted directly into circumferential grooves machined into the titanium and filled with epoxy resin specifically selected to minimise thermal disturbance errors. The thermocouples were manufactured from a single batch of wire to minimize any variation in the Seebeck coefficient. In addition to the thermocouples on the rotating disks, three thin foil thermocouples were secured on the underside of the disk shroud and under the cob in the bore flow using adhesive Kapton tape.

The wires of the rotating thermocouples were routed through the disk drum and drive unit to a telemetry unit at the drive end of the shaft; here the wires were pinned into the sockets of the acquisition channels in five separate transmitter modules. Each module contained a PT100 resistance temperature detector (RTD) to measure the cold junction temperature. The RTDs were connected in a four-wire configuration to ensure that the wire resistance can be neglected. The uncertainty in the temperature of the cold junction, at a 1σ confidence level, is approximately ±0.2 °C. The thermocouple and RTD data were relayed from the telemetry unit to the receiver via an antenna, and the data was then converted to a compensated temperature using a known calibration. The total estimated uncertainty of the rotating thermocouples is around ±0.5 °C, also at a 1σ confidence level.

Figure 6.3 also shows rakes containing five K-type thermocouples, which were positioned immediately upstream and downstream of the central cavity to measure the through-flow temperature. The thermocouples in each rake were evenly spaced in the annulus between the stationary shaft and the disk bore. The mean average temperature from the upstream rake was used to calculate the inlet temperature of the through-flow, T_f, with an estimated uncertainty of ± 0.3 °C.

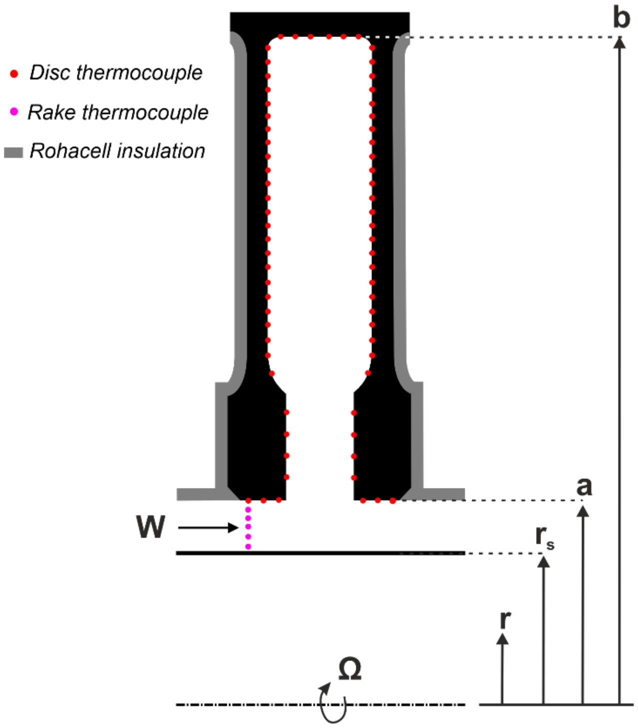

Figure 6.3 – Cross-section of the cavity, showing thermocouple locations and the main dimensions.

Steady-state temperature data was acquired at a sampling rate of 10 Hz. The normalized temperature, Θ, was used to assess whether the conditions were steady-state:

$$\Theta = \frac{T_o - T_f}{T_{o,b'} - T_f} \tag{6.1}$$

T_f is the average temperature of the through-flow upstream of the cavity, and $T_{o,b'}$ is the temperature measured from the thermocouple at the highest radius on the diaphragm (*i.e.* closest to the shroud). A steady-state condition was defined to be when the median average of Θ for each disk thermocouple changed by less than 0.01 between a pair of ten-minute intervals. This was typically achieved after a period of 1.5 to 2 hours of continuous operation.

As part of a series of commissioning tests for the rig, a total of 30 experiments were conducted over a range of Re_ϕ, $\beta \Delta T$ and Ro. The range is shown in Figure 6.4 on a series of iso-Re_ϕ lines. For each data point on the Gr versus $\beta \Delta T$ chart of Figure 6.4a, two to three cases were collected at different Ro, as shown in Figure 6.4b (Ro versus Re_z). The experimental range and typical uncertainty of each parameter is given in Table 6.1.

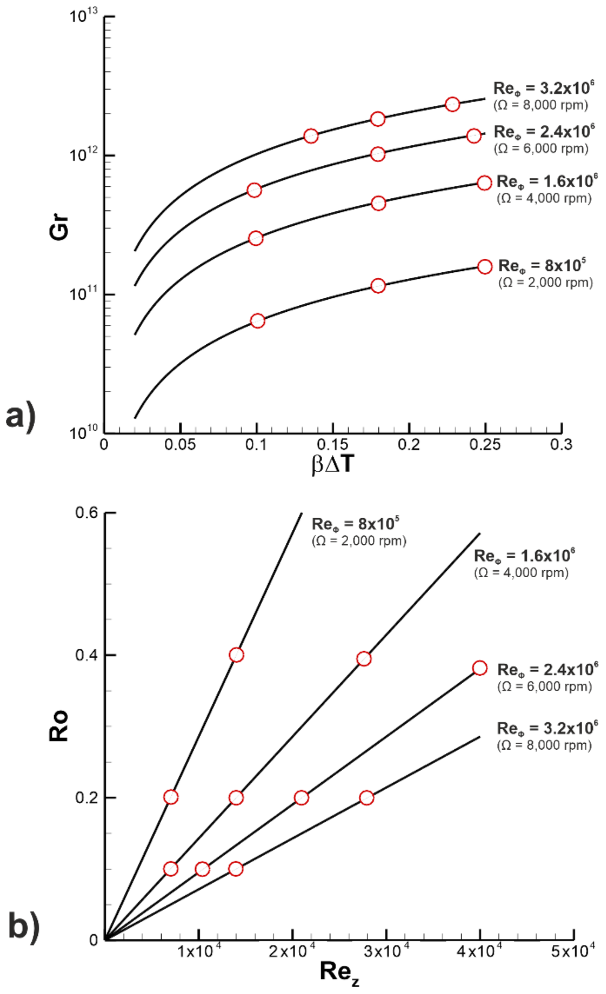

Figure 6.4 – Test conditions, showing the variation of Gr *with $\beta\Delta T$ (a) and the variation of* Ro *with* Re_z *(b).*

Table 6.1 – Parameter ranges and typical uncertainties.

a)	*Parameter*	Ω [rpm]	ΔT [°C]	$\dot{m}$ [kg/s]
	Range	2,000 – 8,000	30 – 80	0.025 – 0.139
	Uncertainty	±10	±1	$\pm 5\times10^{-4}$

b)	*Parameter*	$\beta\Delta T$	Re_ϕ	Gr	Re_z	Ro
	Range	0.1 – 0.25	$7.7\times10^5 – 3.0\times10^6$	$7.0\times10^{10} – 2.0\times10^{12}$	$6.4\times10^3 – 4.0\times10^4$	0.1 – 0.4
	Relative Uncertainty	±1.5%	±0.5%	±2%	±4%	±4%

6.3 DATA ANALYSIS

The models used to analyse the data were described in Section 6.1. This Section describes the application of this analysis to a single, example experimental case (Re_ϕ = 3.2×10^6; $\beta\Delta T = 0.23$; $\mathrm{Gr} = 2\times10^{12}$; Ro = 0.2). Section 6.4 presents data over the full range of engine-representative non-dimensional parameters listed in Table 6.1.

6.3.1 Conversion of temperatures to Nusselt numbers

Figure 6.5 shows the radial distribution of temperature across the disk, T_o, for the example case (Figure 6.5a), as well as the normalized temperature, Θ (Figure 6.5b). The measurement locations are indicated on the silhouette of the central cavity, which is aligned radially with the data presented. The axial through-flow is left-to-right; the closed and open symbols are for data on the upstream and downstream rotating disks, respectively. The temperatures of the axial through-flow measured upstream and downstream of the cavity are also shown.

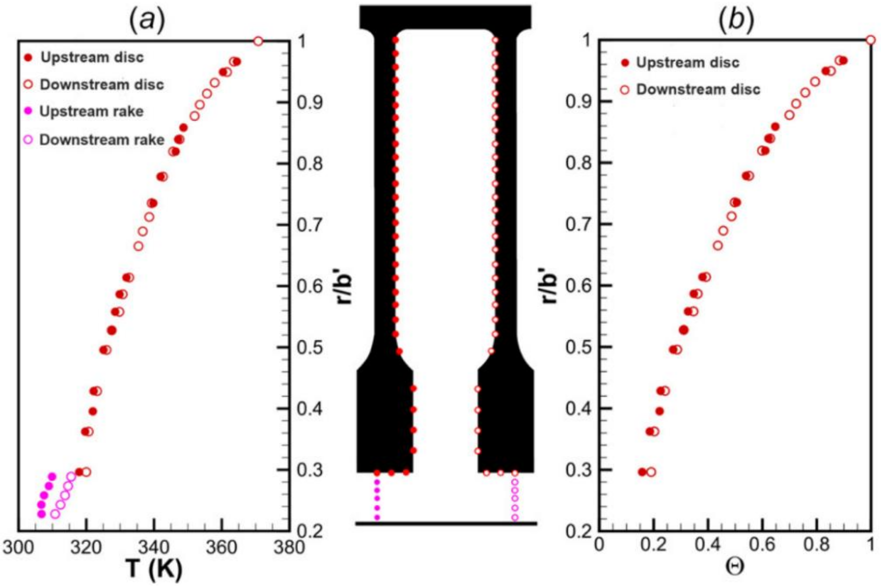

Figure 6.5 – Raw temperatures (a) and non-dimensional temperatures (b) on the upstream and downstream disk, for an example case (Re_ϕ *= 3.0×10*^{6}*;* Gr *= 2.0×10*^{12}*;* Ro *= 0.2).*

The radial temperature gradient on the rotating disks is shown clearly; this will drive buoyancy-induced flow at this large value of Gr. At radii approaching the shroud and for the greater portion of the diaphragm ($r/b' > 0.6$), the temperatures on the upstream and downstream disk mainly agree within the experimental uncertainties; an average of disk temperatures is used in the analysis below. Close to the bore, especially in the region of the cobs, the downstream disk is slightly hotter than the upstream one. There is a clear rise in temperature of the axial through-flow due to an exchange in enthalpy with the rotating cavity and the heat transferred directly from the bore of the cobs.

Figure 6.6a shows the variation of the averaged temperature at discrete points across the radius of the disk. The Bayesian model has been applied to provide an experimentally-derived continuous radial variation shown by the line. The Bayesian model, in conjunction with the circular-fin equation, has been used to determine the variation of heat flux (from Bi) with radius; this is plotted in Figure 6.6b. (Note that any two-dimensional effects in the cob region, determined using a 2D FEA solver, have been shown to be negligible.)

The heat flux, q_o, shown in Figure 6.6b is due to both convection and radiation; the two components are separated in the discussion below. Positive q indicates that heat is transferred from the disk surface to the air in the cavity. There is a steep gradient in q for r/b' > 0.6, suggesting that buoyancy-induced flow dominates at high radius in the cavity. For r/b' < 0.6, the heat flux is relatively constant and at a significantly reduced magnitude. The data suggests two regions of heat transfer: the buoyancy-dominated region on the diaphragm, principally governed by Gr; and a forced convection zone in the region of the cobs where the mechanism for heat transfer is controlled by Re_z.

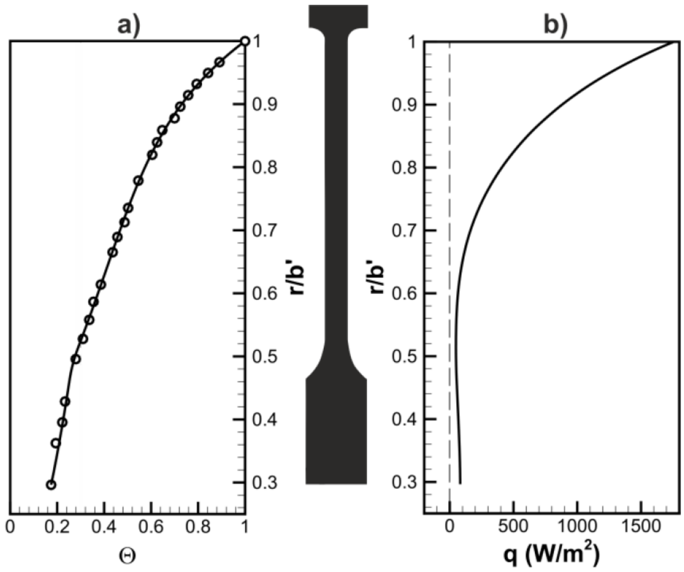

Figure 6.6 – Radial distribution of Θ (a) and q (b), calculated from the Bayesian model.

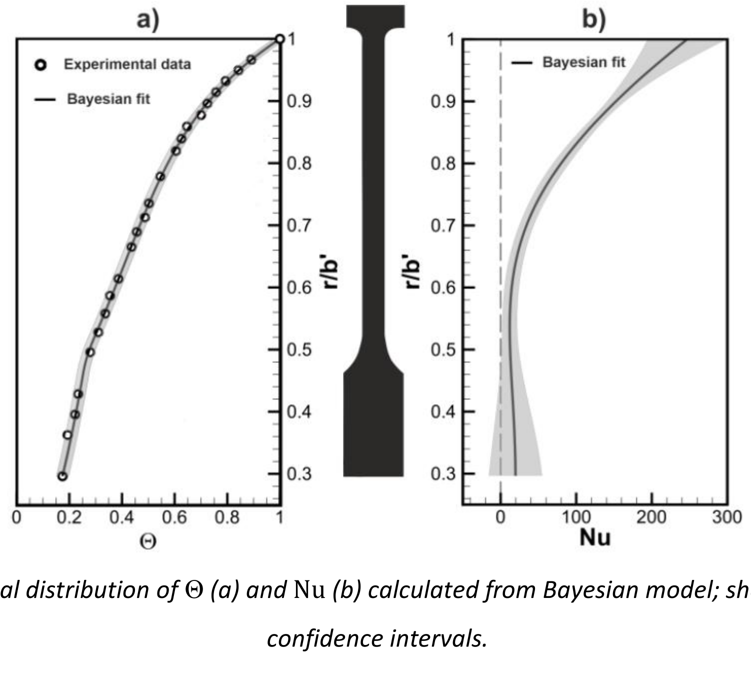

Figure 6.7 – Radial distribution of Θ (a) and Nu (b) calculated from Bayesian model; shading shows 95% confidence intervals.

The variation of experimentally-derived Nusselt numbers with radius is presented in Figure 6.7. The shaded 95% confidence intervals of the Bayesian method in Θ (Figure 6.7a) and Nu (Figure 6.7b) are also shown. In a qualitatively similar manner to the distribution of q, Nu increases towards the outer radius, where the heat transfer is buoyancy-dominated.

The total heat flux shown in Figure 6.6b is a combination of the convective and radiative heat flux components. The shaft, shroud and the disk surfaces, which surround the cavity, were painted matt black to allow the accurate calculation of the radiant heat transfer – see Tang and Owen 2021. The two components of heat flux are presented in Figure 6.8. The radiative component, marked by a red line, is subtracted from the total to give the convective contribution. The surfaces at $r/b' > 0.95$ (where the radiative heat flux is positive) lose heat due to radiation, while surfaces elsewhere gain heat. At large radius, where heat transfer is buoyancy-dominated, the radiation component is relatively small, but it is significant in the cob region.

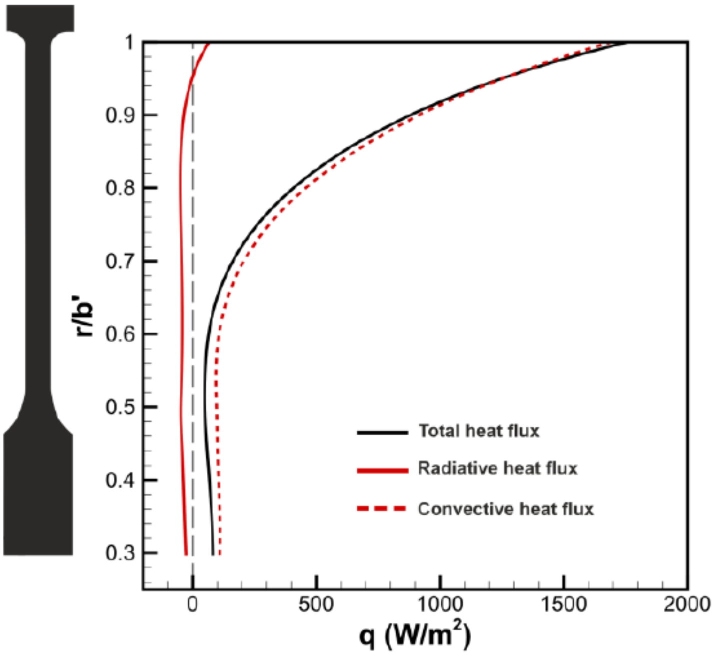

Figure 6.8 – Effect of radiation on radial distribution of heat flux.

6.3.2 Application of Owen-Tang Buoyancy Model

Figure 6.9 compares the measured temperatures and experimentally-derived temperatures (left) and Nusselt numbers determined using the Bayesian model (right) with the theoretical values of temperature and Nusselt numbers predicted from the Buoyancy Model. Figure 6.9a shows the example experimental case ($\beta\Delta T$ = 0.23; Re_ϕ =

3.0×10^6; Gr = 2.0×10^{12}; Ro = 0.2; Bo = 3.0×10^3); Figure 6.9b describes a case at $\beta\Delta T$ = 0.14 (Re_ϕ = 3.0×10^6; Gr = 1.2×10^{12}; Ro = 0.2; Bo = 1.7×10^3).

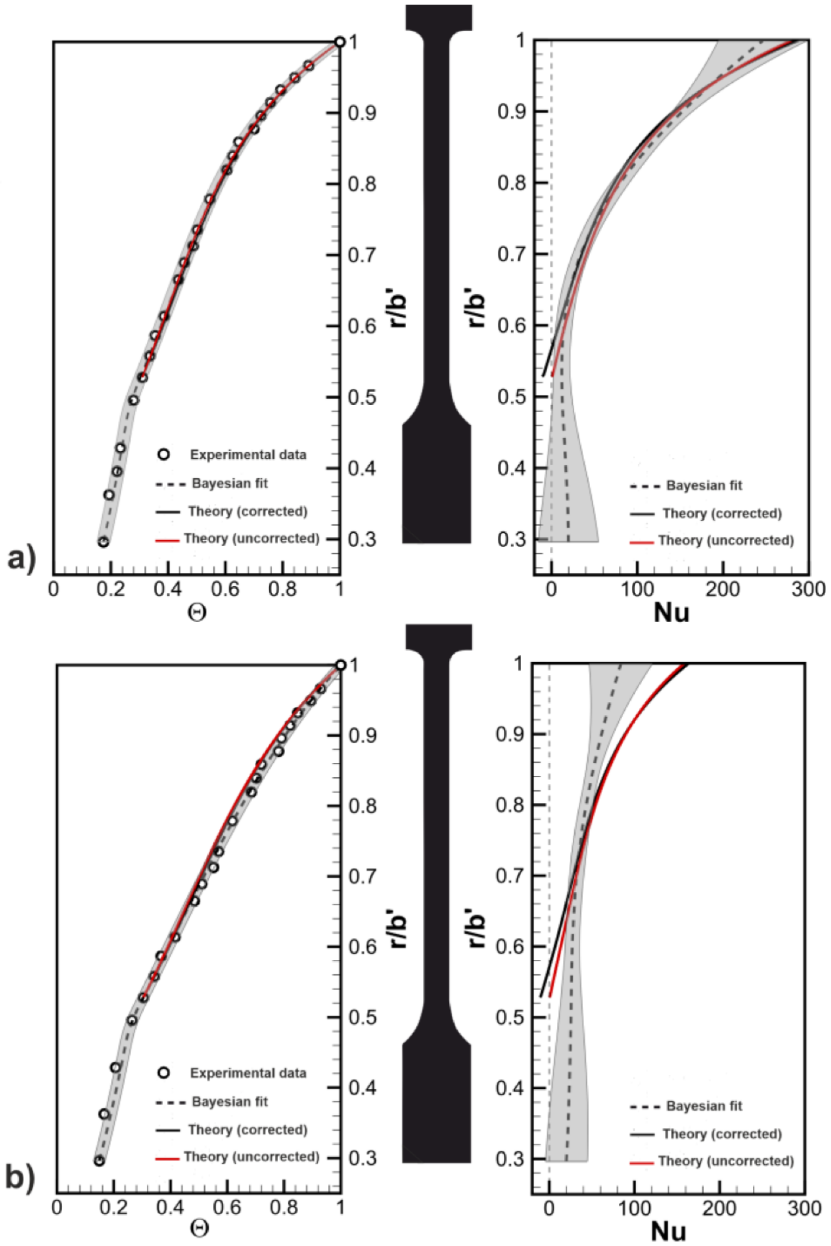

Figure 6.9 – Effect of radiation on radial distribution of Θ *and* Nu *calculated from Bayesian and Buoyancy Models; shading shows 95% confidence intervals. In (a),* $\beta\Delta T$ *= 0.23 (*Gr *=* 2.0×10^{12}*;* Bo *=* 3.0×10^3*) and (b),* $\beta\Delta T$ *= 0.14 (*Gr *=* 1.2×10^{12}*;* Bo *=* 1.7×10^3*).* Re_ϕ *=* 3.0×10^6 *and* Ro *= 0.2 for both cases.*

The Owen and Tang Buoyancy Model is only applied to the buoyancy-dominated region on the diaphragm, assuming a starting point of $\mathrm{Nu_c}$ = 0 (and thus $\mathrm{Nu}_f = 0$) at the outer radius of the cob fillet ($r = a'$, i.e. r/b' = 0.52) before the radiation correction is applied. Compressibility effects are considered in the model, from which the radial distribution of the core temperature is calculated.

The Buoyancy Model only considers convective heat transfer and a correction for radiation must be applied in order to compare with the experimentally-derived radial variation of temperature and Nusselt number (marked 'Bayesian fit'). The red lines show the theoretical values of Θ (left) and Nu (right) from the model, and the black lines are corrected for radiation. The effect of the radiation correction on the temperatures and on Nu at large radius is small. At low radius the radiation causes a reduction in Nu to negative values.

The predicted values compare well with the experimentally-derived temperatures (left) and Nusselt numbers in the high $\beta\Delta T$, high Bo case (Figure 6.9a), quantitatively agreeing within the confidence intervals. The comparison for the low $\beta\Delta T$, low Bo case (Figure 6.9b) is not as good. This suggests that the effects of forced convection can be significant in the inner region between the through-flow and the core, and the Buoyancy Model needs to be extended to include these effects. However, the temperature distribution, which is of principal interest to the designer, is reasonably well predicted by the model even at low Bo.

6.4 EXPERIMENTS OVER A RANGE OF Gr, Ro, Re_{ϕ}

Section 6.3 described an example experimental case. This section presents experimentally-derived Nusselt numbers over the range of engine-representative non-dimensional parameters illustrated in Figure 6.4. Rather than present the radial variation of Nu, the data is presented as an integrated radially-weighted average, $\overline{\mathrm{Nu}}$, over the disk surface.

Figure 6.10 illustrates the effect of $\beta\Delta T$ and Re_{ϕ} on the variation of $\overline{\mathrm{Nu}}$ with Gr; for all cases, Ro = 0.2. Consider first the physical effects of $\beta\Delta T$. For a fixed rotational speed, $\overline{\mathrm{Nu}}$ increases with increasing $\beta\Delta T$, due to the buoyancy forces driving the convection.

As Re_{ϕ} increases, Gr increases but, owing to compressibility effects, the core temperature also increases; the latter tends to reduce the heat transfer. As a result, there is a critical rotational Reynolds number for which $\overline{\mathrm{Nu}}$ is a maximum; this critical value of Re_{ϕ} increases as $\beta\Delta T$ increases.

Consider now the two pairs of data at common Gr (0.6×10^{12} and 1.2×10^{12}), but different Re_{ϕ} and $\beta\Delta T$. The juxtaposition of these points is marked in Figure 6.10 by vertical dashed lines. For both pairs, $\overline{\mathrm{Nu}}$ is significantly higher for the case with a larger

$\beta\Delta T$ (increased buoyancy-induced heat transfer) and smaller Re_ϕ (reduced temperature rise in the core created by compressibility effects in the air).

The compressibility discussed above has been reported in other papers for experiments made in different experimental rigs (Tang et al. 2018, Owen and Tang 2015, Tang and Owen 2018). This is explored further in Figure 6.11, which shows the variation of Θ (Figure 6.11a) and Nu (Figure 6.11b) with radius for the two conditions at Gr = 1.2×10^{12} but different Re_ϕ and $\beta\Delta T$. The Nusselt number for the case of larger $\beta\Delta T$ and lower Re_ϕ is relatively greater for $r/b' > 0.65$, where buoyancy-induced heat transfer dominates. However, for $r/b' < 0.65$ Nu → 0 for the case of higher $\beta\Delta T$ (hence higher Bo at the same Ro) in the inner region; Nu for the lower $\beta\Delta T$ (hence lower Bo) case is slightly higher. This is indicative of a change in the relative dominance of the two regions of heat transfer in the cavity, *i.e.* forced convection in the inner region, and buoyancy-induced heat transfer at higher radius. The influence of the through-flow has extended further into the cavity, as reflected in the radial distribution of Θ.

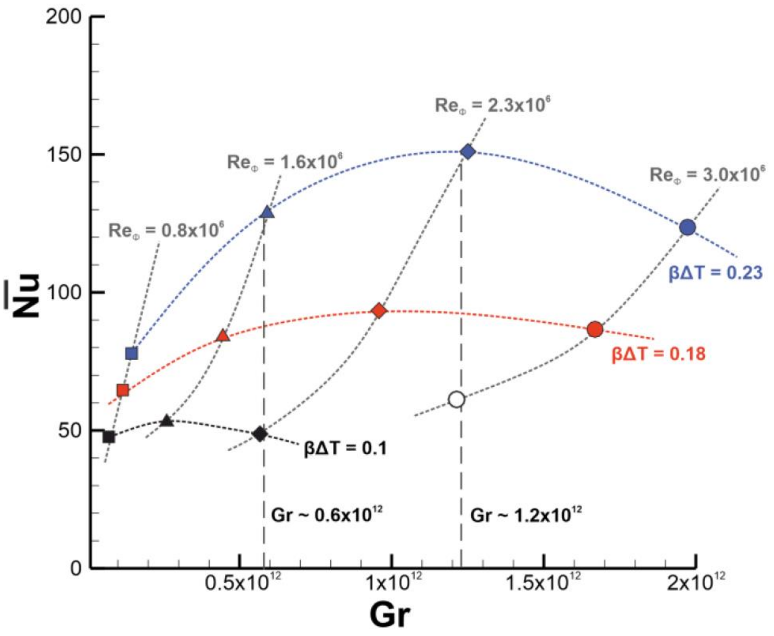

Re_Φ $(x10^6)$	βΔT			
	0.1	0.13	0.18	0.23
0.8	■		■	■
1.6	▲		▲	▲
2.3	◆		◆	◆
3.0		○	●	●

Figure 6.10 – Effect of Re_ϕ *and* $\beta\Delta T$ *on variation of* $\overline{\mathrm{Nu}}$ *with* Gr *(*Ro *= 0.2).*

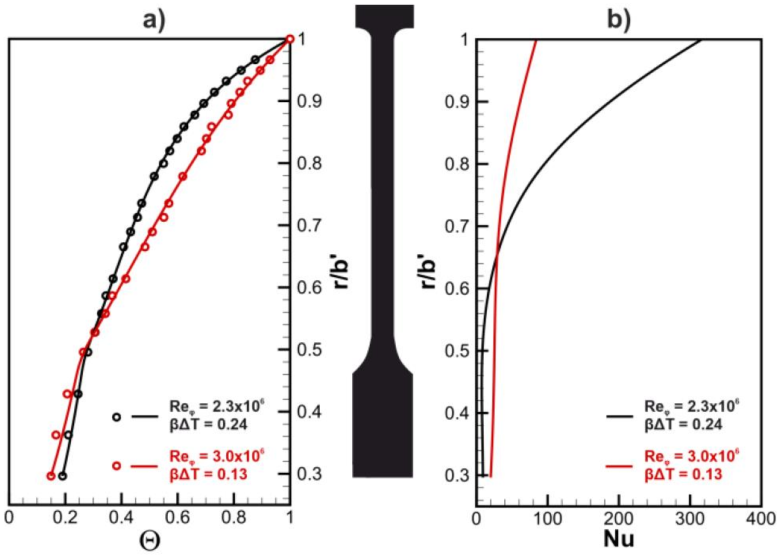

Figure 6.11 – Effect of compressibility on radial distribution of Θ *(a) and* Nu *(b) calculated from Bayesian model; shading shows 95% confidence intervals for* Gr *=* 1.2×10^{12}*. (Black data is taken at* Bo *=* 3.1×10^{3} *and red data at* Bo *=* 1.7×10^{3}*).*

The relative effects of the free and forced convection regions can be quantified by the buoyancy number, Bo; the numerator, $\mathrm{Re}_{\phi}^{2}\beta\Delta T$ (equivalent to Gr) is proportional to the strength of free convection on the disks, while Re_{z}^{2} (the denominator) is proportional to the influence of the through-flow.

Figure 6.12 shows the effect of Ro on the variation of $\overline{\mathrm{Nu}}$ with Bo. It can be seen that $\overline{\mathrm{Nu}}$ increases if either Bo or Ro increase. The effect of Ro can be explained by considering the inner region, which constitutes a combined source-sink for the cavity; it is also a mixing region in which entrained cold through-flow mixes with hot fluid from the Ekman layers. Consequently, the air temperature in the cavity tends to decrease, and the Nusselt numbers tend to increase, as Re_{z} increases. As Ro is proportional to the ratio $\mathrm{Re}_{z}/\mathrm{Re}_{\phi}$, $\overline{\mathrm{Nu}}$ therefore tends to increase as Ro increases. Conversely, for constant Ro, Bo increases as $\beta\Delta T$ increases, and – due to the stronger buoyancy forces – $\overline{\mathrm{Nu}}$ increases as Bo increases.

The effect of the Rossby number on the radial distribution of Θ and Nu is shown in Figure 6.13; here $\beta\Delta T$ = 0.24, Re_{ϕ} = 2.3×10^{6}, and Gr = 1.2×10^{12}. With increasing Ro, Θ (Figure 6.13a) decreases while Nu (Figure 6.13b) increases across all radial locations on the disk. As stated above, the larger rate of through-flow associated with increasing Ro reduces the core temperature and increases the heat transfer.

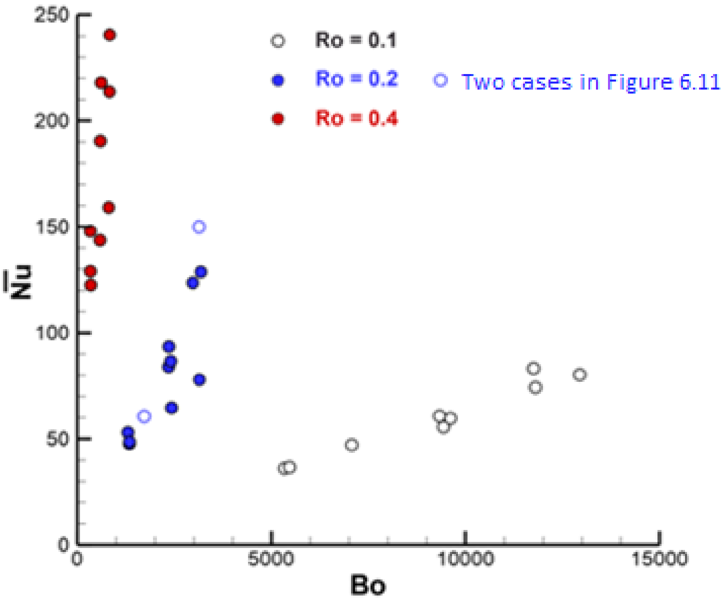

Figure 6.12 – Effect of Ro *on variation of* $\overline{\mathrm{Nu}}$ *with* Bo *(*Bo $\propto \beta\Delta T/\mathrm{Ro}^2$ *)*

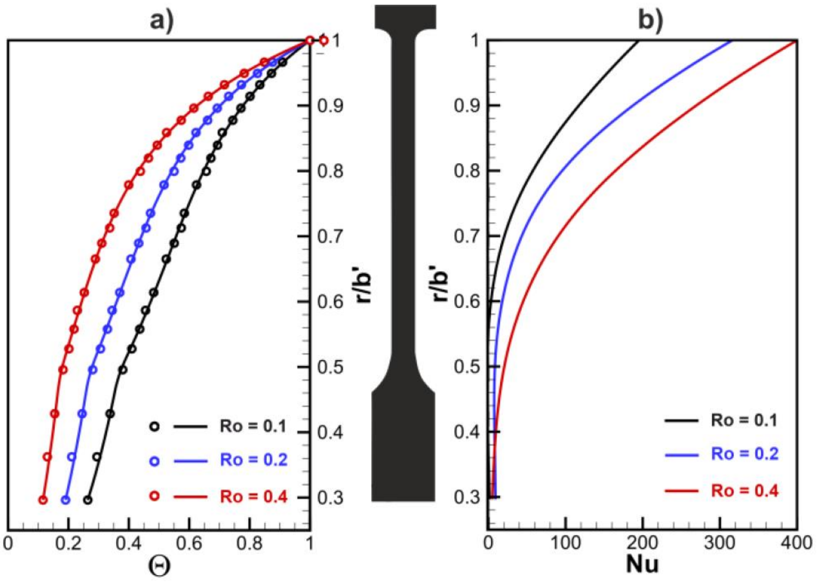

Figure 6.13 – Effect of Ro *on radial distribution of* Θ *(a) and* Nu *(b) calculated from Bayesian model (*$\beta\Delta T$ *= 0.24;* Re_ϕ *= 2.3×10*^{6}*).*

The data presented so far have been an average of the two disks in the cavity. Now the heat transfer for the upstream and downstream disks are analysed separately. Figure 6.14 presents the separated temperatures and Nusselt numbers, respectively, in the inner region, for a case where Ro = 0.4. The axial through-flow is left-to-right; the closed and open symbols are for data on the upstream and downstream rotating disks, respectively. Also shown are the air temperatures of the axial through-flow measured just upstream and downstream of the rotating cavity. The temperature rise of the axial through-flow is caused by heat transfer from the disks and shroud to the through-flow (Figure 6.14a). The combined source-sink and mixing region, where entrained cold through-flow mixes with hot fluid from the Ekman layers, is illustrated in Figure 6.14b.

There are significant differences in the cob region, where the downstream disk is hotter than the upstream one; this is consistent with toroidal vortex flow and forced convection. There is a positive value of Nu for the downstream disk and a negative value for the upstream disk. (This behaviour has also been observed at high Ro in the experimental results of Günther et al. 2012 and the computational results of Pitz et al. 2019) It can be explained by the cold through-flow impinging on the downstream disk first, before recirculating, gaining enthalpy, and then transferring heat to the upstream disk. As a caveat, the fact that the Nusselt number is negative is driven by the way it is calculated. Indeed, the calculated Nusselt number is the non-invariant Nu_f and is obtained with the through-flow temperature T_f as reference temperature.

Although it is not shown here, for $r/b' > 0.6$ (*i.e.* most of the diaphragm region where buoyancy effects dominate) the differences between the upstream and downstream values of Θ and Nu are mainly within the experimental uncertainties.

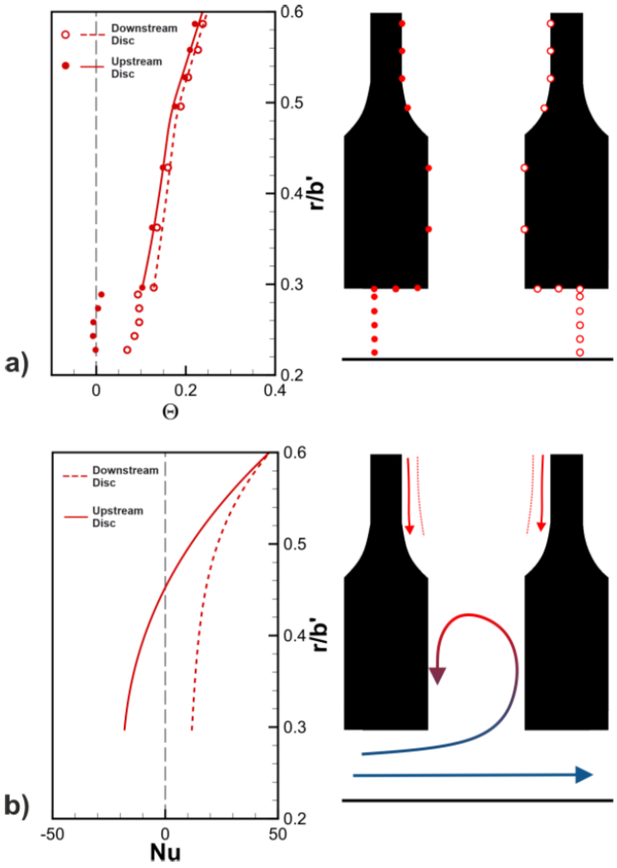

Figure 6.14 – Radial distribution of Θ *(a) and* Nu *(b) for the upstream and downstream disks at* Ro *= 0.4 ($\beta\Delta T$ = 0.24;* Re_ϕ *= 2.2×10^6;* Gr *= 1.2×10^{12}).*

6.5 MAIN FINDINGS

Mathematical models based on Bayesian statistics and the circular fin equation have been used to calculate Nusselt numbers using steady-state disk temperature measurements in the Bath Compressor-Cavity Rig.

Steady-state temperature data was collected and analysed for a range of the important non-dimensional parameters: Re_ϕ, $\beta\Delta T$, Gr, and Ro. The ranges of these parameters were: $0.8\times10^6 < \mathrm{Re}_\phi < 3.0\times10^6$; $0.10 < \beta\Delta T < 0.25$; $7.0\times10^{10} < \mathrm{Gr} < 2.0\times10^{12}$; $0.1 < \mathrm{Ro} < 0.4$. The Nusselt numbers were estimated using the Bayesian model applied to the inverse solution of the fin equation.

Analysis showed that, due to an increase in the buoyancy forces, the radially-weighted average disk Nusselt numbers increased with increasing $\beta\Delta T$. However, at high rotational speeds an increase in Re_ϕ could cause a decrease in $\overline{\mathrm{Nu}}$. This effect, which is attributed to a temperature rise in the core, is created by compressibility effects in the air.

An inner region, between the axial through-flow and the region of buoyancy-induced flow, was shown to constitute a combined source-sink for the cavity. It is also a mixing region, in which entrained cold through-flow mixes with hot fluid from the Ekman layers. Consequently, the air temperature in the cavity tends to decrease, and the Nusselt numbers tend to increase, as Re_z increases. As the Rossby number, Ro, is proportional to the ratio of Re_z to Re_ϕ, the Nusselt numbers therefore tend to increase as Ro increases. The buoyancy number, Bo, which is the ratio of free (buoyancy-induced) and forced convection, is inversely proportional to Ro. Consequently, Nu tends to increase as Bo decreases.

The Owen and Tang Buoyancy Model has been used to compare predicted radial distributions of disk temperatures and Nusselt numbers with the experimentally determined distributions, taking account of radiation between the inner surfaces of the cavity. Although there was good agreement with the temperature measurements at the higher values of Bo (that is, at the smaller values of Ro and the larger values of $\beta\Delta T$), the agreement was less good at the smaller values of Bo. This suggests that the effects of forced convection can be significant in the inner region, and the Buoyancy Model may need to be extended to include these effects.

Chapter 7

Conclusions and future work

This Chapter presents the conclusions of the thesis, building up from main findings from each of the Chapters 3-6. The future research activities which can be envisaged are then reported, and divided in three main areas.

7.1 CONCLUSIONS

Radial growth of compressor disks

To evaluate the influence of the radial temperature distribution on the disk growth (and ultimately on the blade tip clearance), the overall radial growth of an isolated compressor disk was divided in three components: the *thermal expansion* (material-related); the *rotational growth* (due to the rotational speed); and the *thermal growth* (due to the stresses created by the temperature gradients). This is a complex conjugate problem faced by the engine designer: since the temperature gradients depend on the Nusselt numbers generated by the buoyancy-induced flow in the fluid core of the cavity between adjacent disks, and the Nusselt numbers depend, in turn, on the radial temperature distribution in the disk.

The three growth components have been calculated separately for a single disk operating at the steady-state conditions associated with compressor pressure ratios of 50, 60 and 70 to 1. At each pressure ratio, calculations were conducted for five different temperature distributions: the distribution based on the Owen and Tang Buoyancy Model was used as the datum case, and results from this were compared with those from linear, quadratic, cubic and quartic power laws. For the 50:1 pressure ratio, the calculations were conducted using both FEA and a theoretical 1D stress model.

The radial distribution of temperature has a significant effect on the disk growth and consequently on the blade clearance in a compressor. Although the growth due to the thermal stress is small relative to the total growth of the disk, it is the same magnitude as the blade clearance. For the assumptions used in the calculations, the pressure ratio has instead a relatively small effect on the thermal growth.

Using the Buoyancy Model as a datum, comparison with the growth predicted using power-law temperature distributions shows that a quartic power-law produces the most accurate results. By contrast, a linear power-law causes errors the same magnitude as the thermal growth itself. Although a power-law profile might be suitable for the steady-state cases considered here, no single power law could fit the changing temperature profile during a thermal transient. Only transient modelling is able to predict the evolution of the thermal growth during a manoeuvre. A lumped-parameters transient model run between two engine steady states in a deceleration scenario revealed that the time behaviours of the thermal growth and the thermal expansion are not synchronous. The design of the Bath Compressor-Cavity Rig allows with limited modifications the measurement of the radial growth of the disks in both steady-state and transient conditions.

The good agreement between the growths predicted by the 1D theoretical model and the FEA computations suggests that the combination of the 1D model and the Buoyancy Model could be useful in the preliminary calculation of blade clearances. The advantage of this approach is that the combined solution of the coupled 1D stress and buoyancy equations may take only seconds on an ordinary laptop.

Thermo-mechanical analysis of the Bath Compressor-Cavity Rig

The design of the rotating disk pack of the Bath Compressor-Cavity Rig has been validated via the calculations presented in Chapter 4. The rig design successfully meets the requirements of life and safety.

The loads and boundary conditions used were representative of the rig tests, while the calculation assessment has provided insight into the disk deformation, following a comprehensive assessment of the rig behaviour. Calculations from an initial design led to an improved design, which has been shown to be successful in terms of limited stress and acceptable life. Under the maximum expected load, there are no locations where the disk material is stressed above the elastic limit.

The maximum stresses (static and fatigue failure) in the disk pack are located at the first two thermocouple slots on the disk diaphragms (especially on disk 2) and on all the features in the cob. Of critical importance, the equivalent stress values at these locations are always below the yield strength of the disk material, with a static safety factor of at least 1.26 and a fatigue safety factor of at least 1.37. Of further importance, the fatigue model and the mean stress values are both conservative. The maximum stress levels have been compared favourably to an engineering study for an unfeatured disk pack and a stress-concentration-factor study. This provides further confidence on the reliability of the solution.

It was shown that a successful standard ultrasonic test allows pre-existing cracks which do not raise concerns with regards the static failure. Surface cracks on the disk bore and on the features, i.e. the potentially critical location for crack failures, were not visually detected. The analysed crack propagation cases – which feature only ideal surface cracks and uncertainty in the material parameters characterizing the crack propagation behaviour – take into account surface cracks oriented normally with respect the material surface and located *exactly* in the locations of maximum stress. This event is unlikely and there is a very small associated risk. In conclusion, there is no reasonable concern regarding crack propagation. Finally, the operating conditions of the rig will not always be at full speed (8,000 rpm) with maximum heating – consequently this will result in an increased safety factor and expected life.

The thermo-mechanical analysis was reviewed by engineers at Rolls-Royce with full approval.

Design and commissioning of the Bath Compressor-Cavity Rig

The Bath Compressor-Cavity Rig has been designed to investigate the buoyancy-induced heat transfer that occurs inside the compressor rotors of aero-engines. The test section includes four rotating disks enclosing three cavities; the central cavity is instrumented with thermocouples and the outer cavities are thermally insulated. There is an axial through-flow of air between a stationary central shaft and the bore of the disks. For a cold through-flow, the outer shroud of the central cavity is heated by two radiant heaters, which allows different shroud temperatures on the upstream and downstream disks. There is provision for the through-flow to be heated to investigate cases with negative Grashof numbers, which can occur during engine accelerations and decelerations when the through-flow is hotter than the shroud. As stratified flow could occur under these conditions – significantly reducing convection in the cavity so that radiation could be dominant – all internal surfaces of the cavity were painted matt black. This allows the accurate calculation of the radiant heat transfer also in cases with cold through-flows.

Modularity and flexibility have been addressed in the design of the rig. A rail system allows movement of the disk pack relative to the drive unit and access to the test section. Separate attachments can be fitted to the cobs of both central disks; the attachments reduce the axial gap between the cobs – reducing the gap to zero creates a closed cavity, which can occur in some compressor designs.

Both titanium disks forming the central cavity featured a radial distribution of 28 thermocouples across the cob and diaphragm regions. The thermocouples were located in circumferential slots designed to minimize stress concentrations and thermal disturbance. Other instrumentation on the rotating disks included heat-flux gauges and high-frequency pressure transducers. Attention has been given to experimental uncertainty, including the computation of thermal-disturbance errors, caused by thermocouples embedded in the rotating disks. A Bayesian model has been used to reduce the effect of uncertainties in temperature measurements on the calculation of Nu.

In non-dimensional terms, the rig can operate over the range $-1.2\times10^{12} < \mathrm{Gr} < 2\times10^{12}$, $0.1 < \mathrm{Ro} < 0.8$, and up to $\mathrm{Re}_\phi = 3\times10^6$, $\mathrm{Re}_z = 4\times10^4$ and $\beta\Delta T = 0.25$. The effect of Ro and $\beta\Delta T$ on the radial distribution of both the disk and through-flow temperatures were readily highlighted in the first tests after commissioning. Disk temperatures measured on the rig are adequate to determine the effect of Re_ϕ, Ro and $\beta\Delta T$ on the radial distribution of Nu.

Buoyancy-induced heat transfer in the Bath Compressor-Cavity Rig

Mathematical models based on Bayesian statistics and the circular fin equation have been used to calculate Nusselt numbers using steady-state disk temperature measurements in the Bath Compressor-Cavity Rig.

Steady-state temperature data was collected and analysed for a range of the important non-dimensional parameters: Re_ϕ, $\beta\Delta T$, Gr, and Ro. The ranges of these parameters were: $0.8\times10^6 < \mathrm{Re}_\phi < 3.0\times10^6$; $0.10 < \beta\Delta T < 0.25$; $7.0\times10^{10} < \mathrm{Gr} < 2.0\times10^{12}$; $0.1 < \mathrm{Ro} < 0.4$. The Nusselt numbers were estimated using the Bayesian model applied to the inverse solution of the fin equation.

Analysis showed that, due to an increase in the buoyancy forces, the radially-weighted average disk Nusselt numbers increased with increasing $\beta\Delta T$. However, at high rotational speeds an increase in Re_ϕ could cause a decrease in Nu. This effect, which is attributed to a temperature rise in the core, is created by compressibility effects in the air.

An inner region, between the axial through-flow and the region of buoyancy-induced flow, was shown to constitute a combined source-sink for the cavity. It is also a mixing region, in which entrained cold through-flow mixes with hot fluid from the Ekman layers. Consequently, the air temperature in the cavity tends to decrease, and the Nusselt numbers tend to increase, as Re_z increases. As the Rossby number, Ro, is proportional to the ratio of Re_z to Re_ϕ, the Nusselt numbers therefore tend to increase as Ro increases. The buoyancy number, Bo, which is the ratio of free (buoyancy-induced) and forced convection, is inversely proportional to Ro. Consequently, Nu tends to increase as Bo decreases.

The Owen and Tang Buoyancy Model has been used to compare predicted radial distributions of disk temperatures and Nusselt numbers with the experimentally determined distributions, taking account of radiation between the inner surfaces of the cavity. Although there was good agreement with the temperature measurements at the higher values of Bo (that is, at the smaller values of Ro and the larger values of $\beta \Delta T$), the agreement was less good at the smaller values of Bo. This suggests that the effects of forced convection can be significant in the inner region, and the Buoyancy Model may need to be extended to include these effects.

7.2 FUTURE WORK

The study of buoyancy-induced heat transfer in axial compressor cavities involves multi-disciplinary aspects and contributions. Future work is here divided into three main areas: radial growth of compressor disks, theoretical modelling and experimental activity. The experimental activity is strictly related to the rig operation. The other two activities would rely on rig testing to achieve robust validation. In a complementary manner, modelling of the cavity heat transfer and radial growth will help and direct the interpretation of the experimental results.

Radial growth of compressor disks

Future activities regarding compressor radial growth should not be limited to the isolated disk assumption. The model development would have two directions. The first consists in adopting a 2D or 3D multi-disk model, up to the entire HPC rotor. The added geometrical complexity cannot be captured by 1D modelling – which still holds robust for preliminary single disk calculations – in favour of FEA only. Theoretical modelling would have to be extended to more than one cavity at the time (each with a different Nusselt number and temperature profiles).

The other future direction for compressor growth modelling is to extend and refine the geometry in the shroud area, leading to the blade platform characterisation and to extend to the rotor blades themselves. A refinement of the main annulus flow conditions would be mandatory.

Theoretical modelling

This thesis does not directly deal with the theoretical aspects of buoyancy-induced flows. However, it can give some insight for future developments of the Owen and Tang Buoyancy Model for what strictly concerns the interpretation of the experimental data achievable via the Bath Compressor-Cavity Rig in all its foreseen operating modes. The following extensions of the model would be beneficial:

- Extend the model to understand the interaction with the through-flow and include the forced convection effects in the cavity inner region
- Include transient effects, to underpin transient rig data
- Include the effects of asymmetrical heating of the cavity (one disk hotter than the other), i.e. the model could be applied to more than one cavity at the time.

Experimental activity

First, future work will include experiments and theoretical modelling over a wider parameter range. This will involve measurements of heat transfer on the shroud and unsteady pressures on the surface of the disks; the pressure measurements will be used to determine the unsteady flow structures in the core. The temperature of the air in the cavity will be measured by a custom-made aerodynamic probe. In addition, there will be tests with different cob geometries – including the closed-cavity case with no axial clearance between the cobs – and with differential heating of the shroud to produce different temperatures for the two disks. Importantly, tests will also be conducted with heated through-flow to produce conditions in which stratified flow could occur in the cavity.

Non-symmetrical heating of the cavity might be achieved powering only one set of radiant heaters, corresponding to the shroud of only one disk. This will help to understand how the heat transfer changes compared to the symmetrical heating base case. The non-symmetrical heating condition is the one actually happening during engine steady state, as the flow in the main annulus becomes hotter stage by stage.

Finally, transient experiments would give extensive sets of valuable data to inform a transient Buoyancy Model. From an engine designer perspective, the possibility to predict the cavity heat transfer in transient conditions would mean the ability to predict reliably the blade tip clearance at all engine operating conditions and manoeuvres, pushing the limits of the current performance and guaranteeing high levels of engine safety and efficiency.

References

Agarwal, H., Akkaram, S., Shetye, S. and McCallum, A., 2008. Reduced Order Clearance Models for Gas Turbine Applications. *49th AIAA/ASME/ASCE/AHS/ASC Structures, Structural Dynamics and Material Conference*, Schaumburg, IL, USA, Apr 7-10, AIAA Paper No. 2008-2177. https://doi.org/10.2514/6.2008-2177.

Alexiou, A., 2000. *Flow and heat transfer in gas turbine H.P. compressor internal systems*. Thesis (Ph.D.). University of Sussex, Brighton, UK.

Appelquist, E. 2017. *The rotating-disk boundary layer flow studied through numerical simulations*. Thesis (Ph.D.). Royal Institute of Technology KTH, Stockholm, Sweden.

Atkins, N. R. and Kanjirakkad, V., 2014. Flow in a rotating cavity with axial throughflow at engine representative conditions. *Proceedings of ASME Turbo Expo*, Düsseldorf, Germany, June 16-20, Paper No. GT2014-271747, V05CT16A041 (14 pages). https://doi.org/10.1115/GT2014-27174.

Atkins, N. R., 2013. Investigation of a radial-inflow bleed as a potential for compressor clearance control. *Proceedings of ASME Turbo Expo*, San Antonio, Texas, USA, June 3-7, Paper No. GT2013-95768, V03AT15A020 (14 pages). https://doi.org/10.1115/GT2013-95768.

Baghdadi, S., 1996. Modeling Tip Clearance Effects in Multistage Axial Compressors. *Journal of Turbomachinery,* Vol. 118(4), pp. 697-705. https://doi.org/10.1115/1.2840925.

Ballal, D. R. and Zelina, J., 2004. Progress in Aeroengine Technology (1939-2003). *Journal of Aircraft*, Vol. 41, No.1, pp. 43-50. https://doi.org/10.2514/1.562.

Bohn, D. E., Deutsch, G. N., Simon, B. and Burkhardt, C., 2000. Flow Visualisation in a Rotating Cavity with Axial Throughflow. *Proceedings of ASME Turbo Expo*, Munich, Germany, May 8-11, Paper No. 2000-GT-280, V003T01A084 (8 pages). https://doi.org/10.1115/2000-GT-0280.

Bohn, D., Deuker, E., Emunds, R. and Gorzelitz, V., 1995. Experimental and Theoretical Investigations of Heat Transfer in Closed Gas-Filled Rotating Annuli. *Journal of Turbomachinery,* Vol. 117(1), pp. 175–183. https://doi.org/10.1115/1.2835635.

BSI, 2017. *BS 3TA 11:2009+A1:2017 Specification for bar and section for machining of titanium-aluminium-vanadium alloy (Tensile strength 900–1 160 MPa) (Limiting ruling section 150 mm).*

Budynas, R. G. and Nisbett, J. K., 2010. 9th ed. *Shigley's Mechanical Engineering Design*. McGraw Hill.

Burkhardt, C., Mayer, A. and Reile, E., 1993. Transient Thermal Behaviour of a Compressor Rotor with Axial Cooling Air Flow and Co-Rotating or Contra-Rotating Shaft. *AGARD Conference Proceedings 527, Heat Transfer and Cooling in Gas Turbines*, presented at the *Propulsion and Energetics Panel 80th Symposium*, Antalya, Turkey, 12-16 Oct. 1992, pp. 21.1-21.9.

Chapman, A., J, 1984. Heat Teansfer. 4th ed. Pearson College Div.

Childs, P. R. N., 2011. *Rotating Flow*. Butterworth-Heinemann/Elsevier.

Cohen, H., Rogers, G. F. C. and Saravanamuttoo, H. I. H., 1996. *Gas Turbine Theory*. 4th ed. Longman Group Limited.

Crespo del Arco, E., Serre, E., Bontoux, P. and Launder, B. E., 2005. Stability, transition and turbulence in rotating cavities. In: M. Rahman, ed. *Instability of Flows*. Wit Press, pp. 141-195.

Cumpsty, N., 2003. *Jet Propulsion: A Simple Guide to Aerodynamic and Thermodynamic Design and Performance of Jet Engines*. Cambridge University Press.

Denton, J. D., 1993. Loss Mechanisms in Turbomachines. *Journal of Turbomachinery*, Vol. 115(4), pp. 621-656. https://doi.org/10.1115/1.2929299.

Diemel, E., Odenbach, S., Uffrecht, W., Rey Villazon, J., Guijarro Valencia, A. and Reinecke, M., 2019. High speed single cavity rig with axial throughflow of cooling air: rig structure and periphery. *Proceedings of ASME Turbo Expo*, Phoenix, AZ, USA, June 17-21, Paper No. GT2019-91265, V05BT15A010 (11 pages). https://doi.org/10.1115/GT2019-91265.

Dixon, S. L. and Hall, C. A., 2014. *Fluid Mechanics and Thermodynamics of Turbomachinery*. 7th ed. Butterworth-Heinemann/Elsevier.

Dong, Y., Xinqian, Z. and Qiushi, L., 2014. An 11-Stage Axial Performance Simulation Considering the Change of Tip Clearance in Different Operating Conditions. *Proceedings of the Institution of Mechanical Engineers, Part A: Journal of Power and Energy*, Vol. 228(6), pp. 614–625. https://doi.org/10.1177/0957650914535389.

Dorfman, L. A., 1963. *Hydrodynamic Resistance and the Heat Loss of Rotating Solids*. Oliver & Boyd.

Farthing, P. R., Chew, J. W. and Owen, J. M., 1991. The use of deswirl nozzles to reduce the pressure drop in a rotating cavity with a radial inflow. *Journal of Turbomachinery*, Vol. 113(1), pp. 106-114. https://doi.org/10.1115/1.2927727.

Farthing, P. R., Long, C. A., Owen, J. M. and Pincombe, J. R., 1992a. Rotating cavity with axial throughflow of cooling air: flow structure. *Journal of Turbomachinery*, Vol. 114(1), pp. 237-246. https://doi.org/10.1115/1.2927991.

Farthing, P. R., Long, C. A., Owen, J. M. and Pincombe, J. R., 1992b. Rotating cavity with axial throughflow of cooling air: heat transfer. *Journal of Turbomachinery*, Vol. 114(1), pp. 229-236. https://doi.org/10.1115/1.2927990.

Günther, A., Uffrecht, W. and Odenbach, S., 2012. Local measurements of disc heat transfer in heated rotating cavities for several flow regimes. *Journal of Turbomachinery*, Vol. 134(5): 051016 (9 pages). https://doi.org/10.1115/1.4003965.

Günther, A., Uffrecht, W. and Odenbach, S., 2014. The Effects of Rotation and Mass Flow on Local Heat Transfer in Rotating Cavities with Axial Throughflow. *Proceedings of ASME Turbo Expo*, Düsseldorf, Germany, June 16-20, Paper No. GT2014-26228, V05CT16A026 (9 pages). https://doi.org/10.1115/GT2014-26228.

Incropera, F. P., Dewitt, D. P., Bergman, T. L. and Lavine, A. S., 2013. *Fundamentals of Heat and Mass Transfer*. 7th ed. John Wiley & Sons.

Jackson, R. W., Luberti, D., Tang, H., Pountney, O. J., Scobie, J. A., Sangan, C. M., Owen, J. M. and Lock, G. D., 2021. Measurement and Analysis of Buoyancu-Induced Heat Transfer in Aero-Engine Compressor Rotors. *Journal of Engineering for Gas Turbines and Power*, 143(6): 0610004 (9 pages). https://doi.org/10.1115/1.4049100.

Johnson, B. V., Daniels, W. A., Kawecki, E. J. and Martin, R. J., 1991. Compressor drum aerodynamic experiments and analysis with coolant injected at selected locations. *Journal of Turbomachinery,* Vol. 113(2), pp. 272-280. https://doi.org/10.1115/1.2929101.

Johnson, B. V., Lin, J. D., Daniels, W. A. and Paolillo, R., 2006. Flow characteristics and stability analysis of variable-density rotating flows in compressor-disc cavities. *Journal of Engineering for Gas Turbines and Power*, Vol. 128(1), pp. 118-127. https://doi.org/10.1115/1.1925648.

Juvinall, R. C. and Marshek, K. M., 2011. 5th ed. *Fundamentals of Machine Component Design*. John Wiley & Sons.

Keller, S., 2015. A practical approach to implementing linear elastic fracture mechanics in gas turbine rotor disk analyses, *Proceedings of the ASME Turbo Expo*, Montréal, Canada, June 15-19, Paper No. GT2015-43303, V07AT28A010 (9 pages). https://doi.org/10.1115/GT2015-43303.

Kypuros, J. A. and Melcher, K. J., 2003. A Reduced Model for Prediction of Thermal and Rotational Effects on Turbine Tip Clearance. NASA Glenn Research Center, Cleveland, OH, USA, Report No. NASA/TM–2003-212226. Available at: https://ntrs.nasa.gov/citations/20030032933.

Long, C. A., Miché, N. D. D. and Childs, P. R. N., 2007. Flow Measurements Inside a Heated Multiple Rotating Cavity with Axial Throughflow. *International Journal of Heat and Fluid Flow,* Vol. 28(6), pp. 1391-1404. https://doi.org/10.1016/j.ijheatfluidflow.2007.04.010.

Long, C. A. and Childs, P. N. R., 2007. Shroud Heat Transfer Measurements inside a Heated Multiple Rotating Cavity with Axial Throughflow. *International Journal of Heat and Fluid Flow*. Vol. 28(6), pp. 1405-1417. https://doi.org/10.1016/j.ijheatfluidflow.2007.04.009.

Long, C. A., Alexiou, A. and Smout, P. D., 2003. Heat Transfer in H.P. Compressor Gas Turbine Internal Air Systems: Measurements from the Peripheral Shroud of a Rotating Cavity with Axial Throughflow. *2nd International Conference on Heat Transfer, Fluid Mechanics and Thermodynamics (HEFAT)*, June 23-26, Victoria Falls, Zambia, Paper No. LC1.

Luberti, D., Patinios, M., Jackson, R. W., Tang, H., Pountney, O. J., Scobie, J. A., Sangan, C. M., Owen, J. M. and Lock, G. D., 2021. Design and Testing of a Rig to Investigate Buoyancy-Induced Heat Transfer in Aero-Engine Compressor Rotors. *Journal of Engineering for Gas Turbines and Power*, Vol. 143(4): 041030 (11 pages). https://doi.org/10.1115/1.4048601.

Luberti, D., Tang, H., Scobie, J., Pountney, O.J., Owen, J.M. and Lock, G., 2020. Influence of Temperature Distribution on Radial Growth of Compressor Disks. *Journal of Engineering for Gas Turbines and Power*, 142(7): 071004 (10 pages). https://doi.org/10.1115/1.4046704.

Miché, N. D., 2008. Flow and Heat Transfer Measurements inside a Heated Multiple Rotating Cavity with Axial Throughflow. Thesis (Ph.D.). University of Sussex, Brighton, UK.

Muktinutalapati, N. R., 2011. Materials for Gas Turbines – An Overview. In: Benini. E., ed. *Advances in Gas Turbine Technology*, IntechOpen, Chapter 13, pp. 293–314. DOI: 10.5772/20730.

Ohja, P. and Raghava, K. Trent 1000 presentation. Available at https://image.slidesharecdn.com/trent1000presentation-141105035408-conversion-gate02/95/trent-1000-presentation-11-638.jpg?cb=1415159754.

Owen, J. M. and Bilimoria, E. D., 1977. Heat Transfer in Rotating Cylindrical Cavities. *Journal of Mechanical Engineering Science*, Vol. 19, No. 4, pp. 175-187. https://doi.org/10.1243/JMES_JOUR_1977_019_038_02.

Owen, J. M. and Long, C. A., 2015. Review of Buoyancy-Induced Flow in Rotating Cavities. *Journal of Turbomachinery,* Vol. 137(11): 111001 (13 pages). https://doi.org/10.1115/1.4031039.

Owen, J. M. and Pincombe, J. R., 1979. Vortex breakdown in a rotating cylindrical cavity. *Journal of Fluid Mechanics*, Vol. 90, part 1, pp.109-127. https://doi.org/10.1017/S0022112079002093.

Owen, J. M. and Powell, J., 2004. Buoyancy-induced flow in a heated rotating cavity. *Proceedings of ASME Turbo Expo*, Vienna, Austria, June 14-17, Paper No. GT2004-53210, pp. 297-305. https://doi.org/10.1115/GT2004-53210.

Owen, J. M. and Rogers, R. H., 1989. *Flow and Heat Transfer in Rotating Disc Systems, Vol.1: Rotor-Stator Systems*. Research Studies Press.

Owen, J. M. and Tang, H., 2015. Theoretical Model of Buoyancy-Induced Flow in Rotating Cavities. *Journal of Turbomachinery*, Vol. 137(11): 111005 (7 pages). https://doi.org/10.1115/1.4031353.

Owen, J. M., 1979. On the Computation of Heat-Transfer Coefficients from Imperfect Temperature Measurements. *Journal of Mechanical Engineering Science*, Vol. 21, No. 5, pp. 323-334. https://doi.org/10.1243/JMES_JOUR_1979_021_055_02.

Owen, J. M., 2010. Thermodynamic analysis of buoyancy-induced flow in rotating cavities. *Journal of Turbomachinery*, Vol. 132(3): 031006 (7 pages). https://doi.org/10.1115/1.2988170.

Owen, J. M., Tang, H. and Lock, G. D., 2018. Buoyancy-Induced Heat Transfer inside Compressor Rotors: Overview of Theoretical Models. *Aerospace*, Vol. 5(1): 32 (22 pages). https://doi.org/10.3390/aerospace5010032.

Pilidis, P. and Maccallum, N. R. L., 1984. A Study of the Prediction of Tip and Seal Clearances and Their Effects in Gas Turbine Transients. *Proceedings of ASME,* Paper No. 84-GT-245. https://doi.org/10.1115/84-GT-245.

Pitz, D. B, Marxen, O. and Chew, J. W., 2017. Onset of convection induced by centrifugal buoyancy in a rotating cavity. *Journal of Fluid Mechanics,* Vol. 826, pp. 484-502. doi:10.1017/jfm.2017.451.

Pitz, D. B., Chew, J. W. and Marxen, O., 2019. Large-Eddy Simulation of Buoyancy-Induced Flow in a Sealed Rotating Cavity. *Journal of Engineering for Gas Turbines and Power,* Vol. 141(2): 021020 (9 pages). https://doi.org/10.1115/1.4041113.

Pountney, O., Patinios, M., Tang, H., Luberti, D., Sangan, C., Scobie, J., Owen, M., & Lock, G. (2021). Calibration of Thermopile Heat Flux Gauges using a Physically-Based Equation. *Proceedings of the Institution of Mechanical Engineers Part A: Journal of Power and Energy*, Vol. 0(0), pp. 1-11. https://doi.org/10.1177/0957650920982103.

Quan, Y., Han, D., Xu, G., Wen, J. and Luo, X., 2018. Convective Heat Transfer of a Rotating Multi-Stage Cavity with Axial Throughflow. *International Journal of Heat and Mass Transfer*, 119, pp. 117-127. https://doi.org/10.1016/j.ijheatmasstransfer.2017.11.110.

Rolls-Royce, 1996. *The Jet Engine*. 5th ed. Rolls-Royce plc.

Rolls-Royce, 2015. *The Jet Engine*. 6th ed. John Wiley & Sons.

SAE International, 1972. *AMS2631 Ultrasonic Inspection, Titanium and Titanium Alloy Bar and Billet*.

Schlichting, H., 2000. *Boundary Layer Theory*. 8th ed. Springer-Verlag Berlin Heidelberg.

Sultanian, B. K., 2018. *Gas Turbines Internal Flow System Modeling*. Cambridge University Press.

Sun, Z., Lindblad, K., Chew, J. W. and Young, C., 2007. LES and RANS Investigations into Buoyancy-Affected Convection in a Rotating Cavity With a Central Axial Throughflow. *Journal of Engineering for Gas Turbines and Power*, Vol. 129(2), pp. 318-325. https://doi.org/10.1115/1.2364192.

Tang, H. and Owen, J. M., 2017. Effect of Buoyancy-Induced Rotating Flow on Temperatures of Compressor Disks. *Journal of Engineering for Gas Turbines and Power,* Vol. 139(6): 062506 (10 pages). https://doi.org/10.1115/1.4035400.

Tang, H. and Owen, J. M., 2018. Theoretical Model of Buoyancy-Induced Heat Transfer in Closed Compressor Rotors. *Journal of Engineering for Gas Turbines and Power*, Vol. 140(3): 032605 (7 pages). https://doi.org/10.1115/1.4037926.

Tang, H. and Owen, J.M, 2021. Effect of Radiation on Heat Transfer inside Aeroengine Compressor Rotors. *Journal of Turbomachinery,* Vol. 143(5): 051005 (7 pages). https://doi.org/10.1115/1.4050114.

Tang, H., Puttock-Brown, R. and Owen, J. M., 2018. Buoyancy-Induced Flow and Heat Transfer in Compressor Rotors. *Journal of Engineering for Gas Turbines and Power*, Vol. 140(7): 071902 (10 pages). https://doi.org/10.1115/1.4038756.

Tang, H., Shardlow, T. and Owen, M. J., 2015. Use of Fin Equation to Calculate Nusselt Numbers for Rotating Disks. *Journal of Turbomachinery,* Vol. 137(12): 121003 (10 pages). https://doi.org/10.1115/1.4031355.

Vullo, V. and Vivio, F., 2013. *Rotors: Stress Analysis and Design*, Springer-Verlag.

Wang, K., Wang, F., Cui, W., Hayat, T. and Ahmad, B., 2014. Prediction of short fatigue crack growth of Ti-6Al-4V. *Fatigue & Fracture of Engineering Materials & Structures*, Vol. 37(10), pp. 1075-1086. https://doi.org/10.1111/ffe.12177.

Yepifanov, S. V., Zelenskyi, R. L. and Loboda, I., 2015. Modeling the Gas Turbine Engine Under Its Dynamic Heating Conditions. *Journal of Engineering for Gas Turbines and Power*, 137(3): 031506 (10 pages). https://doi.org/10.1115/1.4028449.